



TECHNISCHE UNIVERSITÄT MÜNCHEN

TUM SCHOOL OF COMPUTATION, INFORMATION AND TECHNOLOGY

Real-time Optoacoustic Monitoring of Thermal Ablation and Laser Surgery

FRANCISCO JAVIER OYAGA LANDA

Vollständiger Abdruck der von der TUM School of Computation, Information and Technology der Technischen Universität München zur Erlangung des akademischen Grades eines

Doktors der Naturwissenschaften (Dr. rer. nat.)

genehmigten Dissertation.

Vorsitzende(r):

Prof. Dr.-Ing. Matthias Althoff

Prüfer der Dissertation:

1. Prof. Dr. Bjoern Menze
2. Prof. Dr. Daniel Razansky
3. apl. Prof. Dr. Christoph Haisch

Die Dissertation wurde am 20.01.2021 bei der Technischen Universität München eingereicht und durch die Fakultät für Informatik am 15.06.2022 angenommen.

“Nature does not hurry, yet everything is accomplished.”

— Lao Tzu

Abstract

Therapeutic interventions based on thermal ablation are commonly employed medical procedures for annihilating malignant tumors and treating other disorders that require selective tissue targeting. Although thermal ablation presents important advantages with respect to alternative therapeutic options, the lack of haptic feedback during ablative treatments remains a major drawback. As a consequence, clinical interventions commonly result in a high number of undesired outcomes, excessive collateral damage to healthy tissues or ineffective treatments that need to be repeated. In this thesis, we investigate on the feasibility of using optoacoustics, a fast growing biomedical imaging and sensing modality, to provide real-time feedback during thermal ablation and to assess the outcome of these procedures. In this context, two types of ablation treatments were studied, namely laser surgery, aimed to generate incisions replacing traditional scalpels, and thermal therapies using a variety of energy sources, such as photothermal, focused ultrasound and radiofrequency current. Mathematical models of thermal diffusion as well as new hardware configurations based on air-coupled transducers and radio-frequency catheters were further developed in order to fully exploit the optoacoustic monitoring capabilities. The experimental results demonstrate the powerful performance of optoacoustics as a real-time feedback tool providing quantitative readings of the critical ablation parameters during thermal ablation procedures. Current limitations of the developed monitoring approaches are discussed and potential technological improvements are laid out.

Acknowledgements

This dissertation would not have been possible without the help, support and guidance of many people.

Foremost, I would like to express my sincere gratitude towards my supervisors Prof. Dr. Daniel Razansky and Prof. Dr. Bjoern Menze, for their great leadership, guidance and support throughout the last years.

Secondly, I would like to express my appreciation and thanks to Dr. Xosé Luís Deán-Ben for his dedication, unlimited patience and time supporting my doctoral research.

Big thanks go to everyone at the Institute of Biological and Medical Imaging at Helmholtz Center Munich who made this time in academia highly enjoyable.

Furthermore, I would like to thank Prof. Dr. Anand Kumar for giving me the opportunity of collaborating with his group during my research stay in Boston.

And how can we not give special mention to my family, friends and loved ones. You know that your support and encouragement was worth more than I can express on paper.

Contents

Abstract	ii
Acknowledgements	iii
Contents	iv
List of Figures	vi
Abbreviations	x
Physical Parameters	xi
0 Summary	1
1 Background	1
1.1 Thermal Ablation Treatments	1
1.2 Effects of Temperature on Biological Tissue	3
1.3 Laser Surgery	6
1.4 Laser Induced Thermotherapy (LITT)	7
1.5 High Focused Ultrasound (HIFU) Treatments	8
1.6 Radiofrequency Ablation (RFA)	10
1.7 Temperature Monitoring Techniques	11
1.7.1 Invasive Approaches for Temperature Monitoring	11
1.7.2 Non-invasive Approaches for Temperature Monitoring	15
1.8 Optoacoustic Imaging	20
1.8.1 Light and Sound Propagation in Tissue	20
1.8.2 The Optoacoustic Effect	26
1.8.3 Optoacoustic Signal Detection	30
1.8.4 General Forward Solution and Reconstruction	31
2 Methods and Contributions	34
2.1 Noncontact Monitoring of Incision Depth in Laser Surgery with Air-coupled Ultrasound Transducers	35
2.2 Integrated Catheter for Simultaneous Radio-frequency Ablation and Optoacoustic Monitoring of Lesion Progression	42

2.3	Volumetric Optoacoustic Temperature Mapping in Photothermal Therapy	49
2.4	Four-dimensional Optoacoustic Monitoring of Tissue Heating with Medium Intensity Focused Ultrasound	60
2.5	Optoacoustic Monitoring of RF Ablation Lesion Progression	64
3	Publications	73
4	Summary and Conclusion	105
	Bibliography	107

List of Figures

1.1	Clinical setup of radio-frequency thermal ablation being monitored with pulse-echo ultrasound. Multi-tine catheter tip is positioned in the targeted tissue volume. Image courtesy of Mallinckrodt Institute of Radiology. ©	2
1.2	Thermal effects in tissue as a function of temperature and exposure time [132]. As the temperature decreases, the exposure time needed to achieve thermal necrosis increases exponentially. Temperature and exposure times generally used for both local hyperthermia and thermal ablation are marked. Tissue water boils above the threshold of 100 °C regardless of the exposure time. ©	4
1.3	Representative signals versus temperature for Y3Al5O12:Ce. Peaks at all three temperatures were normalized to the same height for comparison purposes. (top trace, 10°C, middle trace 40°C, bottom trace 77°C). [99]	14
1.4	Optical excitation and relaxation of atoms and molecules from the ground state to excited states can result in fluorescence, phosphorescence, energy transfer, electron transfer, stimulated emission or non-radiative relaxation.	21
1.5	Optical absorption spectra of major endogenous chromophores at typical concentrations occurring in living mammalian tissues. Melanin spectrum (brown) is shown for typical concentrations in the skin; hemoglobin (red – oxygenated, blue – deoxygenated) for typical concentrations in whole blood (150 g l^{-1} – continuous lines) and average soft tissues (15 g l^{-1} – continuous lines); water (cyan) for a typical concentration of 80% by volume in soft tissues; lipids (yellow) for a concentration of 20% by volume. The first (NIR - I) and second (NIR - II) windows, where optical absorption is minimized, are indicated [133]. ©	23
1.6	Schematics of optoacoustic signal generation by short-pulsed excitation of a spherical absorber.	27
2.1	Diagram of plasma formation at the focal spot of a focused laser pulse.	35
2.2	(a) Layout of the experimental setup. ACT, air-coupled transducer; DAQ, data acquisition. The glass slide with 1.1 mm thickness is positioned at 45° relative to the propagation direction of the shockwaves so that the acoustic waves are reflected at 90° into the ACT. (b) Ablation beam characterization in the vicinity of the focal region. Typical beam shapes are shown in the inset. The effective depth of the focus is approximately 5 mm.	38

2.3	Illustration of the method used to estimate the incision depth within the incision profile for different tissue types. Examples of the recorded signals for (a) liver cheese, (b) chicken, and (c) bone. Each color corresponds to three different instants, namely, pulse #100, #250 and #400 after the ablation starts. Evolution of the corresponding TOFD is shown in (d)-(f).	39
2.4	(a)-(c) Distribution of the estimated speed of sound within the incision based on measurements performed on sliced specimen. Green lines correspond to the linear fit through the scattered data. Examples of real-time incision depth estimations for the tissue samples in Figure 2.3 are presented in (d)-(f). Actual photographs of the sliced samples are shown in (g)-(i), respectively.	41
2.5	Cross-sectional photograph taken after completion of ablation and post-ablation OA image corrected for fluence decay. The three differential tissue stages of coagulation can be identified: Highly coagulated, mildly coagulation and non-coagulated tissue.	43
2.6	Design and application of the combined RF and OA catheter. (a) Catheter ablation tip, comprising copper-coated light guides embedded in a steel ferule using high-temperature epoxy. (b) Proximal end facet of the catheter, optimized for high light coupling efficiency. (c) Distal end facet of the catheter, delivering both RF current and pulsed-light illumination. (d) Fully assembled bundle. (e) Layout of the combined RF-OA monitoring experiment.	45
2.7	Characterization of the RF-OA catheter. (a) Experimental arrangement for OA imaging. (b) Reconstructed volumetric OA images of the phantom containing signals generated by the absorbing layer (P) and the catheter tip (C) as well as the signal reflected by the catheter tip (R). (b) Maximal intensity projection (MIP) along the x direction. (c) Corresponding MIP image made along the depth direction. (d) Top- and side-view photographs of lesions generated.	47
2.8	Real-time OA monitoring of RF ablation in ex-vivo porcine heart tissue. (a) OA images acquired from unablated tissue. (b) Noninvasive OA imaging of the lesion formation in 3D. (c) OA image acquired after the cooldown phase along with the photograph of coagulated area from a sliced specimen. Images on the top are top-view MIPs while the bottom row shows a single (z-y) slice through the center of the reconstructed OA volumes, as indicated by the white-dashed line in (a). (d) Time evolution of the OA signal during and after RF ablation in the locations indicated in panel (b).	48
2.9	Theoretically calculated water Grüneisen coefficient and OA pressure amplitude induced in aqueous solution as a function of temperature [119].	51
2.10	Volumetric optoacoustic monitoring during photothermal therapy [33].	52

2.11 OA temperature estimations in a tissue mimicking phantom. (a-c) Transverse and coronal maximum intensity projection (MIP) OA images reconstructed for three different time points during laser heating of the phantom; (d) The temperature increase estimated from the OA signal variations (dashed curves) as compared to the temperature increase measured with thermocouples (solid curves). The regions of interest (ROIs) considered for the estimation are marked in panel a; (e) Relative deviation of the F factor from the theoretical value as a function of the temperature increase [33].	54
2.12 Volumetric OA monitoring of temperature during photothermal therapy performed in a mouse post mortem. (a) Transverse and lateral MIPs of the reconstructed OA volumes at different time points during the treatment. The tip of the ablation fiber is located approximately at the center of the displayed volumes. (b) Transverse and lateral MIPs of the estimated temperature maps at the same time points. (c) Actual temporal traces of temperature from the points labeled in (a). [33] . . .	57
2.13 Real-time optoacoustic temperature monitoring during photothermal therapy video screenshots. Left: Volumetric OA image sequence. Right: Volumetric sequence of the estimated temperature maps during laser ablation. [33]	59
2.14 Schematic view of the experimental setup. (a) Drawings of the transducer array and the US system. (b) Transverse MIP optoacoustic images of the front and side views of the phantom. (c) Optoacoustic temperature validation (dashed lines) using the approach proposed in this section. The thermocouple readings (continuous lines) from the same color, represent the two different US heating procedures, at 255 (blue) and 125 (red) cycles.	61
2.15 MIPs of the differential 3D OA images along the z and y directions from ex-vivo bovine tissue for the US focus located at a reference position right underneath the tissue surface (a) and at 1.5 mm (b) and 3 mm (c) points deeper than the reference position, respectively. Scalebar – 5 mm.	62
2.16 Volumetric OA monitoring of temperature during MIFU therapy performed in an ex-vivo bovine tissue. (a) MIPs of the estimated 3D temperature increase maps at different time points along the procedure. Scalebar – 5 mm. (b) Temporal profiles of the estimated temperature increase for the 3 points labeled in (a) with their respective color. . . .	63
2.17 Optoacoustic pressure amplitude induced in canine liver during conductive heating and passive cooling. The triangles represent heating without coagulation; circles – heating with coagulation; squares – passive cooling of the sample. [124]	65
2.18 Schematic view of the experimental setup of the ablation experiment. (a) Drawings of the OA transducer array and RF system network. (b) Schematic synchronization diagram of the OA and RF excitations and acquisition routines.	67

2.19 Computational method for estimation of coagulated lesion size during RF ablation by means of the OA signal derivative. The higher panel shows the OA signal increment based temperature computation, the panel below plots the OA signal derivative.	68
2.20 Lesion boundary progression dimensions for width (w) and depth (d) of the ablated tissue displayed with continuous and dashed lines respectively. Applying the OA signal derivative method (blue), the standard 50°C temperature coagulation threshold method (green) and the iterated temperature threshold attaining similar final lesion size as the direct OA derivative method, results in 60°C. (b) Coagulation boundary regions overlaid on top of the actual fluence-corrected OA images at different time-points during the treatment and the post-ablation cross-sectional view of the porcine tissue sample.	70

Abbreviations

RF	Radio-frequency
OA	Optoacoustic/Photoacoustic
US	Ultrasound
LITT	Laser Induced Thermo therapy
HIFU	High Focused Ultrasound
RFA	Radio-frequency Ablation
GPU	Graphics Processing Unit
AC	Alternting Current
DC	Direct Current
ECM	Extracellular Matrix
IR	Infrared
CT	Computed Tomography
MRI	Magnetic Resonance Imaging
TUS	Therapeutic Ultrasound
ITU	Intense Therapy Ultrasound
LIPUS	Low Intensity Pulsed Ultrasound
MIFU	Medium Intensity Focused Ultrasound
CW	Continuous Wave
FOS	Fiber Optic Sensor
FBG	Fiber Bragg Grating
PRF	Proton Resonance Frequency
NIR	Near Infrared
SNR	Signal to Noise Ratio
ACT	Air-Coupled Transducer
DAQ	Data Acquisition
TOFD	Time Of Flight Difference
ARFI	Acoustic Radiation Force Impulse
ELT	Endovenous Laser Therapy
ROI	Region Of Interest
MIP	Maximum Intensity Projection
MSPS	Mega-samples per Second

Physical Parameters

Grüneisen Coefficient	Γ	Dimensionless
Volume thermal expansivity	β	K^{-1}
Sound Speed	C_s	$m \cdot s^{-1}$
Specific heat capacity at a constant pressure	C_p	$kJ/kg^\circ C$
Absorption Coefficient	μ_a	cm^{-1}
Scattering Coefficient	μ_s	cm^{-1}
Effective attenuation coefficient	μ_{eff}	cm^{-1}
Optical Fluence	ϕ	J/cm^2
Anisotropy Factor	g	—
Heat Capacity at constant pressure	C_p	$J/(kg \cdot K)$
Heat Capacity at constant volume	C_v	$J/(kg \cdot K)$
Material density at reference temperature	$\rho(T_0)$	kg/m^3
Reflection Energy coefficient	R	—
Transmission Energy coefficient	T	—

Chapter 0

Summary

Chapter 0

Summary

Motivation and Objectives

Thermal therapies are widely employed in clinical practice, from selective ablation of cancerous tissues, benign hyperplasias and varicose veins to elimination of subcutaneous fat, cardiac arrhythmias and enhanced drug delivery. Several sources have been considered for tissue heating such as laser light, focused ultrasound (US) and radio-frequency (RF) current.

Most current ablation treatments are tracked via monitoring of indirect parameters associated to the ablation procedure, such as output power, maximum surface temperature or total treatment duration. The lack of reliable feedback during the intervention generally leads to treatment and post-treatment performances built on the skills of the physician. Ablation size can then be over or under estimated, resulting on either insufficient tissue coagulation or undesired damage to healthy tissue. For example, laser surgery has emerged as an advantageous alternative to scalpel-based procedures as it enables minimally invasive interventions with less collateral damage. However, the lack of haptic feedback and real-time control over the lesion profile limit the applications and broad use of this approach.

The goal of this thesis is to investigate on the capabilities of optoacoustic/photoacoustic (OA) imaging and sensing methods as a monitoring approach for different types of ablation procedures. In this context, we focus on the following objectives

1. To study of the feasibility of noncontact monitoring of incision depth in laser surgery.
2. To develop new algorithms to compute volumetrically the temperature distribution in real-time from temperature-induced OA signal increases.
3. To quantitatively assess thermal treatment procedures, e.g. by imaging or monitoring the lesion, incision or temperature maps generated using radio-frequency ablation and medium intensity focused ultrasound.

Outline

The thesis is organized as follows. Chapter I begins with a description of the mechanisms of ablation during thermal treatments, explaining the effects of temperature in biological tissues. The limitations of current monitoring approaches for different thermal ablation processes are described. Subsequently, the OA effect and the tissue parameters involved are described to establish the mathematical background of OA imaging. The OA equation is introduced, its solution is derived and reconstruction strategies are discussed. The spectral capabilities of OA imaging in current biomedical imaging are also outlined. Moreover, the basics of ultrasound (US) detection and the main image formation approaches are described. Particularly, recently-developed real-time OA imaging systems used in this thesis are introduced. These systems capitalize on the rapid development of acoustic detection transducers, laser technology as well as Graphics processing units (GPU) architectures to provide previously unachievable imaging capabilities.

Chapter II details the methodology followed in the thesis for the application of OA imaging in ablation treatments monitoring. First, an overall description of the OA capabilities for thermal ablation monitoring is provided. Subsequently, details on

the use of a focused high-intensity pulsed laser for the generation of shockwaves that retrieve the incision profile depth are provided. Shockwaves have much higher intensity than OA waves, but both have in common being generated with a short-pulsed laser. The next sections encompass the use of OA contrast for thermal ablation monitoring and the previously suggested temperature monitoring techniques. The capabilities of OA to become a temperature monitoring tool are also described. This is followed by empirical calibration results that enable rendering volumetric optoacoustic monitoring of temperature during photothermal therapy with the introduced approach. The limitations of state-of-the-art methods are further discussed. Chapter II ends by focusing on the development of a real-time coagulation trigger technique that can advance deep early coagulation detection by means of OA tomographic imaging.

Chapter III is dedicated to the presentation of the information sheet and manuscripts corresponding to the peer-reviewed journal publications published during the thesis. Chapter IV provides final remarks, future research directions and conclusions of the thesis.

Chapter I

Background

Chapter 1

Background

1.1 Thermal Ablation Treatments

Thermal ablation therapies have been widely employed in general clinical practices for applications ranging from targeted ablation of unwanted tumoral tissue, benign hyperplasias and varicose vasculature to subcutaneous fat removal, cardiac arrhythmias and enhanced drug delivery [1–6]. Thermal ablation, namely thermotherapy, is the use of heat energy with therapeutic purposes. The heat generation process can be induced by several heat sources including laser light (LITT) [7, 8], high intensity focused ultrasound (HIFU) [9], radio-frequency electrical energy (RF) [10] and microwave radiation [11]. The energy source is then applied in the undesired tissue volume, after an initial temperature rise of the surrounding tissue, cell denaturation drives coagulation and with further exposure carbonization and tissue removal levels are achieved.

The ablative capability of heat treatments has been increasingly applied in a wide range fields with therapeutic purposes such as oncology, ophthalmology and cardiology. The most widely used thermal ablation technique is Radio Frequency Ablation (RFA). RFA is based on the insertion in the tumor of a needle like catheter. The catheter is connected to a RF current generator and the return circuitry is typically

arranged with the placement of a ground pad attached to the leg of the patient. Ablative current applications involve the generation of heat by the flow of an alternative current through the tissue targeted for ablation. Currently, high frequency alternating current (350-500 kHz) RF ablation is preferred over previously used low frequency AC or DC pulses, the benefit is found in a lack of electrical muscle tissue stimulation for cardiac applications where hence general anesthesia is not required.

Figure 1.1 depicts clinical application of radio-frequency thermal ablation. In order to be therapeutically effective, the thermal ablation must be performed in a volume confined to the targeted region so that undesired tissue damage is avoided. The targeting of a tumor remains as a challenging task to achieve since the optimal lesion geometries vary with different ailments. After the exact volume of ablation is targeted, electric current is conducted through an electrode at the catheter tip.

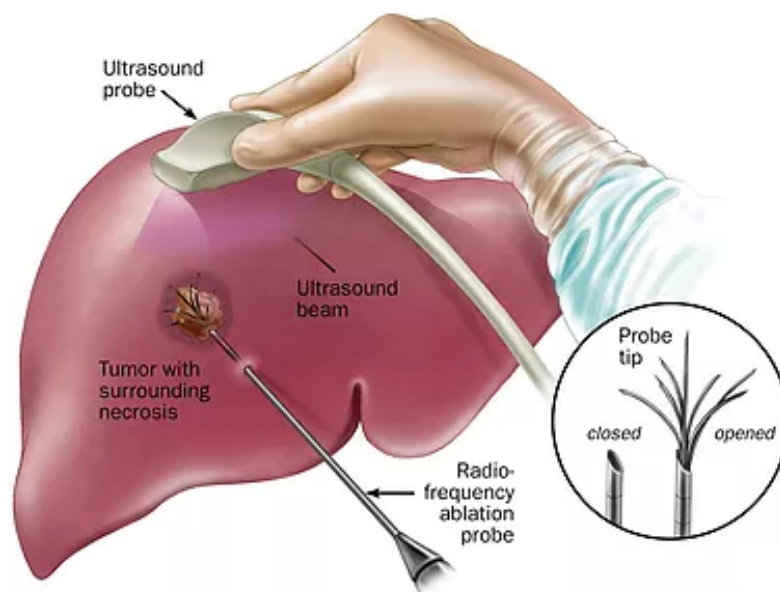


FIGURE 1.1: Clinical setup of radio-frequency thermal ablation being monitored with pulse-echo ultrasound. Multi-tine catheter tip is positioned in the targeted tissue volume. Image courtesy of Mallinckrodt Institute of Radiology. ©

Specifically in some thermal RFA applications, such as liver ablation, the ablation electrode has a multi-tine tip geometry for a better electrical energy deposition in the tumor vicinity as the detail shows in Figure 1.1 In RFA ablation the electrical current,

by means of the Joule effect, leads to resistive heating of the tissue sample and consequently temperature rises that drive coagulation and irreversible tissue denaturation effects. The contact area at the ablative catheter tip is relatively smaller to that of the ground pad, therefore the current density is bigger in the electrode and tumor spot. Thermal ablation is consequently delivered in the vicinity of the catheter tip, yielding typically lesion profiles of several millimeters.

Currently the most commonly used thermal techniques, and the main focus of this thesis, are laser ablation or laser induced thermotherapy (LITT), high focused ultrasound (HIFU) and radiofrequency ablation (RFA).

1.2 Effects of Temperature on Biological Tissue

The application of continuous heating during thermal ablation procedures leads to tissue denaturation and eventually coagulation, carbonization and removal of the ablated tissue volume. Minimally invasive thermal therapy has been explored as a means of treating small solid tumors [12]. It involves heating the target tissue to temperatures between 50°C and 95°C for several minutes which results in coagulative necrosis. This is differentiated from hyperthermia, which involves lower temperature applications ranging between 40° to 45°C, and it involves longer and multiple thermal dosages as well as in conjunction with the use of multi-fractioned radiation or chemotherapy.

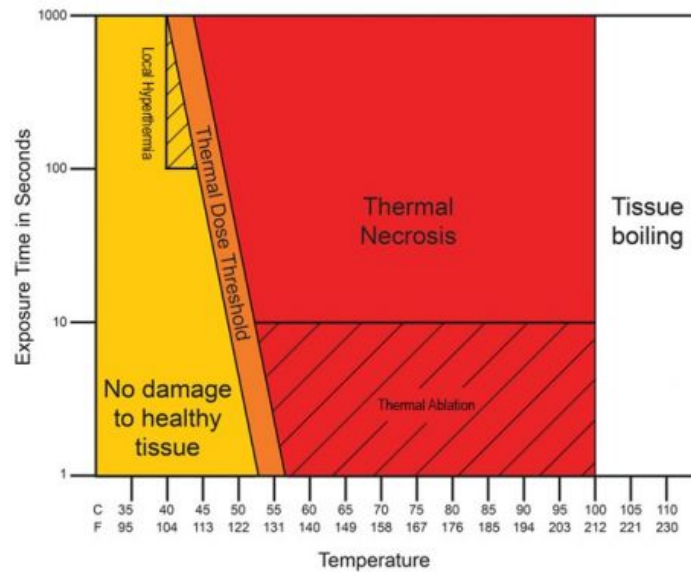


FIGURE 1.2: Thermal effects in tissue as a function of temperature and exposure time [132]. As the temperature decreases, the exposure time needed to achieve thermal necrosis increases exponentially. Temperature and exposure times generally used for both local hyperthermia and thermal ablation are marked. Tissue water boils above the threshold of 100 °C regardless of the exposure time.©

Body temperatures are typically found at 37 °C, approximately for the first 1.5 °C or so of heating few irreversible alterations take place. At 41 °C a range of effects, namely hyperthermia starts. Cell proteins, both membrane and cytoplasmic proteins, begin to undergo structural changes. They change conformation because the hydrogen bonds keeping them in their native state are broken down by the increasing collisional energy of the molecules as the temperature increases. When a molecule suffers shape changes it is no longer fully operational and able to achieve its function within the cell. For example, when enzymes, whose catalytic functions depend crucially on their shape, start to deform, reaction rates within cells slow down. Even at small increases in temperature some cells will die because of these effects. The rate at which cell necrosis occurs, namely apoptosis, increases with the temperature. From 45 °C the collagen fibers forming the extracellular matrix (ECM) begin to shrink as the trihelical structure of the collagen breaks apart. The optical scattering in the tissue increases, it whitens if we think of frying a chicken breast, then the collagen softens and gelatinizes (gelatin). Tissue begins to coagulate and blood starts to clot

[13]. In many clinical applications tissue is regarded as fully coagulated when heated at a transient temperature of 43 °C for a time span of 240 min [14]. Previous studies have noted that for each temperature exposure degree increase above 43 °C, there is a two-fold drop in the exposure time required to achieve the same biological denaturation effect [15]. Consequently, at temperatures above 50 °C the biological tissue will be fully coagulated in few seconds. Herein, when monitoring ablation treatments, 50 °C is widely accepted as a critical temperature threshold above which biological tissue can be regarded as necrosed and fully coagulated defining the lesion volume. In order to avoid charring and micro-explosions it is necessary to control the tissue temperature not to go above 100 °C, exceeding that temperature the water in the cells and extracellular fluid boils, which leads to the formation of steam bubbles and can result in carbonization. The huge volume expansion as the water transitions phase, vaporizes, can lead to tissue being expelled from the tissue sample surface. Once all the water has boiled off, the remaining organic material may char (blacken). At even higher temperatures it will eventually evaporate.

A critical parameter to take into account in laser surgery is the deposited ablation energy threshold. Under thermal confinement conditions, if the radiant exposure of a single laser pulse is above the targeted tissue-specific threshold, the irradiated tissue will show an explosive vaporization of intracellular water, leading to the ejection of water vapor and tissue fragments [16]. In this manner, a certain tissue volume will be ejected and will create a differential incision. A fraction of the remaining incident light reaches depths where the light energy is not enough to immediately eject tissue and will consequently be converted into heat and will result in a tissue temperature increase. Specifically, there will be a tissue-specific repetition rate for which the inter-pulse time is not enough for heat dissipation, thus at high repetition rates (>20 Hz) the latter effect will be pronounced being able to accumulate over time and lead to coagulation and eventually carbonization in the remaining tissue.

1.3 Laser Surgery

Monitoring of most commonly used ablation procedures rely entirely on indirect indicators of ablation activity, such as the delivered power, the overall duration of the treatment or the temperature profile retrieved from few locations using point-wise sensors. Estimations of the lesion geometry growth based on indirect indicators remain inaccurate and mostly irreproducible in similar procedures, yielding assessments highly sensitive to medical experience and training. The post-ablation final lesion size might therefore be over- or underestimated. This in turn leads to an extent of tissue damage that could result insufficient, which would require post-operative treatments, or excessive, in a way that the damage extent would reach healthy tissues. Damaging healthy tissues can additionally lead to clinical problems with potential life-threatening consequences such as liver failure, pleural complications, venous thrombosis or cardiac tamponade [17]. In a similar manner, lack of haptic feedback in laser surgery leads to difficulties determining the incision depth and incised tissue type causing a high risk of collateral damage to tissues that need to be optimally functional, e.g. organs or nerves [18]. Direct judgment of the ablation development, for example by imaging the lesion depth during the procedure, can accurately provide real-time feedback on the lesion size growth. Accurate assessment of the ablation extent can greatly improve real-time decision making, resulting in higher success rates and an advanced clinical applicability of laser-based surgery and thermal ablation procedures.

Laser surgery is an advantageous alternative to scalpel-based procedures, which are often afflicted with excessive mechanical traumatization and bacterial contamination. Pulsed laser ablation results in vaporization and ejection of tissues, leading to generation of laser-induced shock waves at the incision spot. This ablation mechanism is already exploited in an ample spectrum of laser-tissue applications such as laser osteotomy [19] or, soft and connective tissue cutting in dermatology, ophthalmology or oncology [20–24].

Currently, there are several optical and acoustic readout mechanisms that have been

proposed for monitoring laser surgeries [25–27, 27, 28]. However, the lack of accurate haptic feedback and real-time control over the lesion profile still remains a major challenge of laser-based surgical procedures, severely limiting the range of potential applications. Monitoring of the laser incision depth also has been attempted using kinesthetic and vibrotactile haptic feedback [29], however these studies conveyed only initial demonstrations in homogenous agarose phantoms for a limited shallow penetration depths of 1 to 2 mm. Furthermore, acoustic detection of shock waves was used to demonstrate the capability of monitoring of incision depth during laser ablation. This was achieved, by using a matrix array of ultrasound detection elements for 3D localization of the incision profile in ex-vivo samples [30]. However, the need of an acoustic matching medium, typically in the form of water or ultrasound gel, between the ablated tissue and the feedback detector may affect the achievable ablation rate by altering the effective heat capacity of the tissue surface while the contact-based approach may further hamper the general applicability of such monitoring method in a real clinical setup.

1.4 Laser Induced Thermotherapy (LITT)

Techniques based on hyperthermia are largely employed in clinical practice to treat cancer. These procedures induce a temperature increment within a carcinogenic body tissue. Laser-induced thermotherapy is spreading as a technique to induce localized hyperthermia. LITT is a minimally invasive surgical technique, in which the radiation emitted by the laser source is guided by a fiber optic within the tissue to be treated. The laser energy absorption leads to a localized heating able to induce cellular necrosis. LITT ablation has been widely used for the treatment of various tumors e.g. in the, liver, lungs, prostate, brain or pancreas [31, 32]. Temperature values reached within the tissue play a crucial role in the outcome of LITT interventions while the spatial temperature distribution and exposure time defines the volume of coagulation and thus the amount of tissue volume undergoing thermal driven denaturation. Therefore, the monitoring of temperature increase during LITT provides useful feedback in order to adjust laser dosimetry. An effective laser therapy

outcome is crucial in interventions aiming to remove the neoplastic volume entirely without collateral thermal damage to the surrounding healthy tissue. Therefore, the monitoring of temperature has been considered essential in all hyperthermic treatments. In the last decades, the need of new temperature monitoring methods for thermal therapies, and in particular in LITT, facilitated the introduction of several thermometries. Invasive approaches based on thermocouples or fiber-optic sensors can be used for temperature monitoring. In this way, the temperature can only be captured in few locations within the heated region. Also, direct tissue contact or an invasive approach are required. On the other hand, the temperature map can be obtained using non-invasive imaging modalities such as optical methods, infrared (IR) thermometry, US, x-ray computed tomography (CT), or magnetic resonance imaging (MRI). However, these imaging modalities are either limited by low penetration depth, sensitivity, contrast or otherwise lack an adequate temporal resolution for dynamic mapping of the temperature fields [33].

1.5 High Focused Ultrasound (HIFU) Treatments

Therapeutic ultrasound (TUS) involves a wide range of techniques routinely employed in the clinics to treat pathological tissues, such as tumors, neurological disorders, kidney stones, blood clots, injured muscles and tendons or hemorrhages [34]. The majority of US-based treatments involve thermal effects produced via tissue heating with average intensity levels exceeding those permitted for diagnostic purposes. High-intensity focused ultrasound (HIFU) is used to selectively destroy abnormal tissues, such as cancerous neoplastic tumors, via exposing the targeted tissue to local temperature elevations in the coagulation range [35, 36]. HIFU has also been used at lower power levels below the threshold required for ablation, such as in intense therapy ultrasound (ITU), by creating thermal injury zones in the tissue, initiating tissue repair cascade, promoting collagen generation and thus a healing response [37, 38]. Low intensity pulsed ultrasound (LIPUS) is also used in applications driving beneficial tissue healing responses [39]. Additionally, non-thermal physical

effects, such as cavitation and acoustic streaming, have shown to promote cell membrane permeability and improve cellular activity [40]. Medium intensity focused ultrasound (MIFU), with acoustic intensity levels between those used in echography and HIFU that can lead to combined and cooperative thermal and non-thermal physical effects in soft tissues for performing physio or cancer therapy, either directly or via local drug delivery.

When focused ultrasound is used in a continuous-wave (CW) mode, the temperature reached at the focal point can achieve a cumulative thermal dose great enough to kill the tissue by coagulative apoptosis. This process works through the denaturation of the cellular membrane and can be focused to a volume as small as 10 mm^3 [123]. Mechanical destruction at the cellular level occurs if US is used in a pulsed manner, as opposed to the CW mode of operation. The cumulative thermal dose will be lower, so that the effects on the tissue will be due to mechanical interactions. At high enough acoustic intensities, microbubbles will form around cells and through their oscillations, fracture the cell membrane. The interaction of ultrasound with the microbubbles is known as cavitation, also when it is used to mechanically destroy the tissue it is called histotripsy.

Effective application of focused US energy requires precise monitoring of the spatio-temporal temperature distribution map during the clinical intervention, control over the delivered US intensity levels and duration of the treatment as well as precise spatial targeting in the body [41]. Thereby, the development of efficient monitoring methods is paramount for improving the therapeutic efficacy while avoiding unnecessary tissue damage. Of particular importance is the feasibility to render real-time feedback on the spatio-temporal temperature distribution in the treated tissue. Temperature monitoring is also essential in MIFU for controlling the exposure time at lower temperatures and preventing overheating. Intrusive temperature monitoring methods based on thermocouples, thermistors or fiber-optic detectors can be used for temperature control [42]. However, these invasive approaches only retrieve temperature readings from discrete locations. Mapping the temperature distribution was further attempted using non-invasive imaging approaches, including infrared thermometry [43], analysis of US backscattered signals [41, 44], X-ray CT [45] or MRI

[46]. However, all these methods have limitations for real-time volumetric temperature mapping.

1.6 Radiofrequency Ablation (RFA)

Radiofrequency ablation is used for coagulation and destruction of dysfunctional tissues e.g., in cardiology where the target is the elimination of abnormal electrical pathways responsible for cardiac arrhythmias [47]. RFA drives localized coagulation and desiccation of the target tissue while avoiding uncontrolled apoptosis in the neighboring tissue structures. The ablation procedure is generally guided by electrophysiological and anatomical mapping as well as by careful RF titration [48]. The size of the induced lesion is mainly determined by the extent and duration of the heat-affected area. Hence, real-time treatment monitoring is essential to optimize the outcome of the ablation procedure. The ablative process is typically monitored via simple temperature or impedance measurements at the ablation tip [49, 50]. However, heat diffusion and the use of irrigated ablation tips can significantly affect the size and shape of the ablated area, resulting in failed treatments [51]. Up to now, multiple imaging techniques have been proposed for RFA lesion formation monitoring. MRI has shown capabilities for monitoring thermal treatments [52]. However, limited resolution, high costs and specialized equipment prohibit MRI-based techniques from becoming commonplace in regular RFA treatments in general clinical practice. Emerging as an alternative, US-based techniques have been proposed, however pure pulse-echo US based imaging lacks enough clear lesion contrast, while more advanced US-based methods still fall short of providing direct lesion imaging at acceptable temporal resolution rates [53]. Alternatively, pure optical imaging techniques lack enough penetration depth for providing meaningful lesion monitoring feedback.

1.7 Temperature Monitoring Techniques

This section presents an overview of the techniques used to monitor tissue temperature during thermal ablation that are currently used by physicians in clinical practice.

1.7.1 Invasive Approaches for Temperature Monitoring

This subsection focuses in the description of the three most widely used invasive approaches for temperature monitoring. The need to introduce the sensing element within an organ is the main drawback of these methods, which require direct contact with the measurement site. Furthermore, since the outcome of the ablation intervention is related to the distribution of tissue temperature, a number of sensors are required. These techniques are classified as invasive approaches, even though efforts are dedicated to the minimization of the number of necessary probes for the thermal mapping.

Temperature monitoring using thermocouples

Thermocouples are widely used because they are mostly cost-effective, attain high levels of accuracy, have a wide measurement range, small detector size and rapid response. These advantages make thermocouples suitable for localized monitoring of temperature when fast temperature changes are produced [42]. The concerns of using thermocouples during thermal ablation are related to the invasiveness of the measurement and their metallic constitution. Metallic conductors, main components of the thermocouple junction, can become unnecessary absorbers of radiation during specific thermal ablation techniques like laser light radiation. This phenomenon causes a local increase of temperature, entailing a significant overestimation of the actual tissue temperature. Despite this artefact, thermocouples are widely used, particularly unshielded thermocouples facilitate reducing the size and provide a short response time. The use of shielded thermocouples overcomes the fragility of unshielded ones at the expense of an increase of the response time and size.

A thermocouple consists of two metal wires joined in two junctions. The electromotive force of the open circuit is a non-linear function of the temperature difference between the two junctions. During an ablation procedure, the two conductors, usually embedded in an implantable needle, strongly absorb the energy used for ablation, e.g. US, microwave or laser light, thus inducing an error in the temperature measurement. This is a main concern, along with the invasiveness, resulting in a significant overestimation of the actual surrounding tissue temperature [92]. A useful technique to perform a more accurate correction of the associated artefacts is based on the repetition of ablative energy switching on and off in order to measure the amplitude of the artefact by averaging its value on several cycles [42]. The use of thermocouples has been reported in several studies dedicated to temperature monitoring during thermal ablation in different tissues, among others, retina [93], liver [17], and benign prostatic hyperplasia [94]. However, the overestimation of temperature and the limited number of thermocouple sensors needed to avoid clinical trauma still remain as main drawbacks for this temperature detection mechanism.

Temperature monitoring using fiber-optic sensors: FBGs and fluoro-optic probes

There are many types of fiber-optic sensors (FOS) used for temperature measurements. The widespread use of FOS, and in particular of fiber Bragg grating (FBG) sensors, has been delayed by the high equipment costs and by the relatively low interest of the medical community. Currently, there are two main FOS for thermometry, namely FBG sensors and fluoro-optic probes.

FBGs are periodical perturbations of the refraction index of an optical fiber [95] photo-inscribed within the core of the fiber. The working principle of FBGs is based on the detection of a wavelength shift ($\Delta\lambda_B$) due to change of temperature or strain. The Bragg wavelength (λ_B) is expressed by equation 1.1:

$$\lambda_B = 2n_{eff} \cdot \Lambda \quad (1.1)$$

where n_{eff} is the effective refractive index of the fiber core, and Λ is the period of index modulation. When a broadband light source propagates within the fiber, a

narrowband spectral component centered at λ_B is reflected by the grating. A perturbation of the measure causes a λ_B shift ($\Delta\lambda_B$), which can be considered an indirect measurement of temperature or strain. $\Delta\lambda_B$ depends specifically on temperature changes (ΔT) because of the thermal expansion of the fiber material (changes of Λ), and on the temperature dependence of n_{eff} . When FBGs are employed as temperature sensors, the contribution of strain changes on $\Delta\lambda_B$ are neglected with respect to ΔT [42]. FBGs are of interest in the biomedical field [96] due to their electromagnetic inert nature, the small size, the biocompatibility, the non-toxicity and chemical inertness and the capability to be encapsulated into thin and flexible optical fibers. A number of gratings can be easily embedded into a single fiber, constituting a distributed FBG sensor, since the nominal λ_B is different, and they can be interrogated by the same optical spectrum analyzer.

Fluoroptic sensors are based on the fluorescence decay time of a special thermo-sensitive phosphor, such as magnesium fluorogermanate, located at the end of a fiber-optic cable [97]. The decay time of the phosphor is a function of temperature of the phosphor itself, see Figure 1.3. An excitation light pulse generated by a source propagates through the fiber and excites the phosphor layer at its extremity. The fluorescent signal generated by the exciting phosphor is sent back within the same fiber. After the excitation, the fluorescent signal decays with an exponential law which depends on the temperature of the phosphor. The correlation between the decay time and the temperature of the fluorophore allows an estimate of the temperature at the end of the fiber [98].

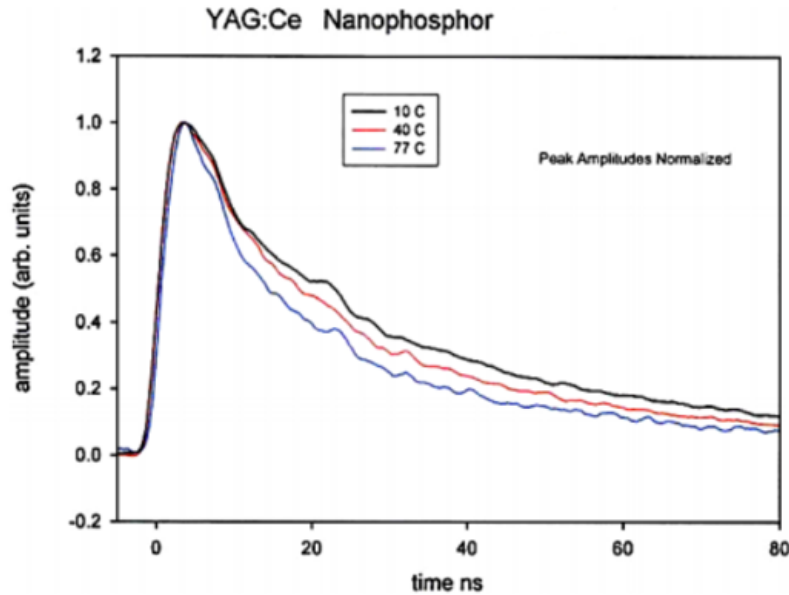


FIGURE 1.3: Representative signals versus temperature for $\text{Y}_3\text{Al}_5\text{O}_{12}:\text{Ce}$. Peaks at all three temperatures were normalized to the same height for comparison purposes. (top trace, 10°C , middle trace 40°C , bottom trace 77°C). [99]

In a fluorescence thermometry study [99], Allison et. al. assumed a fluorescence single exponential decay model with temperatures ranging from 10 to 77°C , and could observe that the captured signals fall at a rate that is faster than a single exponential decay during the first 20 ns. However, at times > 20 ns the signal fall less rapidly than the simplified model. Simons et. al. [100] proposed a simple model aimed at describing how strongly the fluorescence lifetime of a material depends on its temperature. The model has only one free parameter Q . The expression is the following:

$$\frac{\tau}{\tau_0} = \exp[Q(T - T_0)] \quad (1.2)$$

The reciprocal of Q is the temperature change needed for the decay time to decrease by $1/e$. From an instrumental perspective, Ce-doped nano-phosphors provide a short decay time that makes the fluorescence signal easier to acquire and analyze in comparison with phosphors with ms decay times when the same number of photons are emitted and detected in both cases. The reason for this improvement is that the peak

values of the signals are greater and the rise times are faster, thus reducing triggering errors in detection electronics. Fluoroptic probes can cover a large temperature range, typically from 25°C to 300°C and an accuracy of 0.2°C, are electromagnetically inert to interferences and biologically compatible.

1.7.2 Non-invasive Approaches for Temperature Monitoring

The growing interest in medical imaging techniques for temperature monitoring is motivated by their non-invasiveness and the possibility to obtain a temperature map around the therapy applicator. The aim is to avoid the insertion of several sensors and therefore minimize the dimension of operative tools to be introduced within the body. The following subsections describe the fundamental advantages and drawbacks of CT, MRI and US-based thermometry.

CT-based thermometry

CT-based temperature monitoring has recently been advanced to provide effective feedback in hyperthermia dosimetry due to technological improvements in CT scanners [101]. Patient exposure to X-ray radiation is the most important concern of using CT scanners. However, the non-invasive nature of this technique make the use of CT-based thermometry during hyperthermia interesting in certain cases [42].

A basic understanding of the fundamental physics of CT image formation is necessary to describe the thermometry process. An image obtained by CT scan is composed of pixels, which display the average X-ray attenuation properties of the tissue in the corresponding voxel. A limited amount of X-ray radiation is transmitted through the patient, and detectors at the opposite side. The intensity of transmitted X-rays depends on the linear attenuation coefficient, μ . A single image is obtained via mathematical reconstruction from the measured attenuation values at a large number of projections. The value of each pixel of the image is finally converted into the CT number, called Hounsfield(HU) unit. The CT number is obtained by the following relationship [105]:

$$CT(x, y) = 1000 \cdot \frac{\mu(x, y) - \mu_w}{\mu_w} \quad (1.3)$$

where μ_w is the attenuation coefficient of water, and $\mu(x, y)$ is the average linear attenuation coefficient in the pixel located at (x, y) . The value of $\mu(x, y)$ depends on the interaction mechanism between tissue and X-ray radiation. During CT scans, this is partly due to Compton scattering. Therefore, the temperature dependence of physical parameters which influence Compton scattering is the basis of the CT thermometry image formation. A simplified description of the temperature influence on CT can be performed by considering that μ tracks linearly with the tissue physical density (ρ).

The change μ depends on the thermal expansion. In fact, the density of a material at a generic temperature, T, can be expressed as [105]

$$\rho(T) = 1000 \cdot \frac{\rho(T_0)}{1 + \alpha \cdot \Delta T} \quad (1.4)$$

being $\rho(T_0)$ the material density at a reference temperature (T_0), α the volumetric expansion coefficient, and $\Delta T = T - T_0$. Since the linear relationship between CT and density, considering the previous two equations and after performing a linearization based on a Taylor series expansion in $\alpha \Delta T$ [102], we can obtain [105]

$$\Delta CT \approx - [1000 + CT(T_0)] \cdot \alpha \cdot \Delta T \quad (1.5)$$

where $\Delta CT = CT(T) - CT(T_0)$ is the difference in CT, when temperature changes from T_0 to T. Pandeya et al. studied CT thermal sensitivity in ex vivo swine livers, showing a sensitivity of $-0.54 HU^\circ C^{-1}$ heating the target with a hot air flux from 20 to 95°C [103]. Pandeya et al. also studied the CT thermal sensitivity in ex vivo bovine liver, by heating the tissue with RF energy from 20 to 98°C, showing a sensitivity of $-0.60 HU^\circ C^{-1}$ [104].

The ideal requirements for a non-invasive temperature monitoring during hyperthermic ablation therapies include an accuracy of 2°C, a spatial resolution of 1-2 mm, and an acquisition time lower than 10-30s [51]. Experiments on water, other fluids and biological tissues [105] are promising and appear to match the mentioned requirements. Furthermore, a CT scanner does not require special devices with respect to non-invasive thermometry based on MRI.

Ultrasound-based thermometry

In US imaging, high-frequency sound waves, typically between 2 to 15 MHz are transmitted into biological tissue and partially reflected back to the probe in internal structures, being the delay between transmitted and received ultrasound an indirect measurement of the characteristics of the medium. The image is then formed by echoes generated by reflection of ultrasound waves at the boundaries of tissues. Each echo is displayed at a particular coordinate of the image, depending on its relative position within the body cross-section [106].

Several US imaging parameters have been investigated for temperature estimation, such as frequency-dependent attenuation, change in backscattered power and shift in US frequency signal. The frequency signal shift is the most widely employed methodology for temperature monitoring in the US imaging Biomedical Sciences field [107]. Particularly, the time of echo for ultrasound in a homogenous medium is expressed as [107]

$$t(T_0) = \frac{2 \cdot z}{v_s(T_0)} \quad (1.6)$$

where $t(T_0)$ is the time delay of an echo at position z and at temperature T_0 , and $v_s(T_0)$ is the speed of sound in the tissue at temperature T_0 . In the presence of a temperature change ΔT , a time shift Δt , in the ultrasound signal occurs, due to both the thermal expansion of the medium and the change of sound speed. Since the influence of the thermal expansion element is negligible with respect to the change of sound speed and the dependency of time shift with depth can be removed, the dependence between ΔT and Δt can be expressed as [107]

$$\Delta T \approx k \cdot \frac{d(\Delta t)}{dt} \quad (1.7)$$

where k is a tissue constant that can be experimentally determined, and $d(\Delta t)/dt$ is the derivative of the time shift, also called normalized time shift. Thermal images representing heating of tissue are computed by a motion algorithm estimating Δt in consecutive ultrasound frames. Once the normalized time shift is computed, it is then translated into a temperature map.

The temperature resolution in US thermal imaging is strictly related to the motion algorithm adopted. The spatial resolution is mainly influenced by the kernel size employed in the motion algorithm, and by US frequency. An US pulse with higher bandwidth results in images with better spatial resolution at the expense of losing penetration depth. Physiological motion and unexpected acoustic tissue properties changes are also relevant within this approach which could cause artefacts in US thermal imaging. However, artefacts can be removed afterwards by post-processing the US images.

MRI-based thermometry

After the transmission and the successive interruption of a radio frequency signal to a medium, proton spin reacquires the initial position and direction. Two temporal parameters, i.e. spin-lattice relaxation time T1 and the transversal relaxation time T2, quantify the mechanisms of relaxation of the spin proton to recover the equilibrium status, and give information about the structure of the tissue. T2 relaxation time is less appropriate than T1 for temperature monitoring as its temperature dependence is reduced with respect to T1 [108] and can be masked by other factors [109].

In T1-based MRI thermometry, the spin-lattice relaxation in biological tissues results from dipolar interactions of macromolecules and water molecules, which is due to their translational and rotational motion. The temperature dependence of this motion causes an increase of T1 with temperature. The relationship between T1 of water protons and temperature is described by [110]

$$T1 \propto \exp\left(-\frac{E_a(T1)}{k \cdot T}\right) \quad (1.8)$$

where $E_a(T1)$ is the activation energy of the relaxation process, k is the Boltzmann constant and T is the absolute temperature. Within a certain temperature range of interest for hyperthermia purposes (i.e. 30-70°C), the relationship between T1 and temperature can be considered mostly linear.

The quality of T1-based thermal mapping depends on the accuracy in measuring T1. Lipid suppression should be used because of the presence of lipids in biological tissues, which have different T1 change with temperature. Non-linear effects can occur if the tissue properties change, e.g. due to coagulation. Furthermore, since the T1 change due to temperature depends on the tissue type, prior knowledge of the thermal coefficient of each tissue is essential. Because of these issues, T1 changes are often used to get a qualitative measurement of the temperature distribution [111]. The advantage that this technique provides is that it is easy to implement, exhibits high sensitivity to low field strength and low sensitivity to motion.

Proton resonance frequency (PRF) shift is now considered the most promising technique in the field of MR thermometry, that is using the chemical shift that creates the resonance frequency shift of a nucleus with respect a reference element. PRF is preferred because of its independence for aqueous tissues, the linear dependence between electronic shielding and temperature, and the higher precision in mapping temperature changes (uncertainties of $\sim 0.3^\circ\text{C}$) with respect to other parameters [112]. However, some concerns arise related to the small sensitivity to temperature changes of lipid PRF shift that can cause errors of thermal mapping for fat tissue. The main problem that restrains MR thermometry of being implemented in general clinics is the respiratory motion, and several motion-correction techniques are currently discussed and researched [113].

There is no unique parameter offering the highest sensitivity and efficiency in temperature monitoring with MRI [110]. T1 relaxation can be performed with low field ($< 0.5\text{T}$), it shows low motion sensitivity and it is easy to be implemented, although

with the drawback of being tissue-type dependent. Tissue dependence is solved by PRF in aqueous tissues, except for lipid tissues, that shows a linear dependence in the temperature range between -15°C and 100°C and high temperature sensitivity.

The non-invasiveness peculiarity of the thermal ablation imaging methods presented allow them to be subject of research due to their promising applications in the biomedical field. However, the chance of visualizing the ablation procedure in real-time [114] and concurrently estimate the temperature distribution within the treated organ obtained by image-based thermometry is still quite challenging. Therefore, OA capabilities for non-invasively monitoring temperature will be object of consideration in the subsequent sections.

1.8 Optoacoustic Imaging

1.8.1 Light and Sound Propagation in Tissue

Electromagnetic waves, like light, propagate and interact with the structures that compose matter [54]. When photons propagate through biological tissue, they are either scattered or absorbed. Scattering is the deflection of light and is strongest experienced when the scatterer size is in the order of the optical wavelength. Absorption is the uptake process of electromagnetic energy by the electronic and vibrational structures of matter constituents and is intrinsically sensitive to chemical composition [54]. Absorbed light can be converted into heat, utilized in a chemical reaction or radiated back as in fluorescence. Following absorption of a photon, radiative and non-radiative relaxation pathways can take place [13].

Given the photon absorption event in a single excited molecule that does not interact with any other nearby molecules, the molecule can undergo the non-radiative process of “intramolecular redistribution” until the molecule is in equilibrium. Otherwise, the molecule can suddenly shift to a lower energy state by photon emission. If the radiative lifetime of the molecule is shorter than the redistribution time, most likely a photon will be emitted before intramolecular redistribution is completed. In

the same way, there is always partial intramolecular redistribution before a photon is emitted, therefore the energy of the re-emitted electromagnetic particle will be lower than the absorbed photon. There are two possible radiative processes: fluorescence and phosphorescence. While fluorescence is the transition to a similar state, i.e.: singlet-singlet, and usually takes place in the order of few nanoseconds, phosphorescence occurs after an intramolecular crossing has taken place and the transition, i.e.: triplet-singlet, is much less likely to occur, at a lower energy and in the order of milliseconds to seconds timescale, see Figure 1.4.

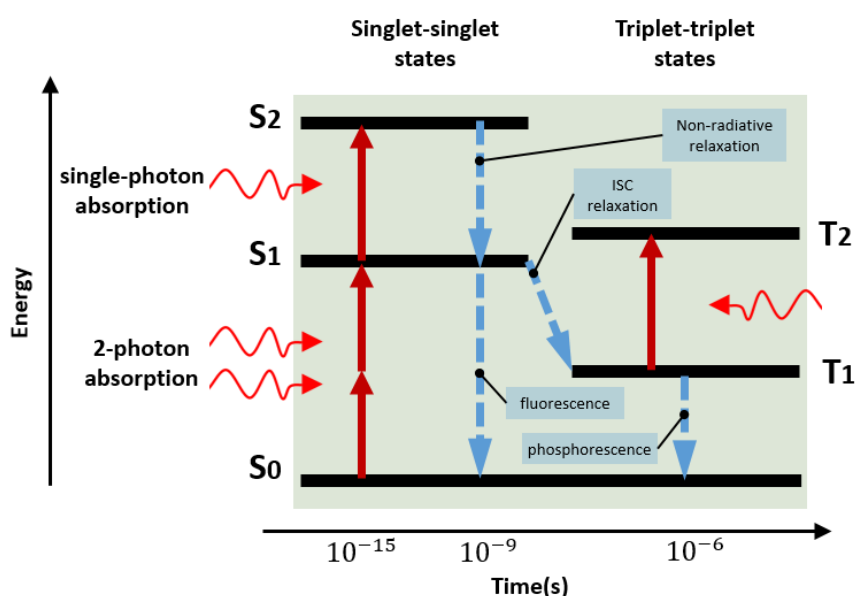


FIGURE 1.4: Optical excitation and relaxation of atoms and molecules from the ground state to excited states can result in fluorescence, phosphorescence, energy transfer, electron transfer, stimulated emission or non-radiative relaxation.

Biological systems are complex organisms constituted by a large number of molecules, where inter-molecule interactions can lead to several processes after a photon is absorbed. Photochemical reactions take place when the electromagnetic energy absorption gives rise to an electronic transition, the more energetic the electron will orbit the nuclei at a greater distance. As the nuclear attraction force decreases notably with distance, the electron will be less tightly bound and will be able to form a chemical bond with another more readily molecule. On the other hand, processes

of thermalization and collisional relaxation happen while an excited molecule is undergoing intramolecular redistribution it might collide with another molecule. Some of the vibrational energy in the excited molecule will be transferred to the colliding molecule as translational kinetic energy. Molecular translational kinetic energy is what appears at a macroscopic level as a temperature rise so leads to photothermal effects. This process of collisional relaxation will thereby thermalize the absorbed photon energy in a matter of picoseconds, although the consequent macroscopic thermal effects occur over longer timescales beyond milliseconds and seconds.

OA imaging exploits optical absorption to target deep biological tissues at millimeters to centimeters from the surface. Anatomical features contain an abundance of chromophores such as hemoglobin, lipids and water that present completely different absorption spectra. Figure 1.5 shows the absorption spectrum of major endogenous chromophores. Optical absorption is minimized within the so-called near-infrared (NIR) optical window, 650 to 1300 nm, and hence this range of wavelengths is preferred for deep-tissue imaging. The absorption coefficients of both the oxygenated and deoxygenated states of hemoglobin at physiologically regular concentrations are generally at least an order of magnitude higher than other chromophores like water or lipids. Thereby, blood vessels are the main source of contrast in OA images. At shorter wavelengths within the visible range hemoglobin absorption is even higher and can exceed that of other chromophores by more than two orders of magnitude.

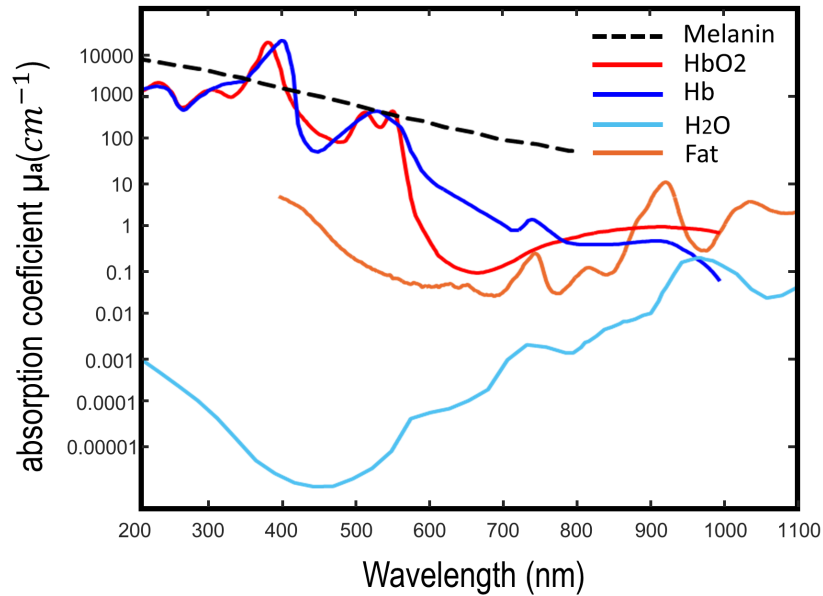


FIGURE 1.5: Optical absorption spectra of major endogenous chromophores at typical concentrations occurring in living mammalian tissues. Melanin spectrum (brown) is shown for typical concentrations in the skin; hemoglobin (red – oxygenated, blue – deoxygenated) for typical concentrations in whole blood (150g l^{-1} – continuous lines) and average soft tissues (15g l^{-1} – continuous lines); water (cyan) for a typical concentration of 80% by volume in soft tissues; lipids (yellow) for a concentration of 20% by volume. The first (NIR - I) and second (NIR - II) windows, where optical absorption is minimized, are indicated [133].©

Although melanin has a higher absorption coefficient than blood, it tends to be highly localized in the skin and other regions rather than being a constituent of most biological tissues. Light penetration is hindered by hemoglobin below 650 nm and by water absorption at wavelengths above 1300 nm, hence this spectral region constitutes the aforementioned NIR window. Optical scattering is generally described with the bulk scattering coefficient μ_s , which gives the probability of a scattering event per unit of length. In biological tissues, μ_s is approximately 100 cm^{-1} [54]. Average absorption coefficient μ_a values within biological tissues typically range between $0.1 - 0.5\text{ cm}^{-1}$ at 750 nm [55]. The relatively low optical absorption coefficient values in biological tissues relative to the scattering coefficient values indicate that scattering is the main cause of light attenuation. Furthermore, light diffusion induced by optical scattering prevents resolving deep-seated structures. Two main light propagation regimes are defined. The ballistic regime takes place at shallow depths below $\sim 1\text{ mm}$

where photons undergo few scattering events and preserve their directivity. The diffusive regime corresponds to deeper regions, where light is omnidirectional due to several scattering events. Classical optics can describe light transport for the ballistic regime, whereas for the diffusive regime the light dispersion can be modeled by the diffusion equation [56]:

$$\frac{1}{c} \frac{\partial \Phi(r, t)}{\partial t} - \nabla D(r) \nabla \Phi(r, t) + \mu_a(r) \Phi(r, t) = S(r, t) \quad (1.9)$$

where $S(r, t)$ is the source term, $\Phi(r, t)$ the fluence rate, c the speed of light [ms^{-1}] and $D(r) = 1/3(\mu_s' + \mu_a)$ the diffusion coefficient. $\mu_s' = (1 - g)\mu_s$ is the reduced scattering coefficient. For anisotropic scattering, g is the anisotropy factor which in biological tissue is in the range 0.8 – 1 [55]. For a uniform semi-infinite medium uniformly illuminated on the surface, the light fluence distribution is given by the 1D solution to the diffusion equation, Beer's law [56]

$$\phi(r) = \phi_0 \exp\left(-\sqrt{\frac{\mu_a}{D}} r\right) \quad (1.10)$$

where r is the distance from the surface. The light fluence decays exponentially from its initial value at the surface level. For biological tissues excited in the NIR window, the decay is approximately one order of magnitude per centimeter. Considering that the OA contrast mechanism is absorbance based, the strength of the signals is proportional to the light fluence. Light attenuation represents a major challenge for OA tomography as instrumentation needs a large dynamic range for a proper detection of shallow and deep structures [57].

Acoustic waves with frequencies above $> 20kHz$ are known as ultrasound. Acoustic waves propagate longitudinally through matter. The propagation speed $c_s [ms^{-1}]$ depends of the material density $\rho [gcm^{-3}]$ and compressibility $k [Pa^{-1}]$ [56]

$$c_s = \sqrt{\frac{1}{\rho k}} \quad (1.11)$$

Speed of sound values for biological tissues, 70-80% water content, are around the speed of sound for water 1500 m s^{-1} at 25°C . Similarly, speed of sound values for bone and air, respectively, are 3500 m s^{-1} and 343 m s^{-1} . An important parameter of an elastic medium for acoustic wave propagation is the acoustic impedance $Z[\text{kg m}^{-2} \text{ s}^{-1}]$ [56]

$$Z = c_s \rho \quad (1.12)$$

The acoustic impedance establishes the relationship between the pressure generated by the acoustic waves and the displacement velocity of the particles $u_d [\text{m s}^{-1}]$ [56]

$$p = Z u_d \quad (1.13)$$

The difference in acoustic impedance at the interface between two propagation media is associated to the reflection R and transmission T coefficients. For normal incidence upon the interface of an incident medium with impedance Z_1 and a transmission medium with impedance Z_2 [58]

$$R = \left(\frac{Z_2 - Z_1}{Z_2 + Z_1} \right)^2 \quad \text{and} \quad T = \frac{4Z_1 Z_2}{(Z_1 + Z_2)^2} \quad (1.14)$$

where R and T are the reflection and the transmission energy coefficients in percent respectively. The strong acoustic mismatch between tissue and air implies that ~99% of the energy is reflected in each interface and hence water or ultrasound gel is generally required as a coupling medium for the detection of OA signals. Acoustic waves also attenuate mainly due to friction losses while propagating through tissue and can be approximated following:

$$p(r) = p_0 e^{-\alpha(f)r} \quad (1.15)$$

where p_0 is the initial amplitude, r the propagation distance [cm] and $\alpha(f)$ the frequency-dependent attenuation coefficient [$dBcm^{-1}$] with a typical value of $0.5 dBMHz^{-1}cm^{-1}$. By attenuating more high frequencies, biological tissues act thus as a low-pass filter for the propagation of ultrasound waves.

1.8.2 The Optoacoustic Effect

OA imaging, also called photoacoustic imaging is a biomedical imaging and sensing modality based on laser-generated US waves within biological tissues. The OA effect describes the conversion of pulsed, or time-varying, electromagnetic radiation into acoustic waves by means of a local thermoelastic expansion of the region where light is absorbed. The absolute value of the thermoelastic pressure is proportional to the micro-temperature rise induced by a portion of the absorbed pulsed light. The temperature rise distribution $\Delta T(r)$, in the order of millikelvins, can be expressed as [59]

$$\Delta T(r) = \frac{\mu_a(r)\phi(r)}{\rho(r)C_v(r)} \quad (1.16)$$

where C_v [$J(KgK)^{-1}$] is the heat capacity at a constant volume. This formulation remains valid upon illumination conditions of heat confinement, which means insignificant heat diffusion during the laser pulse irradiation. To neglect heat transfer during the duration of the laser pulse, the pulse width has to be shorter than the so-called thermal relaxation time [56]

$$\tau_r = \frac{d_c^2}{D} \quad (1.17)$$

where D is the thermal diffusivity (m^2/s) and d_c is the characteristic dimension of the heated region, e.g. the dimension of the structure of interest or the decay constant of the optical energy deposition, whichever is smaller. OA irradiation conditions of stress confinement are typically met by laser pulse excitations in the nanosecond

range. Figure 1.6, depicts an example of OA signal generation by short-pulsed excitation of a spherical absorber. The spherical absorber is located at a distance z_s from the irradiated surface. Taking in consideration its diameter d , the irradiation will meet stress confinement conditions in the spherical absorber during laser energy deposition if the duration of the laser pulse τ_p is shorter than the time of stress relaxation time $\tau_r d/c_s$ of the absorber. Therefore, given a pulse width shorter than τ_r assures thermal confinement conditions, while a shorter pulse width than τ_s is required to fulfill stress confinement [57].

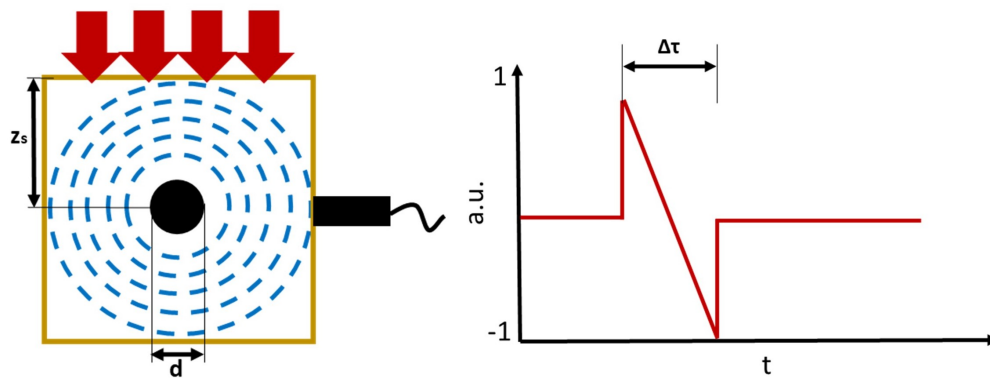


FIGURE 1.6: Schematics of optoacoustic signal generation by short-pulsed excitation of a spherical absorber.

The speed of sound of biological tissues is close to the speed of sound in water ~ 1500 m/s . Laser pulses with durations shorter than 100 ns should be used to generate stress confinement conditions for absorbers of 1 mm size [59]. Given a typical nanosecond laser pulse irradiation, the fractional volume expansion dV/V can be expressed as [56]

$$\frac{dV}{V} = -kp + \beta T \quad (1.18)$$

where $\beta[\%K^{-1}]$ denotes thermal expansivity or thermal expansion coefficient with values of $4 \cdot 10^{-4} K^{-1}$ for muscle tissue, p and T are the changes in pressure [Pa] and temperature [K] respectively. The isothermal compressibility k takes values $5 \cdot$

$10^{-10} Pa^{-1}$ for aqueous solutions such as biological tissues and can be expressed as [56]

$$k = \frac{C_p}{\rho c_s^2 C_v} \quad (1.19)$$

where ρ is mass density $1000 Kg m^{-3}$ for water and soft tissue, C_p and $C_v [J(gK)^{-1}]$ represent the specific heat capacities at constant pressure and volume respectively. Having a laser irradiation with a pulse width that meets heat and stress conditions, from Eq. 1.18 the fractional volume expansion can be neglected and the local pressure rise is derived as [56]

$$p_0 = \frac{\beta T}{k} \quad (1.20)$$

or [56]

$$p_0 = \frac{\beta}{k \rho C_v} \eta H \quad (1.21)$$

where $H [J/m^3]$ is the specific optical absorption and η is the percentage that is converted into heat. From here, the Grüneisen is further defined as:

$$\Gamma = \frac{\beta}{k \rho C_v} = \frac{\beta v_s^2}{C_p} \quad (1.22)$$

Then Eq. 1.21 becomes

$$p_0 = \Gamma \eta_{th} H = \Gamma \eta_{th} \mu_a \phi \quad (1.23)$$

Given that the confinement inequality holds true, thus the pulse durations are short and the fractional volume expansion can be neglected, the initial pressure-rise wave $P_0(r)$ equation may be directly described as a function of the local temperature increase

$$p_0(r) = \Gamma(r)\mu_a(r)\phi(r) = \Gamma(r)\Delta T(r)\rho C_v \quad (1.24)$$

where the Grüneisen coefficient $\Gamma(r)$ [dimensionless] represents the efficiency of thermo-acoustic excitation energy conversion. The Grüneisen coefficient is a function of the three tissue-specific physical parameters; thermal expansivity β , speed of sound c_s , and heat capacity at a constant pressure C_p .

The spatio-temporal propagation of the initial pressure distribution is governed by the inhomogeneous scalar wave equation with the second derivative of the local temperature as source function [62]

$$(\partial_t^2 - c^2\nabla^2)p = \frac{\beta}{k}\partial_t^2\Delta T \quad (1.25)$$

Assuming that Equation 1.17 is fulfilled, the source function can be rewritten in terms of a heating function defined as the thermal energy converted per unit volume and per unit time [56]

$$H = \mu_a\phi = \rho C_v\delta_t\Delta T \quad (1.26)$$

The OA wave equation is then rewritten as [56]

$$(\partial_t^2 - c^2\nabla^2)p = \Gamma\partial_t H \quad (1.27)$$

Equation 1.24 describes the generated pressure rise for small absorbers. The generated pressure-rise propagates in all directions from the absorber while the amplitude of the pressure wave generated by a spherical absorber decreases as $1/r$ with distance from the center from the absorber for $r > r_0$, see Figure 1.6.

For $r > r_0$ the spherical propagation can be considered as a planar wave front, therefore the pressure amplitude decreases as $1/r$ with the distance from the center of the absorber in the far zone.

The temporal profile of the pressure wave from the sphere has a bipolar N-shaped signal with positive and negative phases [60]. Given that the duration of an N-shaped temporal signal is $\Delta\tau$, the absorber dimension d can be then computed as $d = \Delta\tau \cdot c_s$.

1.8.3 Optoacoustic Signal Detection

Correct detection of the OA pressure waves prior to reconstruction is essential for effective OA imaging. Several types of US detection technologies have been employed, the most common being based on piezoelectric materials or optical methods. In this thesis we used piezoelectric detectors that hold 2 orders of magnitude greater sensitivity compared e.g. to interferometric approaches [63].

The piezoelectric material used for OA imaging ultrasonic detection need a high electromechanical coupling efficiency that leads to a higher sensitivity and an acoustical impedance closely matched to water and/or biological tissues. In biological imaging, piezoelectric materials are typically composites rods embedded in a polymer matrix that matches the acoustic impedance of the piezocomposite to the tissue [56].

The main component of an US transducer is the piezoelectric element. It is a resonating device which converts the pressure wave into an electrical signal. The resonance frequency of the piezoelectric element is given by the thickness of the material [64]

$$f_c = \frac{nc_L}{2L} \quad (1.28)$$

With the lowest resonant frequency being $n = 1$, c_L is the longitudinal acoustic wave velocity in the transducer material, L is the thickness of the piezoelectric material, and n is an odd integer. Therefore, resonances occur when L is equal to odd multiples of one half-wavelength and the thinner the piezoelectric material, the higher is the resonance frequency. The two surfaces of the piezoelectric material connected to electrodes to measure the generated voltage difference. The piezoelectric material is then covered with one or several matching layers that reduce losses due to

the impedance mismatch between the piezoelectric material and the imaging target, thus attaining higher sensitivity.

The backing material of an US transducer attenuates reverberations of the piezoelectric element, the higher attenuation the higher the bandwidth of the transducer. The closer it is matched to the impedance of the piezoelectric material, the better is the absorption of acoustic energy and thus the better the damping of the oscillations and will lead to a wider US transducer bandwidth. There will be a trade-off between sensitivity and bandwidth that has to be calibrated for the desired application, in order to be able to detect the weak OA signals while avoiding noise, i.e.: high Signal-to-noise ratio [64].

1.8.4 General Forward Solution and Reconstruction

Computational methods use mathematical techniques to reconstruct an image from the acquired OA signals. These mathematical methods are usually based on backprojecting formulas, also known as delay and sum approaches [65]. They can be resolved in spatiotemporal or Fourier domains, for more details the reader may refer to literature [56, 66, 67]. These formulas are exact under ideal conditions, such as when the wavefront is detected by an infinite number of omnidirectional infinitely broadband transducers distributed on an infinite detection surface. In general, the OA inversion represents the mathematical solution to recover the initial OA pressure distribution p_0 in Eq.1.23 from a finite number of time-resolved pressure measurements. It has been previously demonstrated that the OA inversion can be performed on any surface shape [68]. However analytical solutions were only found for planar, cylindrical and spherical geometries [66].

The backprojection algorithm is a time domain solution to the OA equation, see Eq.1.23, given the assumption of thermal and stress confinement. For a spherical or cylindrical detection geometry, the back-projection formula is expressed as [66]

$$p_0(r) = \int_{\Omega_0} b(r_0, \bar{t} = |r - r_0|) d\Omega_0 / \Omega_0 \quad (1.29)$$

where

$$b(r_0, \bar{t}) = 2p(r_0, \bar{t}) - 2\bar{t} \frac{\partial p(r_0, \bar{t})}{\partial \bar{t}} \quad (1.30)$$

is the backprojection term related to the measurement at position r_0 and

$$d\Omega_0 = \frac{dS_0}{|r - r_0|^2} \cdot \frac{n_0^s \cdot (r - r_0)}{|r - r_0|} \quad (1.31)$$

is the solid angle for a detection element dS_0 with respect to a reconstruction point P at \mathbf{r} , n_0^s a vector pointing outwards perpendicular to the detection surface S_0 . Ω_0 is the solid angle of the whole measurement surface being $\Omega_0 = 4\pi$ for spherical and cylindrical geometries and $\Omega_0 = 2\pi$ for planar geometries. The term $d\Omega_0/\Omega_0$ is a factor weighting the contribution to the reconstruction from the detection element dS_0 .

The linearity of Eq.1.29 simplified the computational implementation of OA image reconstruction, enabling real-time imaging even with a high number of detectors allowed by GPU parallel computing. The analytical inversion that the back-projection approach yields non ideal results in real setups since full geometries, i.e.: full spherical surface of detectors, are typically not available. Therefore, the analytical inversion yields in practice reconstructions with presence of arc artefacts due to the nature of the limited view detector shape [67].

Chapter II

Methods and Contributions

Chapter 2

Methods and Contributions

OA has been demonstrated to be a promising imaging and sensing modality for biomedical applications [69, 70] due to its unique capabilities that bring a new range of tools to the existing imaging technologies. OA is particularly suitable for applications where hemoglobin-based optical contrast is a means to monitor the clinical treatment. Since hemoglobin is one of the strongest absorbers and is present in most living organs, OA provides a means to closely image living organisms together with a wide range of bio-markers and medical procedures. As shown in Figure 1.6, the amplitude of the detected OA pressure wave is proportional to the optical absorption of the illuminated tissue. This principle makes the technique very sensitive to variations in optical absorption and capable of resolving different absorbers with high spatial accuracy. If pressure waves are collected from a multitude of positions, with sufficient observation angle, an image can be reconstructed that shows an absorption map of the irradiated tissue area. Likewise, if we apply several illumination wavelengths, multiple absorbers can be clearly identified based on their characteristic wavelength-dependent absorption profiles by means of spectral unmixing algorithms [71, 72]. On the other hand, OA presents important advantages to monitor ablation procedures as detailed below.

2.1 Noncontact Monitoring of Incision Depth in Laser Surgery with Air-coupled Ultrasound Transducers

When a laser beam is sufficiently focused at a high energy level, its electric field can accelerate a free electron, not bound to a molecule, enough to ionize a molecule with which it collides without itself becoming bound. This results in a chain reaction that leads to plasma formation and shockwave emission. This chain reaction will move on so far as the intensity of the electric field is high enough to have a greater ionization rate than the rate at which electrons become re-bound to ions [13].

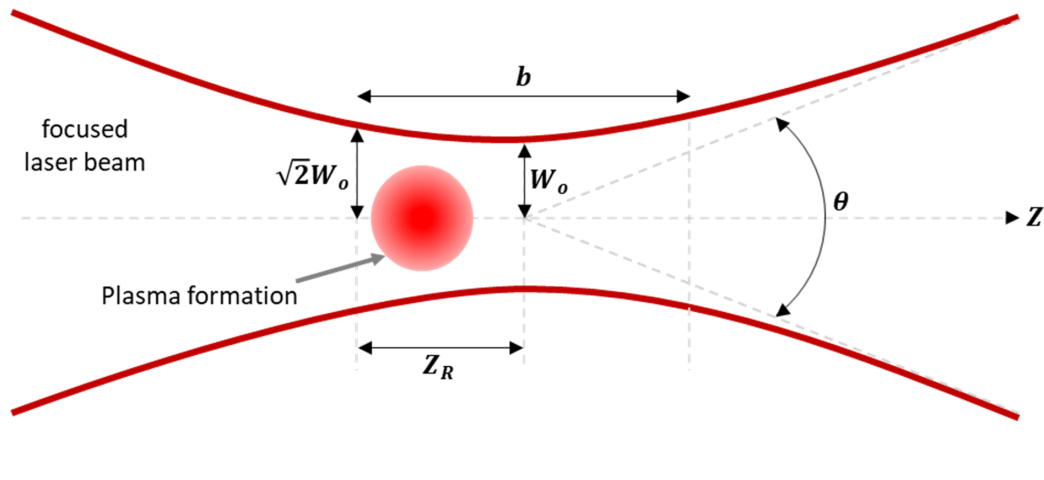


FIGURE 2.1: Diagram of plasma formation at the focal spot of a focused laser pulse.

Figure 2.1 presents the schematics of the focal volume where plasma is generated through laser-induced dielectric breakdown. When an ultrashort pulsed laser beam is focused, the smallest beam radius is found at the focal spot in the depth of focus b . Another name for the focal spot is the beam waist that is equal to the diffraction limited focal spot size, W , for a beam of wavelength λ and can be represented by [73]

$$W = \frac{4M^2\lambda f}{\pi D} \quad (2.1)$$

where, $W = 2W_0$, is the beam focal spot diameter, M^2 is the beam quality factor, f is the focal length, and D is the pre-focus beam diameter. Once the beam passes the focal zone, the beam diameter expands and can be described as [73]

$$W_z = W_0 \sqrt{1 + \left(\frac{z}{z_0}\right)^2} \quad (2.2)$$

where z is the distance from the beam waist and z_0 is the Rayleigh length [74]. When the peak power density of the incident pulsed laser excitation exceeds the ionization threshold potential of the electric field, plasma is generated around the focal spot [75, 76]. The plasma is initially generated near the beam waist and eventually absorbs energy and expands towards the incident laser irradiation. The probability of plasma generation is dependent on the peak power density, at near-threshold power densities this probability is 50%. Material removal on a tissue sample through vaporization and ejected tissue is achieved when the plasma is brought into physical contact with the biological sample.

Tissue ablation using pulsed lasers, is being researched because this illumination form typically produces surgical cuts with less damage than CW lasers [77]. This effect takes place in plasma formation, as the translational kinetic energy of free electrons is quantitatively much higher than the energy of bound electrons known as energy levels, then the plasma can absorb all incoming radiation and shockwaves, this effect is known as plasma shielding [13]. The focus on the use of pulsed lasers arises thus for the purpose of avoiding thermal side effects and treatment of pigmented and vascular lesions by selective photothermolysis. The natural drift from CW laser treatments to pulsed illumination is due to the findings of frequent tissue coagulation and eventual carbonization and charring effects derived from continuous wave laser vaporization [78]. Laser surgery ablation is generally described as a dynamic explosive process, further experimentation with pulsed lasers has led to the development over the last decade of different approaches of modeling the ablation processes, which are of useful value for understanding separately various ablation parameters such as time delay between laser irradiation and tissue removal, velocity of ejected material, tissue removal efficiency or threshold fluence to trigger ablation.

Pulsed laser ablation has been widely applied for laser cutting surgical applications,

ranging from ophthalmology to dermatology and oncology, due to its intrinsic advantages compared to classical scalpel based surgical protocols [79]. Besides an improvement in incision depth accuracy, the main advantage of laser based surgical methods resides in the hemostatic properties of laser light, stagnating the blood for a better post-treatment sealing and thus minimal swelling and bleeding. Besides tissue removal in the focus of the laser beam, the absorption of optical energy also causes heating of surrounding biological tissue and consequently sealing neighboring blood vessels during the surgery [79]. As follows, excessive bleeding complications can be avoided, simplifying the overall complexity of the treatment protocol and reduced operative and post-operative traumatization. Absorption of optical energy and ejection of material also leads to the generation of high intensity (shock) acoustic waves, which can be considered a particular type of OA signals.

The feedback sensing methodology studied in this thesis, see Figure 2.2, tests the feasibility of monitoring the incision depth in laser cutting by measuring the time of flight of the generated pressure waves with air-coupled transducers.

The main limitation associated with coupling of ultrasound through air when using standard (immersion) ultrasound transducers is the impedance mismatch between air and biological tissues with acoustic properties similar to water. Besides, the high attenuation of ultrasonic waves in air of 1.6 dB/cm for 1 MHz also represents an added difficulty for detecting OA signals without direct contact.

It has been shown that air-coupled transducers (ACT) have a sensitivity enhancement of 15 dB by means of composite layers matching the acoustic impedance of the transducer to the air [131]. Therefore, air-coupled transducers are suitable for non-contact shock wave detection.

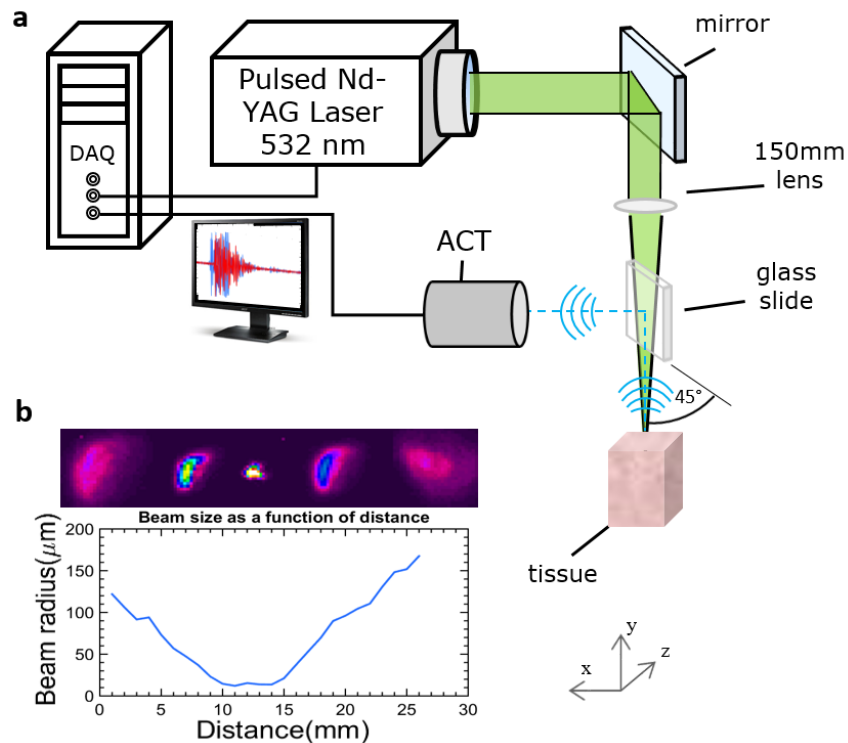


FIGURE 2.2: (a) Layout of the experimental setup. ACT, air-coupled transducer; DAQ, data acquisition. The glass slide with 1.1 mm thickness is positioned at 45° relative to the propagation direction of the shockwaves so that the acoustic waves are reflected at 90° into the ACT. (b) Ablation beam characterization in the vicinity of the focal region. Typical beam shapes are shown in the inset. The effective depth of the focus is approximately 5 mm.

Shock waves emitted from the ablation spot were detected with a self-developed unfocused air-coupled piezoelectric transducer with a central frequency of 0.8 MHz and -6 dB bandwidth of 0.4 MHz, positioned at an acoustic travel distance of 50 mm from the tissue surface using a glass slide at 45° reflecting the acoustic waves at 90° to the transducer, see Figure 2.2

The time of arrival of the measured shock waves was estimated as the instant for which the pressure signal level exceeds a defined threshold, which was set to 16% of the maximum value for the entire signal sequence. It was further assumed that the ablation spot is always located at the bottom of the cut so that it deepens as the incision progresses, thus increasing the delay in the time of arrival of the waves at the transducer surface. The time of flight difference (TOFD) of the generated shock

waves due to propagation inside an open cut is then estimated as the difference in the time of arrival T_i for each detected shock wave with respect to an average time of arrival T_0 for the signals generated by the first 20 laser pulses.

Assuming the speed of sound within the incision c_i is known, the incision depth d can be estimated according to

$$d = c_i \cdot TOFD \quad (2.3)$$

In this study, we used 40 liver cheese (German: leberkäse) samples, 30 samples of chicken breast, and 20 samples of chicken bone. The incision depths ranged from 1 to 4 mm for soft tissue samples, leberkäse and chicken breast, and from 1 to 8 mm for the osseous tissues. The thickness of the samples was 10 mm, see Figure 2.3.

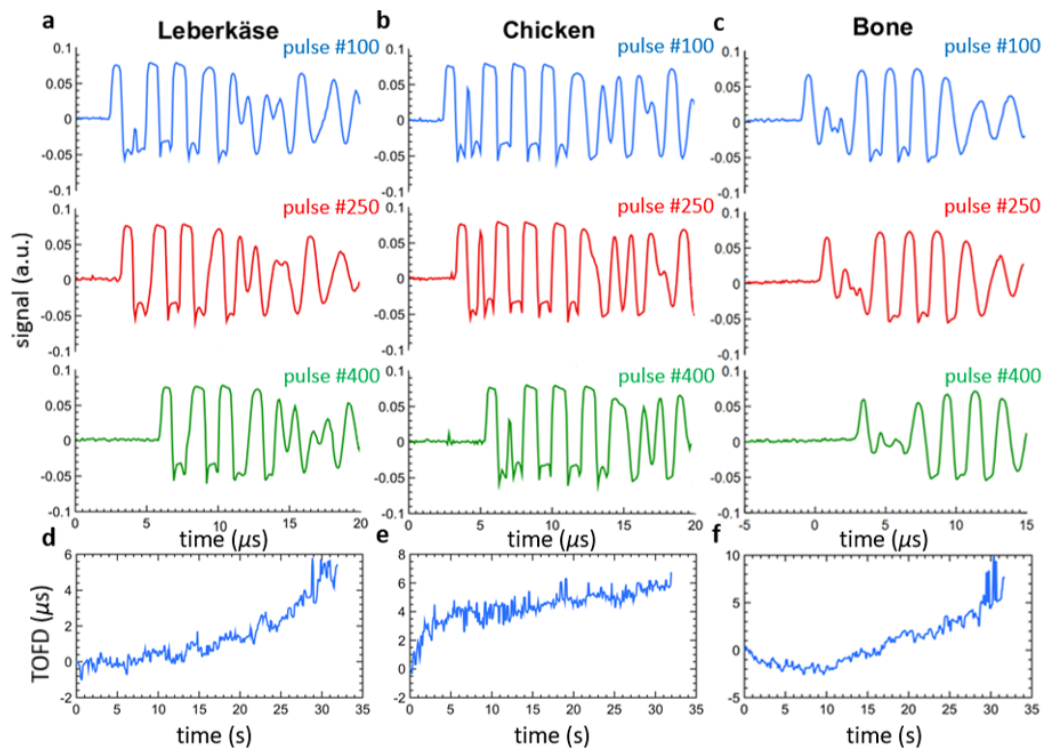


FIGURE 2.3: Illustration of the method used to estimate the incision depth within the incision profile for different tissue types. Examples of the recorded signals for (a) liver cheese, (b) chicken, and (c) bone. Each color corresponds to three different instants, namely, pulse #100, #250 and #400 after the ablation starts. Evolution of the corresponding TOFD is shown in (d)-(f).

Figures 2.3a-2.3c show examples of the time-resolved signals recorded by the air-coupled transducer for the three different tissue types. The recorded waveforms are increasingly delayed as the incision progresses, indicating deepening of the lesion. Figures 2.3d-2.3f show three examples of the measured TOFD of the shock waves for the entire pulse sequence.

One also may note that the time of arrival slightly decreases in the starting phase of the bone tissue ablations, see a representative example in Figure 2.3f, which may be attributed to accumulation of thermoelastic effects at the tissue surface before the actual tissue vaporization takes place. In general, the time of arrival exhibits unsteady behavior in the starting phase of the ablation for all tissue samples. Most time-resolved signals are also characterized by lengthy oscillations, presumably due to residual light absorption in previously generated tissue debris within the crater. Some abrupt variations in the time of arrival also can be attributed to random ablation events occurring in particles suspended in air before the light pulses reach the tissue. The values of the speed of sound inside the incision profile were estimated by considering the final incision depth d_f measured in post-ablated tissue slices and the average time of flight difference recorded for the last 20 laser pulses $TOFD_f$ via

$$c_i = d_f / TOFD_f \quad (2.4)$$

The calculated values of c_i are shown in Figure 2.4 as a function of the measured final incision depth. For soft tissue samples, the average estimated c_i increases versus incision depth, see Figures 2.4a and 2.4b. Specifically, c_i reaches average values of 750 and 570 m/s for 3-4 mm cuts in the leberkäse and chicken breast specimens, respectively.

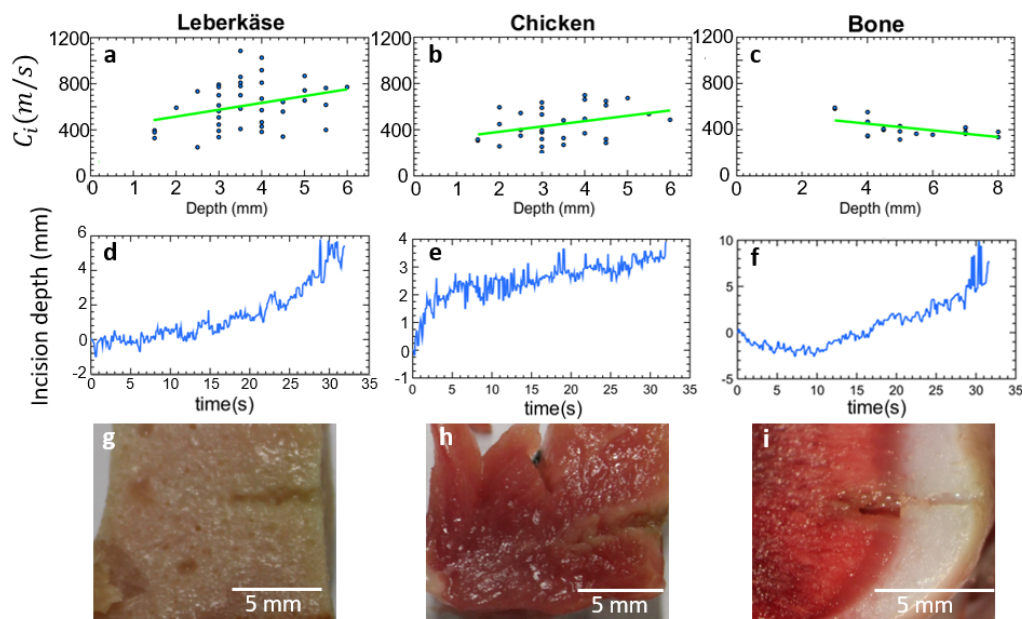


FIGURE 2.4: (a)-(c) Distribution of the estimated speed of sound within the incision based on measurements performed on sliced specimen. Green lines correspond to the linear fit through the scattered data. Examples of real-time incision depth estimations for the tissue samples in Figure 2.3 are presented in (d)-(f). Actual photographs of the sliced samples are shown in (g)-(i), respectively.

For shallow incisions, the average c_i values remained close to the speed of sound in air, 343 m/s for dry air at 20 °C. This may indicate that deeper cuts in soft tissue samples have been filled up with material expelled by previous ablation events, so that the shock waves propagate through a mixed air-tissue medium. Conversely, the average of c_i better matched the speed of sound in air for bone samples, even for considerably deeper cuts, see Figure 2.4c. This implies that the extracted volume is mainly filled with air during the ablation of bones. See the actual incision profiles corresponding to the measurements presented in Figures 2.4g-2.4i.

The method detailed in this section demonstrates the basic feasibility of attaining real-time feedback on the laser-induced incision depth by means of noncontact detection of the generated shock waves with ACTs. Several clinical applications will benefit from the presented approach. In melanin pigmentation treatments, maxillo-facial surgery, and precancerous lesion or benign tumor removal, the performance

of laser-based surgery procedures is often hindered by the lack of online depth monitoring. According to the presented results in this thesis, the method is anticipated to provide accurate estimates on the incision depth in bones, making it ideally suited for accurate monitoring of lesion depth in laser osteotomy. The advances derived from the noncontact nature of this real-time depth monitoring approach are expected to advance the general applicability of laser-based surgeries.

2.2 Integrated Catheter for Simultaneous Radio-frequency Ablation and Optoacoustic Monitoring of Lesion Progression

Radiofrequency catheter ablation is a commonly used treatment for many cardiac arrhythmias, in particular arrhythmias that have shown to be resistant to drug therapy. The RF catheter ablation procedure is guided by electrophysiological and anatomic mapping as well as careful RF power titration during the ablation [126].

Currently, the success of ablation treatments depends on the skill of the medical practitioner in assessing lesion formation, leading to an undesirable amount of inefficiencies, undesired collateral damage and failed treatments. An effective lesion monitoring technique would likely improve the learning curve for clinicians and would strongly increase the success rate of ablation treatments.

Ablation lesion formation has been formerly monitored via alternative imaging modalities. The development of MRI technologies led to MRI-based techniques to real-time visualizations of lesion formation in porcine hearts [80]. However the current spatial and temporal resolution of MRI represents a limitation from becoming a suitable imaging modality in commonplace medical care. US sensing catheters have likewise been developed which resulted in unsuitable imaging contrast and clear boundary distinction between denaturalized and living tissue [81]. More recent US-based methods such as acoustic radiation force impulse (ARFI) imaging [82, 83] and thermal strain imaging [84, 85] strive to improve the contrast between necrotic and

non-damaged cells during ablation lesion formation by monitoring changes in tissue elasticity and temperature dependent speed of sound variations, respectively. The ARFI technique in its current development stage is highly sensitive to motion artefacts and has low temporal resolution, while thermal strain imaging is only capable of providing indirect information on lesion size by interpretation after a measurement of an apparent temperature rise.

Contrast between ablated and non-ablated tissue can also be observed with optical imaging techniques. Optical coherence tomography [86, 87] was shown to be capable of real-time monitoring of ablation lesion formation with high spatial resolution. However the penetration depth of this modality can only reach ~ 1 mm and hence can only be employed for monitoring shallow tissue effects under hyperthermic conditions during ablative interventions.

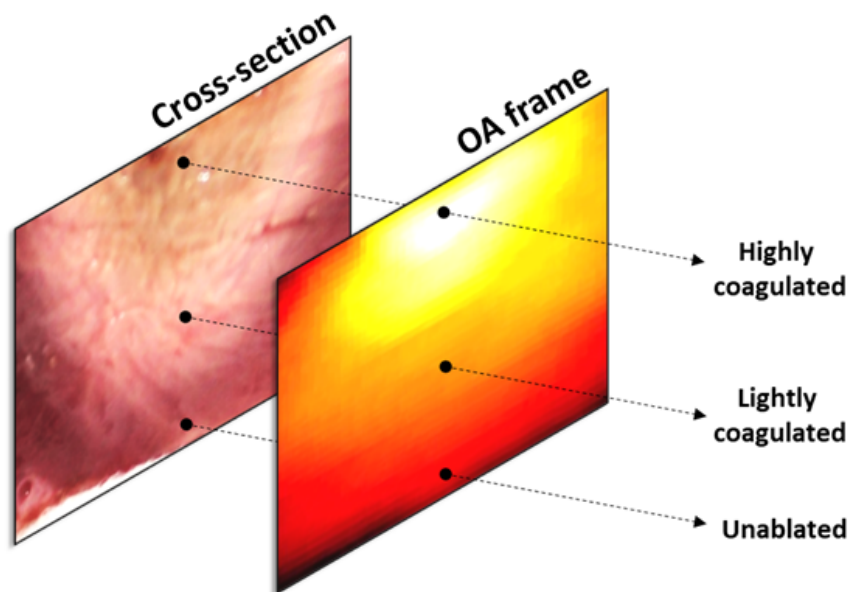


FIGURE 2.5: Cross-sectional photograph taken after completion of ablation and post-ablation OA image corrected for fluence decay. The three differential tissue stages of coagulation can be identified: Highly coagulated, mildly coagulation and non-coagulated tissue.

Previous works to this thesis have shown that three-dimensional OA imaging can

provide effective diagnosis and real-time feedback for monitoring ablation necrosis [88]. Pulse repetition rates of 10 Hz have shown to be effective temporal resolution for controlling coagulation formation through changes in optical properties during current ablation treatments. In the same manner, OA ablation monitoring can achieve faster feedback by using higher frame-rate pulsations. OA delivers a good absorption-based contrast at the boundary of the highly coagulated tissue, providing new advantageous means to monitor ablation-driven coagulation over previously suggested ultrasound-based techniques [81–83]. At the same time, OA can retrieve coagulation changes from significantly deeper lesions compared to pure optical methods.

OA imaging benefits from both aspects of optics and ultrasound, intrinsically having the advantages of US profound detection and optical high contrast. The good ablation lesion contrast that OA provides, originates in the fact that necrotic and un-ablated tissue show to have distinct OA intensity [89], see Figure 2.5. The different OA spectrum found between coagulated and non-coagulated biological tissue is mostly attributed to the difference in the extinction spectrum of hemoglobin Hb. It was previously reported that the extinction coefficient of non-ablated tissue has a peak in the infrared range of 740-800 nm, which is not present in the coagulated tissue [90].

In this study we present a combined RF ablation and OA imaging catheter. Our unipolar ablation catheter design combines the capability of RF ablation and light delivery for OA imaging in a single compact and flexible unit. The catheter was used to generate ablation in ex-vivo porcine tissue while simultaneously monitoring the lesion formation using OA tomography with the necessary illumination delivered through the RF catheter itself, see Figure 2.6.

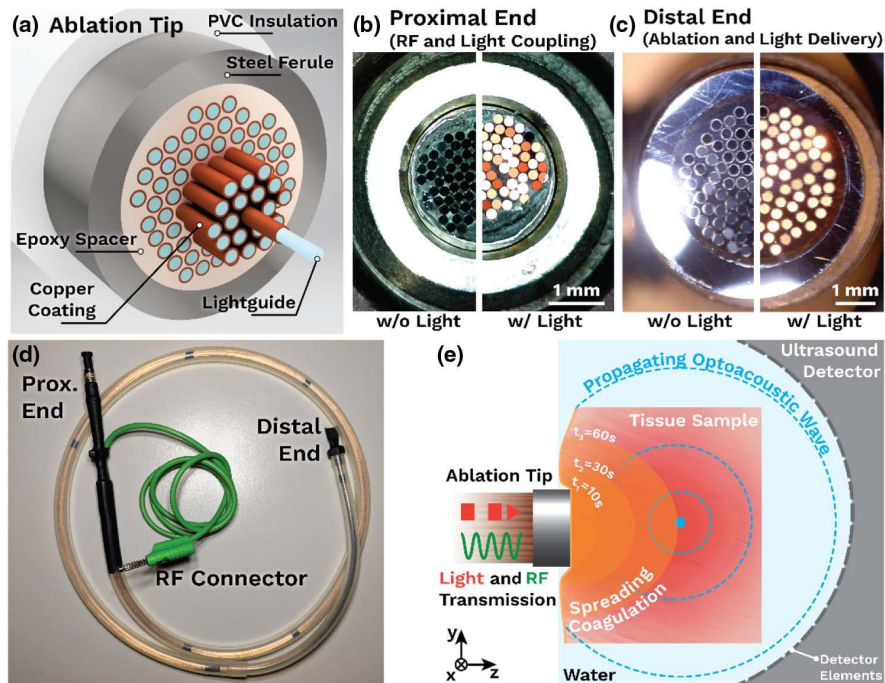


FIGURE 2.6: Design and application of the combined RF and OA catheter. (a) Catheter ablation tip, comprising copper-coated light guides embedded in a steel ferule using high-temperature epoxy. (b) Proximal end facet of the catheter, optimized for high light coupling efficiency. (c) Distal end facet of the catheter, delivering both RF current and pulsed-light illumination. (d) Fully assembled bundle. (e) Layout of the combined RF-OA monitoring experiment.

Light and electrical current are coupled into the distal end of the catheter and are delivered to the tissue at the distal end, where the electrical current causes coagulation and desiccation while the light is locally absorbed and generate OA signals. This is achieved by combining ~ 100 copper-coated multimode light-guides into a single bundle, see Figure 2.6a-c.

The individual light-guides are optical fibers with a silica core and a fluorine-doped glass cladding, creating a classical step index multimode fiber that allows the propagation of visible and near-infrared diffuse illumination over large distances with negligible losses. The fibers have a core diameter of $200\ \mu\text{m}$, a cladding diameter of $220\ \mu\text{m}$ and a numerical aperture of $\text{NA} = 0.2$. The fibers were coated with a $20\ \mu\text{m}$ thin copper film during manufacturing in order to create a fiber conducting both light and current, see Figure 2.6d. The high core-to-cladding ratio of the fibers makes coupling

light into the fiber bundle very efficient, with a theoretical overall coupling efficiency of better than 30%.

RF lesions were created in four separate ex-vivo porcine tissue samples in this study. The samples were immersed in phosphate-buffered saline during the ablation and the ground-electrode of size 20 cm² was positioned on side opposite to the ablation tip with respect to the tissue. The catheter was connected to a RF generator. The catheter acted delivering 20 kHz ablation current with a duty-cycle of 3%, delivering 1 W for 10 s, 20 s, 40 s and 60 s, see Figure 2.7. Synchronous to the laser trigger, the sound amplifier was set to 600 cycles of RF energy at 20KHz after 100 μ s delay at the laser pulse repetition rate, see Figure 2.6e.

Pang et al. visualized lesions showing good contrast at the boundary of the highly-coagulated tissue, and further concluded, that the optimal illumination wavelength in the infrared spectrum is 780 nm for ventricular myocardial tissue, maximizing the contrast at the necrotic-healthy tissue boundary [88]. The distal end of the catheter then delivered short-pulsed 8 ns laser light with a per pulse energy of 6 mJ at a repetition rate of 10 Hz and at a wavelength of 780 nm, while monitoring of RF lesion formation was volumetrically carried out with a three-dimensional OA system consisting of a 512-element spherical transducer array, see Figure 2.7.

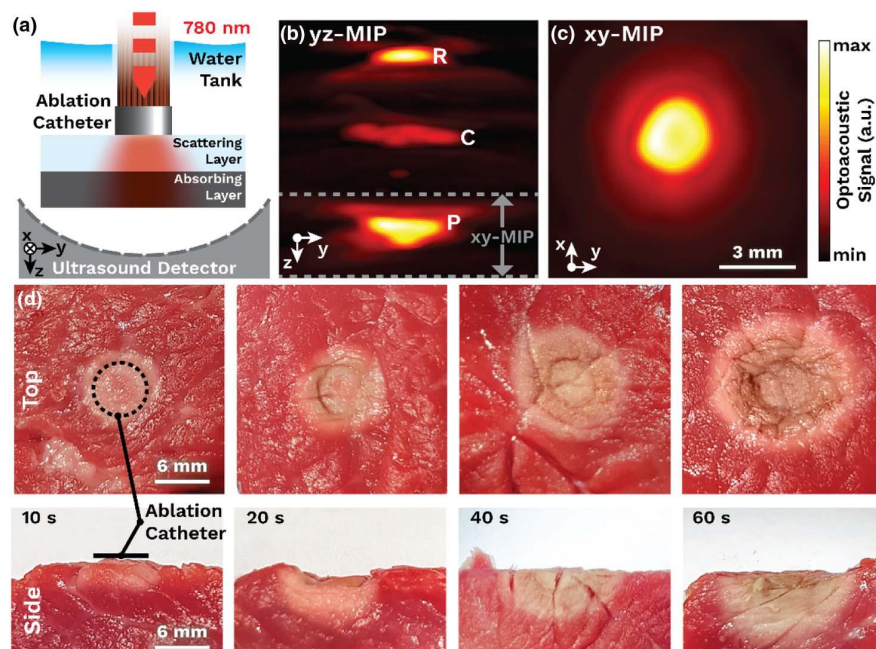


FIGURE 2.7: Characterization of the RF-OA catheter. (a) Experimental arrangement for OA imaging. (b) Reconstructed volumetric OA images of the phantom containing signals generated by the absorbing layer (P) and the catheter tip (C) as well as the signal reflected by the catheter tip (R). (b) Maximal intensity projection (MIP) along the x direction. (c) Corresponding MIP image made along the depth direction. (d) Top- and side-view photographs of lesions generated.

On average, 9 W of electric power were delivered for 10 s, 20 s, 40 s, and 60 s into the porcine tissue samples. Photographs of the generated lesions are shown in Figure 2.7d. Longer ablation durations generated deeper lesions, reaching a maximal depth of ~ 1 cm after 60 s. The uniform lesion shape indicates a homogenous current distribution around the copper-coated light guides.

Figure 2.8 showcases the OA real-time monitoring of the lesion before, during and after RF ablation in *ex-vivo* porcine tissue, see Figures 2.8a-c respectively. Figure 2.8a shows a maximum-amplitude projection of the recorded volumetric OA image and displays the homogenous and undamaged structure of the porcine tissue prior to the RF ablation. It is evident that OA signals are generated throughout the whole tissue, which indicates that the amount of light transmitted through the RF-OA catheter is sufficient to image structures at several centimeters of depth. Hence, the catheter

would easily be able to monitor ablation in several millimeter-thick human myocardial tissue. This was a limitation in previous OA monitoring of ablation formation, where light and ablation energy delivery was separated [126], which required light propagation through several centimeters of highly absorbing tissue. The developed catheter circumvents this by delivering the OA illumination directly to the area at which the ablation is applied.

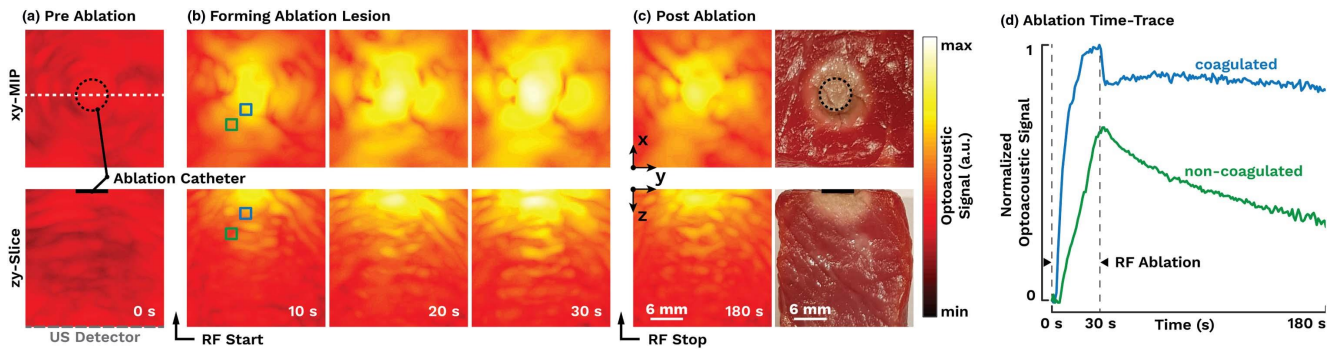


FIGURE 2.8: Real-time OA monitoring of RF ablation in ex-vivo porcine heart tissue. (a) OA images acquired from unablated tissue. (b) Noninvasive OA imaging of the lesion formation in 3D. (c) OA image acquired after the cooldown phase along with the photograph of coagulated area from a sliced specimen. Images on the top are top-view MIPs while the bottom row shows a single (z-y) slice through the center of the reconstructed OA volumes, as indicated by the white-dashed line in (a). (d) Time evolution of the OA signal during and after RF ablation in the locations indicated in panel (b).

Figure 2.8b shows maximum amplitude projections at three discrete time points during the ablation where a strong increase in the OA signal amplitude can be observed. The OA signal increase is due to the lesion specific contrast at 780 nm as well as due to the strong temperature dependence of the Grüneisen parameter, which describes the relation between absorbed light energy and generated OA signal.

OA images and gross pathology of the specimen are compared in Figure 2.8c. Both the OA signals and the pathology confirm a uniform coagulum without charring. The appearance of the lesion in the OA images agrees well with the size and shape of the lesion morphology found in the gross pathologies. The cooled-down tissue, see Figure 2.8c at $t = 180$ s shows a lower OA signal amplitude compared to the OA signals at the end of the RF ablation $t = 30$ s, Figure 2.8b. This is attributed to the temperature dependence of the OA signals. The OA signal levels at $t = 180$ s remain higher than in

the preablated sample due to incomplete cooldown and residual thermal diffusion effects in the rest of the specimen. The separation of the OA signal contribution due to temperature and those due to coagulation are to be investigated further. Using a multi-spectral approach, which is readily available with the given system [126] it should be possible to separate the respective contributions. It would then be possible to acquire both high-resolution images of the actual lesion as well as an accurate temperature map in and around the ablation tip. Currently this cannot be achieved with existing imaging technologies and would be of tremendous advantage for clinical RF catheter ablation.

Here we presented a novel unipolar catheter combining radiofrequency ablation and optoacoustic imaging in a single flexible and adaptable design. The catheter is comprised of copper-coated multimode light-guides which are combined into a bundle and whose proximal and distal ends are polished to allow for efficient light coupling into both the catheter and the tissue. The RF current is conducted through the copper coating of the fibers and no additional wiring is required to form a fully functional catheter capable of delivering both RF ablation current as well as diffuse illumination for volumetric optoacoustic imaging. This catheter design enables precise spatio-temporal monitoring of lesion morphology during RF ablation. Imaging was performed using a single 780 nm wavelength, making a potential combination of this design with existing catheter and monitoring modalities simple and cost-effective. Using multispectral optoacoustic tomography with the same catheter design could enable volumetric imaging of the temperature distribution in the forming lesion as well as the extraction functional tissue parameters in *in-vivo* models.

2.3 Volumetric Optoacoustic Temperature Mapping in Photothermal Therapy

OA imaging represents an advantageous technique for lesion monitoring. As discussed above, it is capable of visualizing the highly coagulated region formed during

ablative treatments. This part of the lesion is characterized by strongly damaged tissue, typically showing brown stains and presenting shrinkage due to loss of water in the coagulation process. However, this tissue coagulation level is present only in a minority of lesions while in the majority of cases, necrosis is reached in a mild-coagulation state of the organic tissue [88].

Temperature values reached within the tissue play a crucial role in the outcome of ablation procedures while the temperature field distribution defines the volume of coagulation [33] and, the amount of tissue undergoing thermal damage. Therefore, it turns critical to find a method that is capable of detecting the boundary of the mildly coagulated region monitoring temperature and thus providing a useful feedback of pivotal importance for effective therapy, aimed at completely removing the neoplastic volume without collateral thermal damage to the surrounding healthy tissue. Temperature monitoring is thus considered essential in all hyperthermic treatments described above, namely LITT, RFA, and HIFU. The rise of all hyperthermic therapy methodologies has led to the investigation of best approaches to succeed in accurate tracking of temperature.

Coagulation induces changes in the tissue sample optical properties, resulting in changes in spatial and temporal pressure profiles. Therefore, by recording with a subsequent analysis of the temporal pressure profiles, it allows monitoring the dimensions of coagulated zone with high resolution and contrast.

There were few initial investigations about the temperature effect on the OA signal pressure amplitude. Larina et. al. presented in 2005 the OA pressure amplitude of an aqueous solution versus temperature, see Figure 2.9 [119]. The theoretical curve in Figure 2.9 was drawn retrieving empirical data on the thermal expansion coefficient, speed of sound and heat capacity at a constant pressure from Weast (1974) and Kikoin (1976).

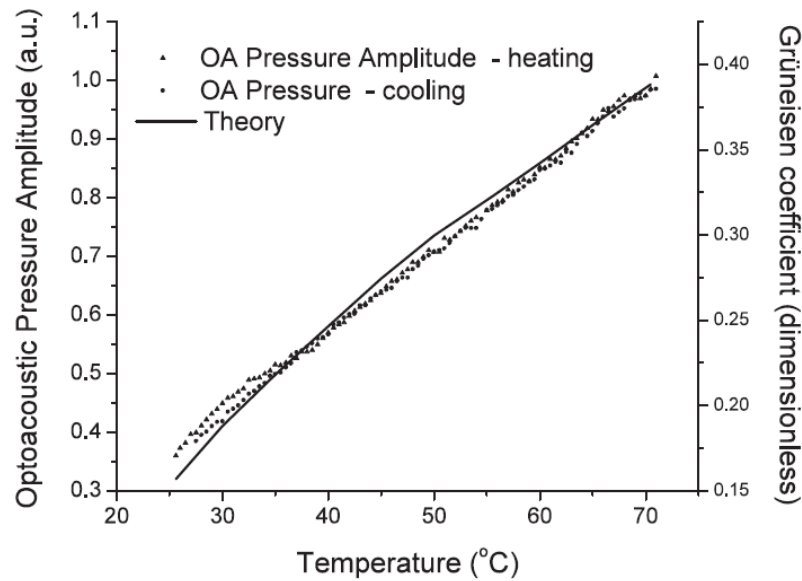


FIGURE 2.9: Theoretically calculated water Grüneisen coefficient and OA pressure amplitude induced in aqueous solution as a function of temperature [119].

The linear dependence of the OA pressure amplitude on temperature can be used for temperature mapping. Temperature changes within biological samples can be computed by detecting the pressure wave and comparing it with the pressure wave saved before the therapeutic heat source had been applied. The reference temperature T_{ref} must be known in advance, meaning there will be some temperature detection element that reads us the initial temperature value. The subsequent OA pressure amplitude measurement will allow us to calculate the increment in temperature that will be converted into absolute temperature by adding T_{ref} .

This methodology leads to the possibility of measuring temperature rises in tissues by detecting the pressure wave amplitude with an accuracy better than 1 °C at depths of up to 3 cm from the transducer surface. The accuracy of an OA measurement is at the same time limited to the stability of the light source, however current laser systems with stabilized pulse energy available in the market attain 1% stability [119].

The temperature computation methodology developed in this thesis, specifically for laser ablation, see Figure 2.10, is based on the physical principle of the thermoelastic conversion efficiency of the OA signals being dependent on the local temperature

at the instant of emission of the laser pulse. When the OA signals are excited with a short-duration laser pulse, the so-called stress-confinement conditions, described in Eq. 1.17, can be assumed for the initial OA signal pressure distribution p_0 in the medium. In this case, the latter is given via Eq. 1.24.

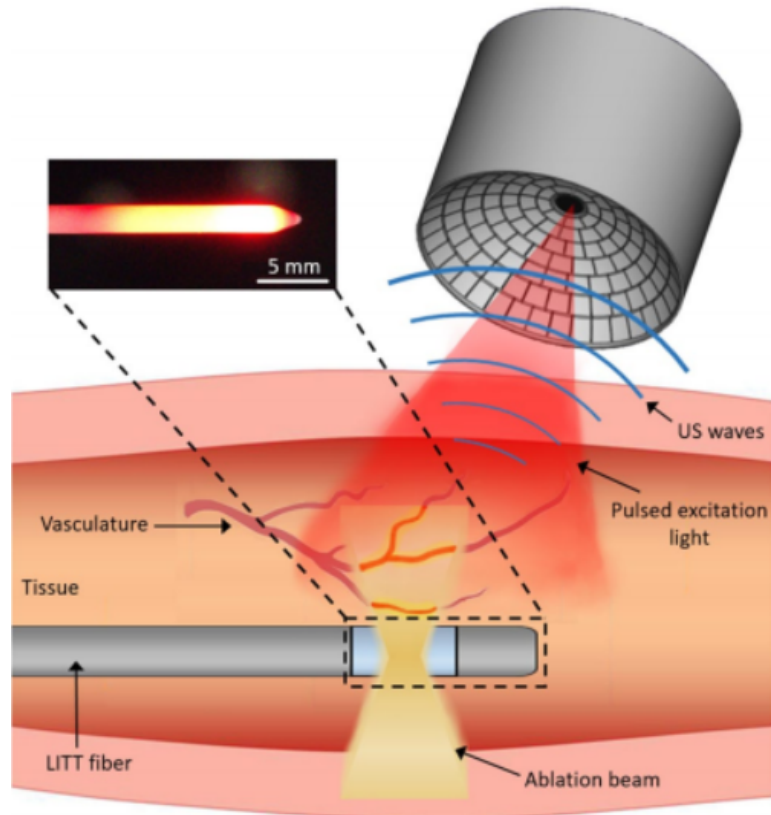


FIGURE 2.10: Volumetric optoacoustic monitoring during photothermal therapy [33].

The temperature dependence of the generated OA signals mainly is attributed to variations in the Grüneisen parameter, whose dependence on temperature in water-like aqueous solutions can be approximated by [56]

$$\Gamma(T) = 0.0043 + 0.0053 \cdot T \quad (2.5)$$

where T is expressed in $^{\circ}\text{C}$. Eq. 2.5 describes the temperature dependence of the Grüneisen parameter for water and diluted aqueous solutions, which was verified

with empirical measurements across a wide range of temperatures [120]. The relative change of the OA signal as a function of the temperature increase ΔT can be then expressed as [33]

$$\frac{\Delta p_0}{p_{0,0}} = \frac{0.0053\Delta T}{0.0043 + 0.0053T_0} \quad (2.6)$$

being $p_{0,0}$ and T_0 the initial baseline OA signal and the initial temperature before the heat source is applied, respectively. According to Eq. 2.6, the amplitude of the OA signals is expected to increase by approximately 2.7% per degree for typical temperature values of 36 °C in living organisms. A coefficient F was further defined for simplicity as the ratio between the relative increment of the OA signal and the relative increment of temperature

$$F = \frac{T_0}{p_{0,0}\Delta T} \Delta p_0 \quad (2.7)$$

Considering Eq. 2.7 the theoretical value of $F(F_{th})$ can be expressed as a function of the initial temperature T_0 via

$$F = \left(\frac{0.8113}{T_0} + 1 \right)^{-1} \quad (2.8)$$

The temperature increment can then be estimated from the relative OA signal increase as

$$\Delta T = \frac{T_0}{p_{0,0}F_{th}} \Delta p_0 \quad (2.9)$$

It should be noted that, unlike for inorganic liquids, protein denaturation and coagulation processes are known to take place in soft biological tissues for temperatures exceeding 50 °C, introducing significant additional complexity due to non-linear alterations of the Grüneisen parameter [119] as well as alterations in the optical absorption and scattering coefficient of the ablated tissues [121]. Accuracy of the above

temperature estimation approach is therefore expected to be limited to temperatures range lying below the coagulation threshold.

Additionally we further tested the quantitative performance of the method described in Eq.2.9 in tissue-mimicking phantoms. The phantom consisted of three tubings with 1 mm diameter and 10 mm length embedded in a ~8 mm thick layer of chicken breast. The tubings were filled with murine blood and sealed with glue. Three implantable thermocouples were inserted into the tubings to provide real-time temperature values. Likewise, for each tubing, the temperature was estimated from the OA signal in a region of interest (ROI) corresponding to the exactly known location of each thermocouple.

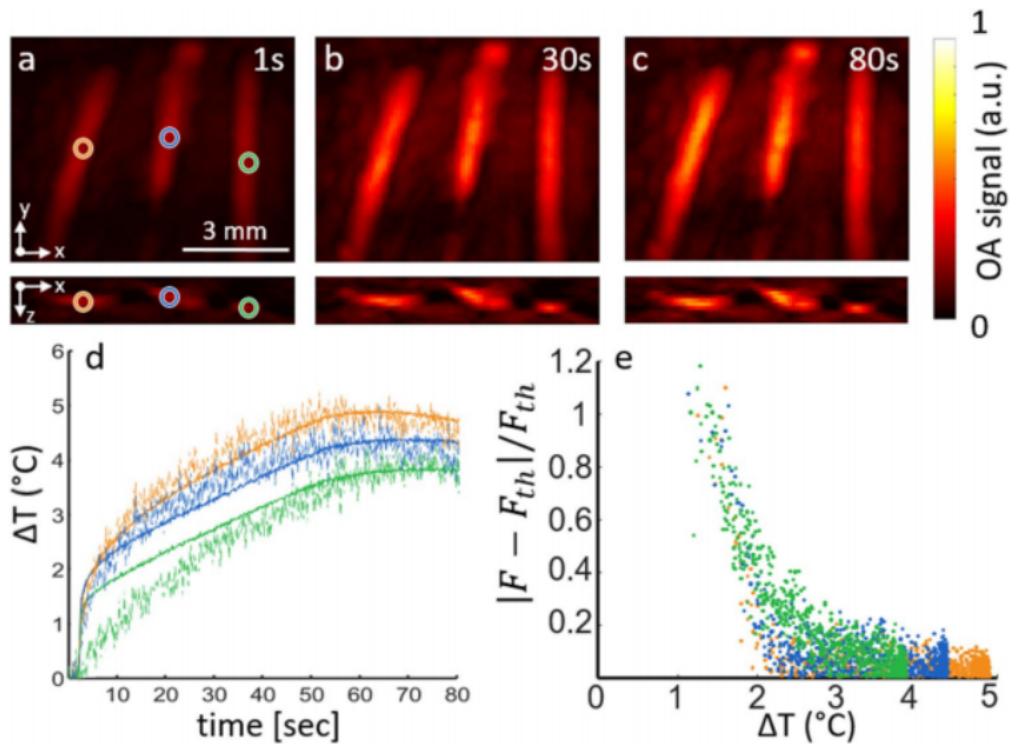


FIGURE 2.11: OA temperature estimations in a tissue mimicking phantom. (a-c) Transverse and coronal maximum intensity projection (MIP) OA images reconstructed for three different time points during laser heating of the phantom; (d) The temperature increase estimated from the OA signal variations (dashed curves) as compared to the temperature increase measured with thermocouples (solid curves). The regions of interest (ROIs) considered for the estimation are marked in panel a; (e) Relative deviation of the F factor from the theoretical value as a function of the temperature increase [33].

Figure 2.11 shows the OA images reconstructed at three different instants during the laser heating procedure. The laser ablation fiber was aligned parallel to the tubings at a distance of approximately 5 mm from the leftmost one. A progressive increase in the OA signal intensity as the temperature rises is clearly visible in all tubings, see Figure 2.11a-c. The temperature increase in blood was then estimated from Eq. 2.9, where the F factor was obtained according to Eq. 2.7. The estimated temperature increase inside the three tubings is plotted in Figure 2.11d (dashed lines). For calculating the relative signal increments in this experiment, a reference OA image (the baseline image) was taken as the average of 50 frames preceding the ablation procedure.

As measured, lower temperature increments resulted in larger disagreement between the optoacoustically-estimated temperature values and those measured with the thermocouples. Figure 2.11e indicates that the relative deviations in F remain below 10% if the temperature increases by at least 3 °C. These deviation can be partially attributed to the relative uncertainty in the measured Δp_0 values, see Eq. 2.9, originating from the noise in OA measurements. It must be also highlighted that discrepancy may also result from inaccuracies in the theoretical F values that were calculated assuming a homogeneous water medium.

In order to accomplish high resolution temperature mapping in real highly heterogeneous tissues, as it is a much more challenging task than pointwise temperature estimations since temperature diffusion while temperature rises will take place, we implemented a thermal diffusion model. The complexity of the problem arises when one thinks that the temperature elevation due to laser-induced heating depends on both the local light fluence distribution and the optical absorption coefficient. As a result, a highly non-uniform temperature distribution is expected to occur in heterogeneous tissues with many locations exhibiting low absorption or otherwise insignificant temperature alterations that cannot be accurately estimated by OA. To find a middle ground solution to these problems we therefore assumed that only voxels that generated OA signals above a certain threshold were reliable temperature estimates, set to 20% of the maximum signal in the entire 3D image stack recorded that corresponds to the time when the maximum contrast coming from the maximum

temperature reached takes place. The remaining 20% of the voxels temperature was assumed to be mainly increased by means of temperature diffusion from adjacent voxels exhibiting higher absorption values. The model based on the heat diffusion equation to dynamically estimate the volumetric temperature distribution is [122]

$$\frac{\partial T(r, t)}{\partial t} - D\nabla^2 T(r, t) = \frac{Q(r, t)}{\rho C_p} \quad (2.10)$$

where $T(r, t)$ is the spatio-temporal map of the temperature increase, $Q(r, t)$ is the heat absorbed in the tissue per unit volume and unit time and $D = k/\rho C_p$ is the thermal diffusivity, being k the thermal conductivity in [W/m°C]. The Green's solution to Eq.2.10 is given by

$$T(r, t) = \int_0^t \int_V \frac{Q(r, t')}{\rho C_p} g(r, t, r', t') dr' dt' \quad (2.11)$$

where $g(r, t, r', t')$ is given by [122]

$$g(r, t, r', t') = \frac{1}{(4\pi D(t-t'))^{3/2}} \cdot \exp\left(-\frac{|r-r'|^2}{4D(t-t')}\right) \quad (2.12)$$

Eq.2.11 is subsequently approximated by assuming that energy absorption takes place at finite number of points and time instants, leading to

$$T(r, t) \approx \sum_{i,j} T_{i,j}(r, t) \quad (2.13)$$

where

$$T_{i,j}(r, t) = \frac{E_i(t_j)}{\rho C_p} \left(\frac{1}{(4\pi D(t-t_j))^{3/2}} \right) \cdot \exp\left(-\frac{|r-r_i|^2}{4D(t-t_j)}\right) \quad (2.14)$$

For values that did exceed 20% of the maximum of the full stack, the temperature was solely estimated by relying on the instantaneous OA signal values $T(r_i, t_j)$ without considering thermal diffusion.

$$\Delta T_i(t_j) = T(r_i, t_j) - T(r_i, t_j - \Delta t) \quad (2.15)$$

Once having the thermal diffusion, we proceeded to test the performance of the presented approach on a post-mortem mouse ablation.

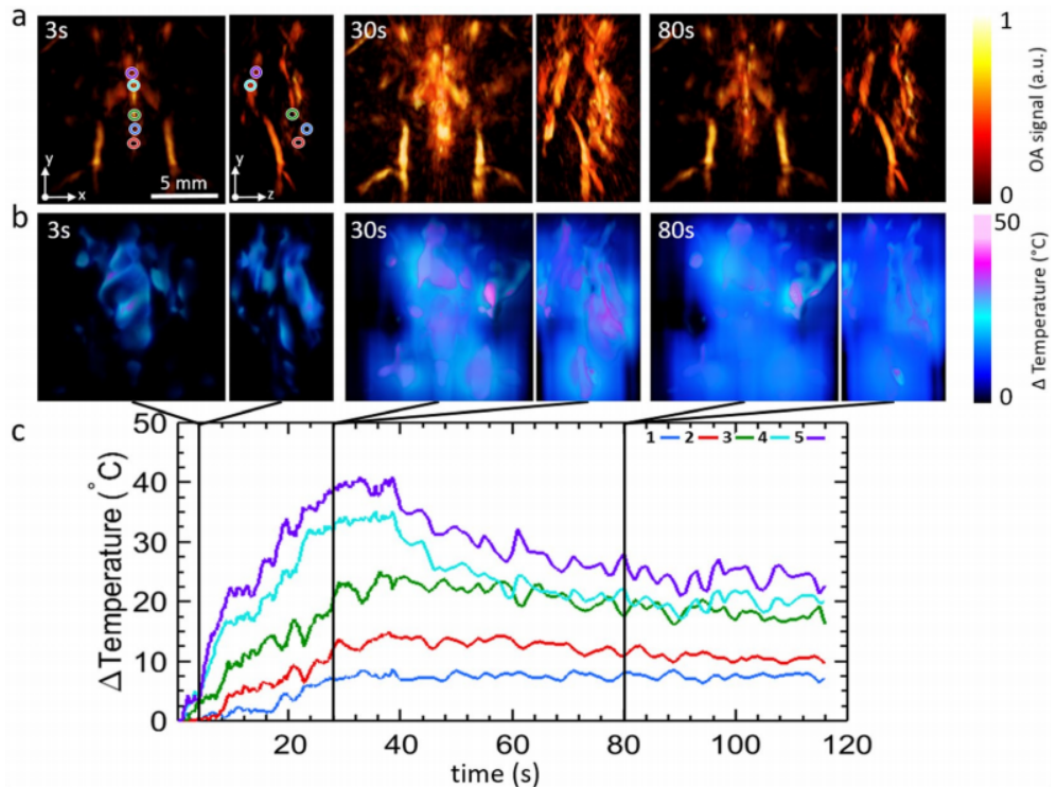


FIGURE 2.12: Volumetric OA monitoring of temperature during photothermal therapy performed in a mouse post mortem. (a) Transverse and lateral MIPs of the reconstructed OA volumes at different time points during the treatment. The tip of the ablation fiber is located approximately at the center of the displayed volumes. (b) Transverse and lateral MIPs of the estimated temperature maps at the same time points. (c) Actual temporal traces of temperature from the points labeled in (a). [33]

Figure 2.12 shows the reconstructed OA maximum intensity projections (MIPs) along the transverse and sagittal views for three different instants during the photothermal ablation. The OA images deliver 3D maps of the mouse anatomy at high spatial resolution in the $150 \mu\text{m}$ range while also showing rapid OA signal variations closely following the temperature rise. The dynamic temperature maps estimated via the methodology described in the Methods section are shown in Figure 2.12b. The plots

shown in Figure 2.12c depict the temporal evolution of the temperature profiles at 5 different locations, see Figure 2.12a. The points closer to the ablation fiber experience more pronounced temperature rise in the first few seconds following initiation of the ablation procedure and reach the maximum temperature approximately when the ablation laser is switched off, see Figure 2.12. Alternatively, lower peak temperatures and slower temperature changes are exhibited at locations away from the ablation fiber adjoining locations. Yet, due to thermal diffusion being the dominant effect maintaining the energy balance, temperature remains constant in those distant regions, see Figure 2.13.

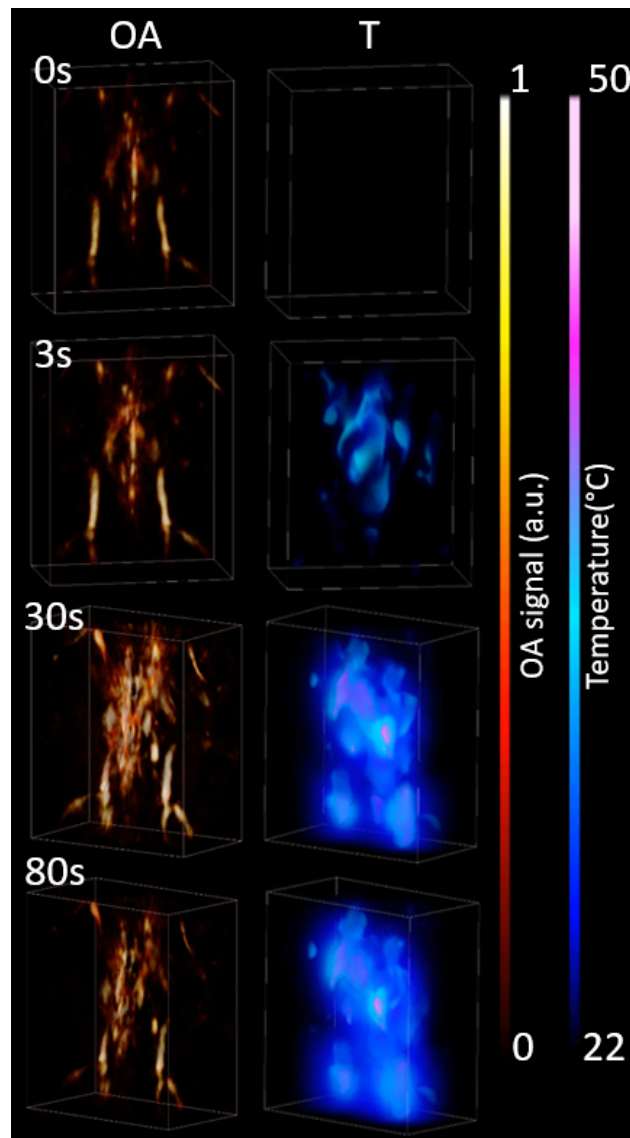


FIGURE 2.13: Real-time optoacoustic temperature monitoring during photothermal therapy video screenshots. Left: Volumetric OA image sequence. Right: Volumetric sequence of the estimated temperature maps during laser ablation. [33]

The method detailed in this section represents a new high-resolution volumetric temperature monitoring approach based on real-time acquisition of three-dimensional OA data, coupled with a thermal-diffusion-based model of heat distribution in tissues. It is expected that the present results anticipate the applicability of the suggested approach in various procedures involving laser-induced ablation in particular and thermal therapies in general.

2.4 Four-dimensional Optoacoustic Monitoring of Tissue Heating with Medium Intensity Focused Ultrasound

The OA temperature method presented in section 2.3 was further applied during an hyperthermic treatment that consisted of medium intensity focused ultrasound (MIFU) used in therapeutic interventions. MIFU with acoustic intensity levels between those used in echography and HIFU, typically $5\text{-}300\text{ Wcm}^{-2}$, represents a largely unexplored scientific niche that can lead to combined and cooperative thermal and non-thermal physical effects in soft tissues for performing physio or cancer therapy, either directly or via local drug delivery.

In a first calibration phase, two measurements were performed. First, a series of 150 V tone-bursts consisting of 255 cycles ($I_{SPTA} = 19.1\text{ Wcm}^{-2}$) were used to excite the MIFU array for 15 s. In Figure 2.14, the time dependence of temperature measured with the thermocouple versus the temperature estimated from the OA image sequence are represented by the solid and dashed blue lines, respectively. In a second measurement, a series of tone-bursts of 150 V and 125 cycles ($I_{SPTA} = 9.4\text{ Wcm}^{-2}$) were used to drive the MIFU array for 20 s. The corresponding temperature values are shown as solid and dashed lines for actual thermocouple temperature and OA computed temperature respectively.

The experiment was performed using a customized spherical matrix array composed of 256 piezoelectric elements with 90° (0.59π solid angle) angular coverage. Each element of the array has an area of $3\times 3\text{ mm}^2$, central frequency of 4 MHz and $>80\%$ detection bandwidth, providing a nearly isotropic imaging resolution of $200\text{ }\mu\text{m}$ around the geometrical center of the sphere. The OA detection array was positioned orthogonally with respect to the MIFU array and the entire setup was acoustically coupled immersed in water, see Figure 2.14.

Optical fluence of $\sim 11\text{ mJcm}^{-2}$ was measured at the surface of the sample at 720 nm illumination wavelength, corresponding to the maximum energy of the laser. The

pulse repetition frequency of the laser source was set to 10 Hz. The 256 optoacoustic signals corresponding to all elements of the array were simultaneously acquired at 40 mega-samples per second (MSPS).

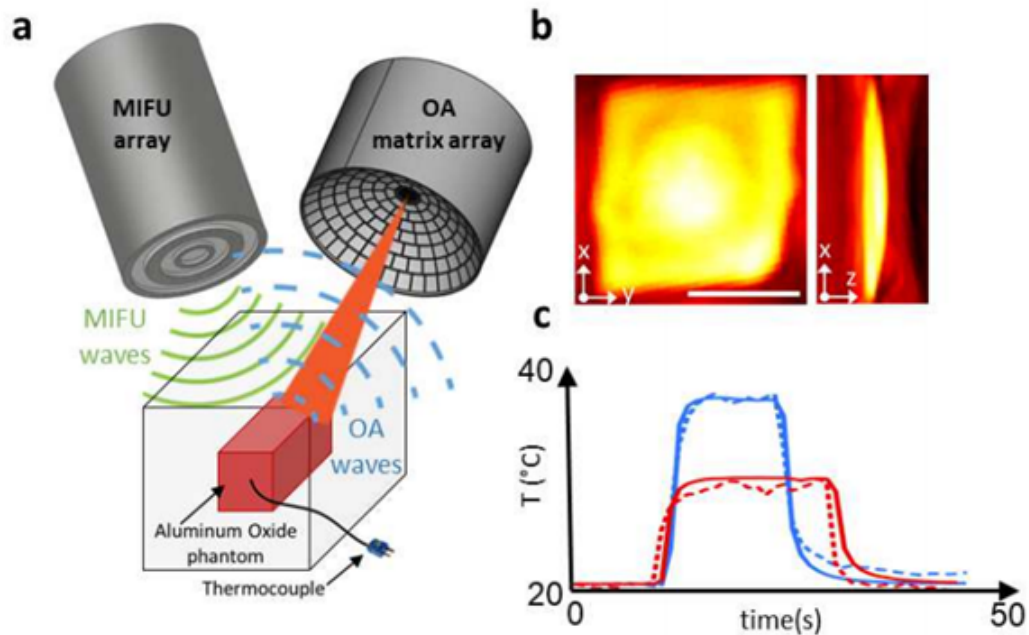


FIGURE 2.14: Schematic view of the experimental setup. (a) Drawings of the transducer array and the US system. (b) Transverse MIP optoacoustic images of the front and side views of the phantom. (c) Optoacoustic temperature validation (dashed lines) using the approach proposed in this section. The thermocouple readings (continuous lines) from the same color, represent the two different US heating procedures, at 255 (blue) and 125 (red) cycles.

It was observed, that the OA-estimated temperature acceptably matches the thermocouple readings, see Figure 2.14. Specifically, the standard deviations of the differences between the corresponding time profiles in Figure. 2.14C are 0.65 °C and 0.88 °C for tone-bursts of 125 and 255 cycles, respectively. The good agreement is probably a consequence of the fact that the phantom consists of an aqueous solution, for which Eq. 2.15 is expected to be valid. Inaccuracies may originate from the discrepancy between the actual location of the thermocouple tip and the analyzed OA traces.

Secondly, we investigated the possibilities of detecting the MIFU focus which is the same region of the bovine tissue with highest temperature increase.

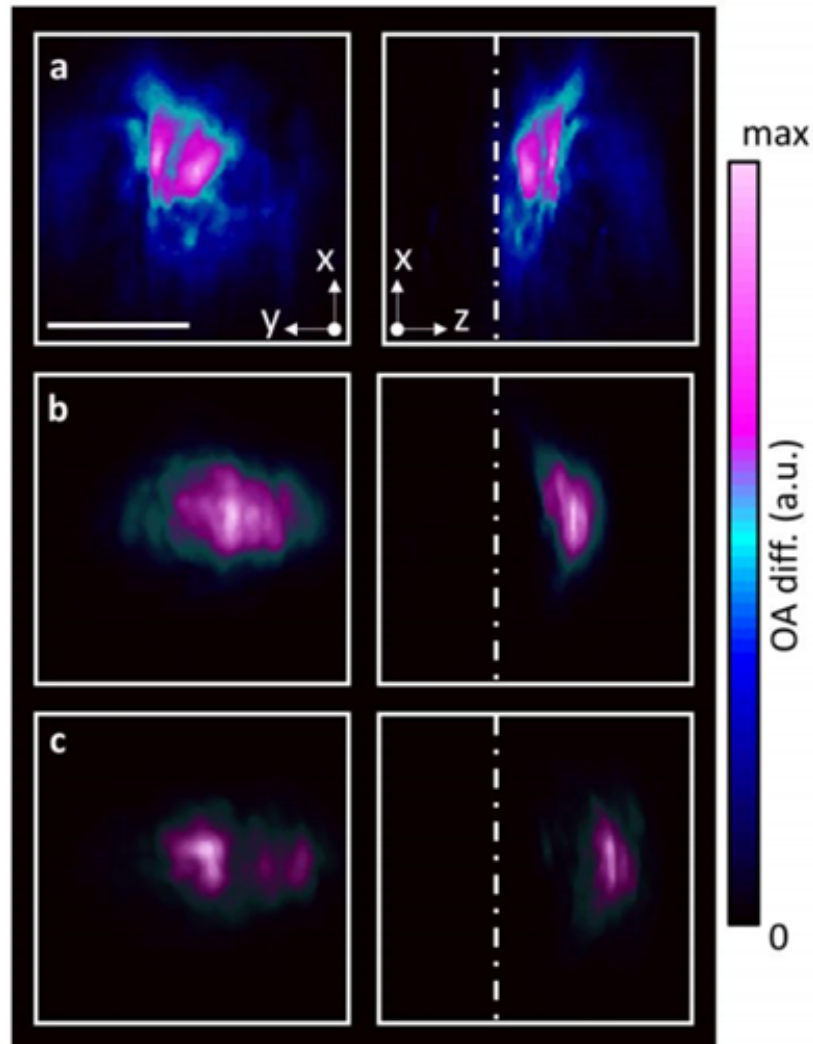


FIGURE 2.15: MIPs of the differential 3D OA images along the z and y directions from ex-vivo bovine tissue for the US focus located at a reference position right underneath the tissue surface (a) and at 1.5 mm (b) and 3 mm (c) points deeper than the reference position, respectively. Scalebar – 5 mm.

The difference of the OA images of the bovine tissue taken after and before MIFU heating (150 V tone-bursts, 255 cycles, are displayed in Figure 2.15. The tissue surface is indicated with a dashed line. No significant heat diffusion was produced during the heating period, so that the differential images reliably represent the heated region, namely, the US focus. The difference in the signal amplitude for the different US focus depths is due to light attenuation, which also results in a lower signal to noise ratio (SNR) at deeper locations. This in turn limits the maximum applicable depth for OA monitoring of the MIFU treatments.

Lastly, once the system had been calibrated, we investigated further the performance of temperature mapping in real-time in ex-vivo bovine tissue.

It can be seen that the temperature map estimated for the time point of peak temperature elevation, see Figure 2.16a at 20 s, is tightly centered around the ultrasonic focus location. On the other hand, the heated region spreads over a larger region at later time points during the cooling period, see Figure 2.16a at 24 s, which indicates that thermal diffusion plays a dominant role in carrying the heat further away from the ultrasonic focus. This is further corroborated in the time traces in Figure 2.16b, corresponding to the estimated temperatures at three locations indicated in Figure 2.16a.

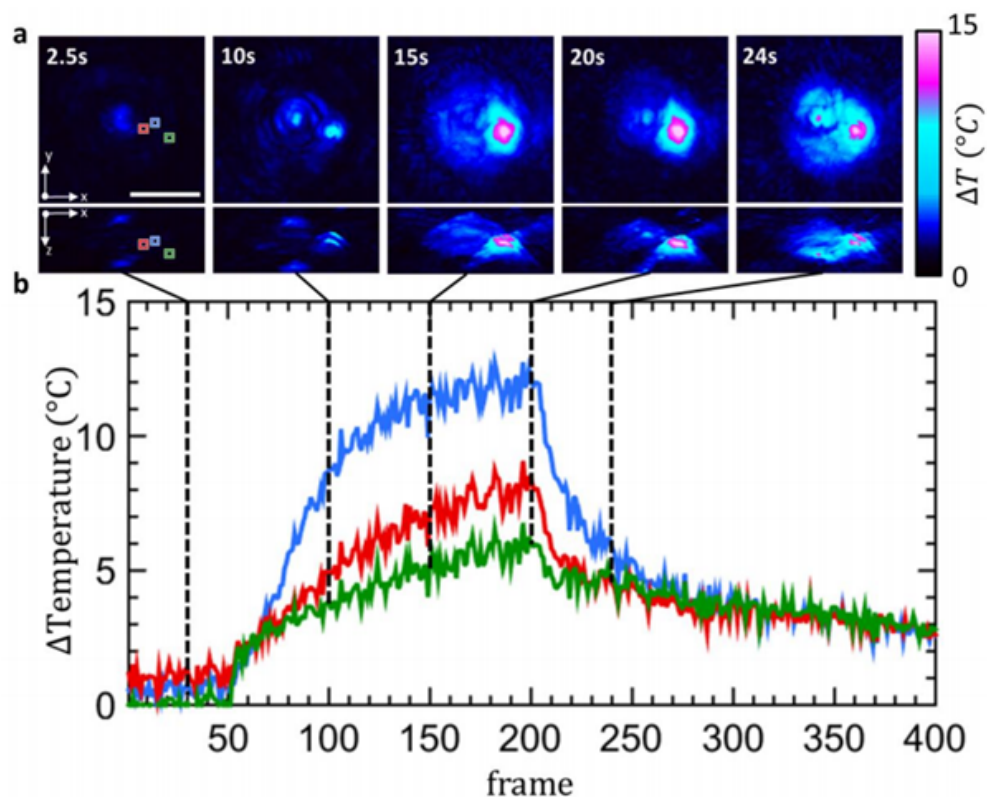


FIGURE 2.16: Volumetric OA monitoring of temperature during MIFU therapy performed in an ex-vivo bovine tissue. (a) MIPs of the estimated 3D temperature increase maps at different time points along the procedure. Scalebar – 5 mm. (b) Temporal profiles of the estimated temperature increase for the 3 points labeled in (a) with their respective color.

The lack of simple and reliable non-invasive temperature feed-back represents a major barrier towards broader adaptation of thermotherapy procedures in pre-clinical research and clinical routine. With the results presented in this section, volumetric OA imaging may emerge as a promising tool for quantitative monitoring of the temperature field during thermal therapies. In the experiments performed for this research, the temperature dependence of the Grüneisen parameter was adopted from an empirical formula for aqueous solutions, which may not accurately represent the physical reality in soft biological tissues and thus an individual calibration of the Grüneisen parameter would be preferred in future investigations [119].

The new high-resolution volumetric temperature monitoring methods presented in this section are based on real-time acquisition of three-dimensional optoacoustic data coupled with a thermal-diffusion-based model of heat distribution in tissues. It is expected that the present results anticipate the applicability of the suggested approach in various procedures involving laser and medium intensity therapeutic US thermotherapies.

The monitoring approach presented in this section can potentially be applied in treatments based on selective tissue destruction with HIFU [127]. The advantages derived from the achieved temperature sensitivity during US heating combined with the high spatial resolution and fast real-time volumetric imaging rates, are expected to improve the outcome in various procedures involving low and medium intensity therapeutic US, such as physical rehabilitation, pain management or neurostimulation [127].

2.5 Optoacoustic Monitoring of RF Ablation Lesion Progression

Efficient monitoring of ablation procedures is essential for improving the treatment outcome as well as to avoid unnecessary tissue damage [125]. OA imaging and sensing systems are able to real-time monitor tissue ablation with high contrast and by

using only non-ionizing excitation [126]. OA presents unique advantages for this purpose since the thermo-elastic conversion efficiency is highly sensitive to temperature variations, see Eq. 2.6 [127], and tissue coagulation leads to chemical changes further affecting the OA signal intensity [128]. These two effects are clearly evinced in experiments performed for calibrating the temperature dependence of OA signals, see Figure 2.11. The increase in OA signal intensity per °C remains approximately constant for temperatures below 50°C, where it abruptly changes [129].

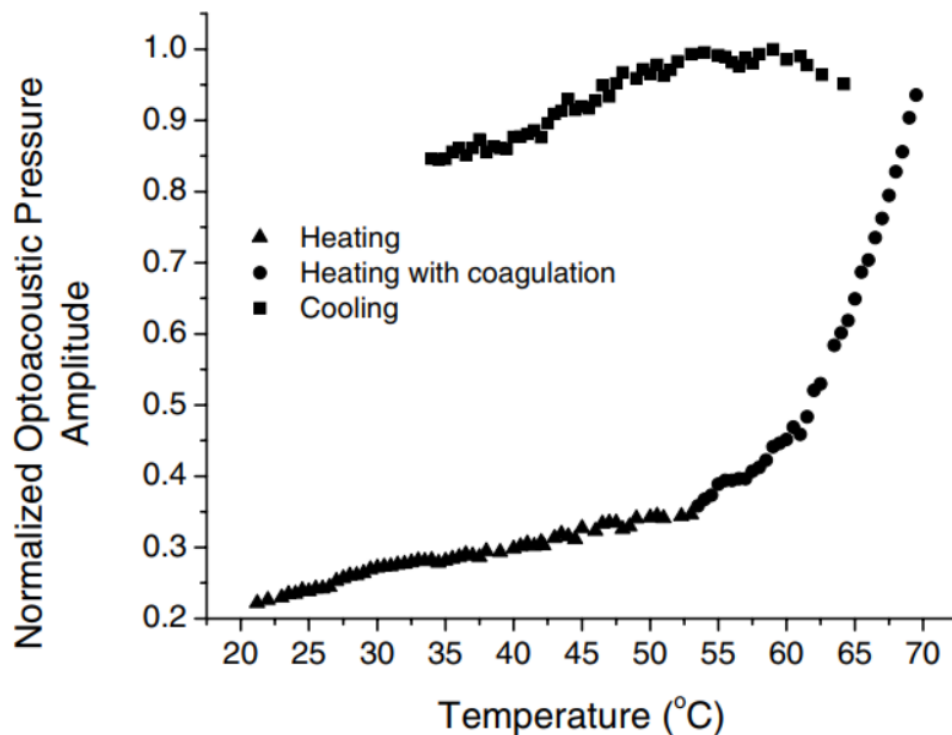


FIGURE 2.17: Optoacoustic pressure amplitude induced in canine liver during conductive heating and passive cooling. The triangles represent heating without coagulation; circles – heating with coagulation; squares – passive cooling of the sample. [124]

As showcased in Section 2.3., real-time temperature mapping is reliable for temperatures below coagulation thresholds [33]. It is known that the resulting lesion size of an ablation treatment depends both on temperature and exposure time [15], and OA temperature readings are inaccurate when ablation is produced [124]. Tissue coagulation further leads to a change in optical attenuation [130], which in turn produces distortion (spectral coloring) of the absorption spectrum at deep locations.

Larin et. al., studied the typical OA peak pressure amplitude induced in a canine liver during conductive heating and passive cooling of the tissue sample, see Figure 2.17. In this thesis, we suggest this approach for characterizing the evolution of the induced lesion based on identifying sharp positive variations in the OA time profiles extracted from the sequence of images acquired. Multi-spectral OA imaging, based on tissue excitation at multiple optical wavelengths, can further provide additional information encoded both in the time and spectral dimensions in future works [88]. The approach proposed is based on detecting sharp positive variations in the time derivative of OA signals.

RF ablation was performed in a porcine tissue sample with approximately 10 mm thickness. Figure 2.18a displays the lay-out of the experimental setup. The RF catheter containing the electrical excitation was positioned orthogonally to the surface of the tissue sample. Thermal coagulation began when the tissue resistance to the electrical input leads to a joule-effect temperature increase above the tissue-specific temperature and time of exposure time for tissue denaturation. The procedure was monitored in real-time by illuminating the region of interest treated beneath the electrode. The guiding fiber bundle delivered approximately 20 mJ of electromagnetic radiation provided with a 10 Hz short-pulsed (<10 ns) laser and it diffused and scattered at the surface of the sample, subsequently leading to an exponential fluence decay in the direction of the beam path.

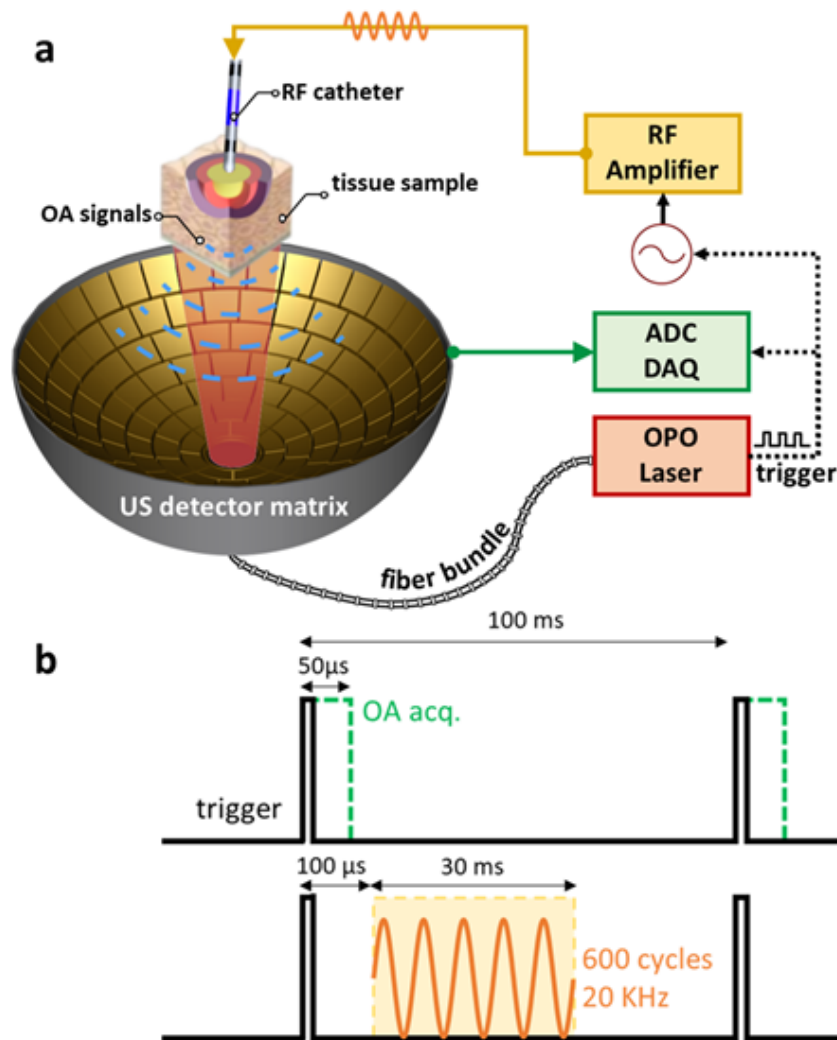


FIGURE 2.18: Schematic view of the experimental setup of the ablation experiment. (a) Drawings of the OA transducer array and RF system network. (b) Schematic synchronization diagram of the OA and RF excitations and acquisition routines.

Figure 2.19 displays the relative increase in OA signal intensity during ablation for a point located at 6 mm depth. Considering that soft biological tissues mainly consist of water, Eq. 2.9 can be taken as a reasonable approximation as increase in temperature is proportional to the relative increase in OA signal. Thereby, the estimated time profiles of temperature are equivalent to those shown in Figure 2.19 for temperatures below the ablation temperature threshold, typically 50 °C. However, this approximation is no longer valid when ablation takes place as additional changes in the Grüneisen parameter are produced.

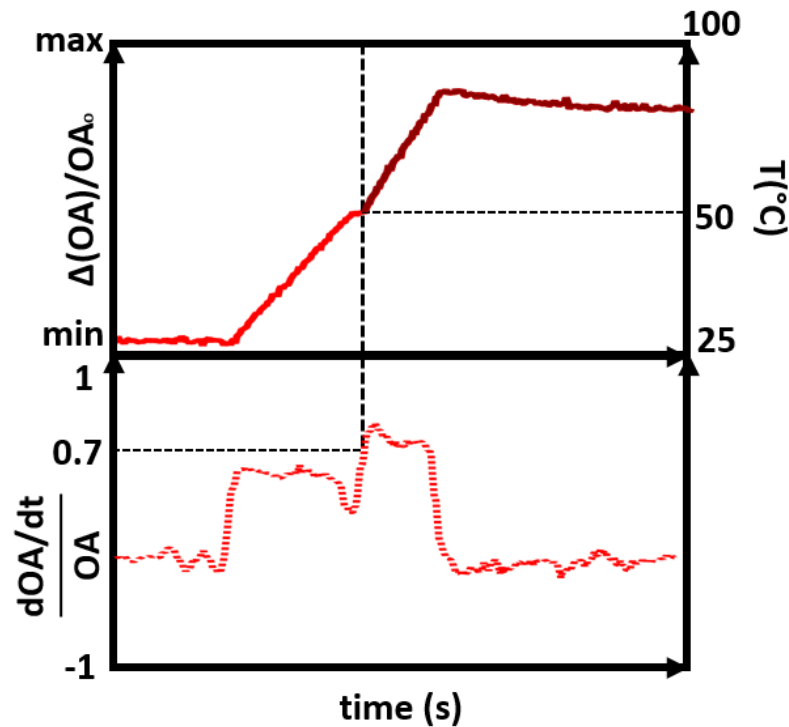


FIGURE 2.19: Computational method for estimation of coagulated lesion size during RF ablation by means of the OA signal derivative. The higher panel shows the OA signal increment based temperature computation, the panel below plots the OA signal derivative.

Testing of the proposed approach was carried out in a porcine heart sample with an average power of 9W. The estimated temperature time profiles are shown in Figure 2.19 in the above panel for temperatures below coagulation threshold. The time point when the ablation temperature threshold is reached can be identified in the temperature profile, this trigger represents the onset of ablation that serves to estimate how the lesion propagates with time. The panel below in Fig. 2.19 displays the numerically estimated time derivative of the OA pressure signal ($\delta p_0/\delta t$). Four different intervals can be clearly distinguished. In the baseline interval, $\delta p_0/\delta t = 0$. $\delta p_0/\delta t$ subsequently reaches defined positive values in a second and third stage intervals, while it eventually becomes slightly negative in the last interval.

The significant change in $\delta p_0/\delta t$ between the second and third interval is consistent with the previously reported change in slope of the OA signal intensity vs. pressure

when ablation is produced [127]. Ablation begins between the second and third intervals in the $\delta p_0/\delta t$ curve.

This way, a map of the onset time of ablation can then be estimated from the time points between the second and third intervals by setting a threshold in $\delta p_0/\delta t$ for the voxels in the image. It is also noticeable the decrease at the beginning of the fourth interval. This is arguably due to the fact that the light fluence is reduced when ablation at deep regions starts. The onset of ablation leads to an increased optical attenuation and consequent decrease in light fluence and OA signal in the entire volume. Thereby, a sharp increase in OA signal is only produced for the timepoints when ablation starts, and the identification of these points represents a robust approach for assessing the progression of the lesion being formed.

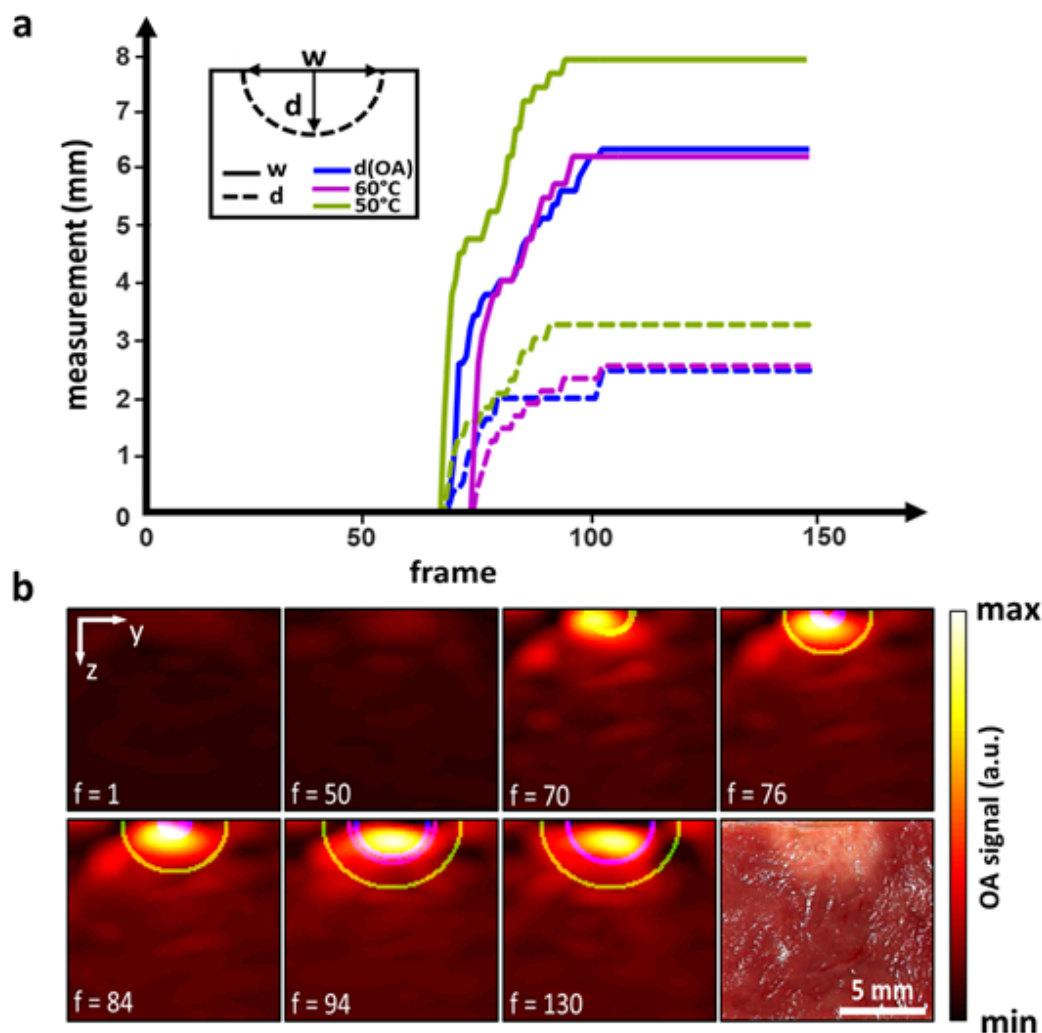


FIGURE 2.20: Lesion boundary progression dimensions for width (w) and depth (d) of the ablated tissue displayed with continuous and dashed lines respectively. Applying the OA signal derivative method (blue), the standard 50°C temperature coagulation threshold method (green) and the iterated temperature threshold attaining similar final lesion size as the direct OA derivative method, results in 60°C. (b) Coagulation boundary regions overlaid on top of the actual fluence-corrected OA images at different time-points during the treatment and the post-ablation cross-sectional view of the porcine tissue sample.

The newly suggested approach, see Figure 2.20, based on analyzing the changes in the temporal derivative of the OA signals does not rely on temperature estimations and hence it is expected to be more robust than alternative approaches. Indeed, the temperature ablation threshold can vary for different tissue types and hence the lesion size can be erroneously estimated even when considering an imaging approach

that accurately maps the temperature distribution. Abrupt changes in the OA signal intensity can also enable identifying the onset of coagulation in ablation procedures based on a relatively large exposure time. Furthermore, the reported increase in optical attenuation in ablated tissues results in a reduced light fluence at deep locations [134]. Thereby, positive changes in the time derivative of OA signals are exclusively due to coagulation and can be detected at any point of the target tissue regardless of the light delivery method for OA excitation.

The newly suggested method has been enabled by the unique OA capabilities for high-frame-rate imaging in three dimensions and for sensing chemical transformations taking place during coagulation. The fact that single wavelength excitation is sufficient for detecting such changes can also significantly reduce the cost of clinical embodiments. These features, along with the fact that non-ionizing radiation is employed, represent unparalleled advantages of OA with respect to other imaging modalities that can potentially be used for fast RFA detection.

Chapter III

Publications

Chapter 3

Publications

NONCONTACT MONITORING OF INCISION DEPTH IN LASER SURGERY WITH AIR-COUPLED ULTRASOUND TRANSDUCERS [1]

Peer-reviewed Journal Paper

Autors: Francisco Javier Oyaga Landa^{1,2}, Xosé Luís Deán-Ben¹, Francisco Montero de Espinosa³, and Daniel Razansky^{1,2,*}

Affiliations:

¹Institute for Biological and Medical Imaging (IBMI), Helmholtz Center Munich, Neuherberg, Germany

²School of Medicine, Technical University of Munich, Germany

³CSIC, Institute of Physics and Communication Technologies, Madrid, Spain

*Corresponding author.

In: Optics Letters, 2016 Jun 15; 41(12): 2704-7.

Abstract: Lack of haptic feedback during laser surgery makes it difficult to control the incision depth, leading to high risk of undesired tissue damage. Here, we present a new feedback sensing method that accomplishes noncontact real-time monitoring of laser ablation procedures by detecting shock waves emanating from the ablation spot with air-coupled transducers. Experiments in soft and hard tissue samples attained high reproducibility in real-time depth estimation of the laser-induced cuts. The advantages derived from the noncontact nature of the suggested monitoring approach are expected to advance the general applicability of laser-based surgeries.

Contribution of thesis author: Laboratory measurements, processing algorithms, signal analysis and computer-aided results and methods.

Copyright Notice: Copyright © 2017, OSA Publishing, The Optical Society, Optics Letters.

Optics Letters

Noncontact monitoring of incision depth in laser surgery with air-coupled ultrasound transducers

FRANCISCO JAVIER OYAGA LANDA,^{1,2} XOSÉ LUÍS DEÁN-BEN,¹ FRANCISCO MONTERO DE ESPINOSA,³ AND DANIEL RAZANSKY^{1,2,*}

¹Institute for Biological and Medical Imaging (IBMI), Helmholtz Center Munich, Neuherberg, Germany

²School of Medicine, Technical University of Munich, München, Germany

³CSIC, Institute of Physics and Communication Technologies, Madrid, Spain

*Corresponding author: dr@tum.de

Received 19 February 2016; revised 21 April 2016; accepted 13 May 2016; posted 16 May 2016 (Doc. ID 259647); published 3 June 2016

Lack of haptic feedback during laser surgery makes it difficult to control the incision depth, leading to high risk of undesired tissue damage. Here, we present a new feedback sensing method that accomplishes noncontact real-time monitoring of laser ablation procedures by detecting shock waves emanating from the ablation spot with air-coupled transducers. Experiments in soft and hard tissue samples attained high reproducibility in real-time depth estimation of the laser-induced cuts. The advantages derived from the noncontact nature of the suggested monitoring approach are expected to advance the general applicability of laser-based surgeries. © 2016 Optical Society of America

OCIS codes: (120.0280) Remote sensing and sensors; (170.1020) Ablation of tissue; (150.5495) Process monitoring and control; (110.5125) Photoacoustics; (110.5120) Photoacoustic imaging.

<http://dx.doi.org/10.1364/OL.41.002704>

Laser surgery is an advantageous alternative to scalpel-based procedures, which are often afflicted with excessive mechanical traumatization and bacterial contamination. Pulsed laser ablation results in vaporization and ejection of tissues, leading to generation of laser-induced shock waves at the incision spot. This ablation mechanism is already exploited by an ample spectrum of laser-tissue applications [1–3]. For example, it has been shown that efficient laser osteotomy can be performed at laser fluence levels of around 160 J/cm² [4]. Laser-based incisions offer minimally invasive intervention with less collateral damage, more efficient hemo- and bacterio-stasis, and less post-operative pain and swelling [5]. These advantages have inspired the application of pulsed laser surgery in a wide range of clinical procedures involving cutting soft and connective tissues, e.g., in dermatology, ophthalmology, or oncology [5–9].

To this end, a number of optical and acoustic readout mechanisms have been proposed for monitoring laser surgeries [10–13]. However, lack of accurate haptic feedback and real-time control over the lesion profile remain the major challenges of laser-based surgical procedures, severely limiting the range of

potential applications. Monitoring of the incision depth also has been attempted using kinesthetic and vibrotactile haptic feedback [14], yet only initial demonstration in homogenous agarose phantoms for a limited penetration depth of 1–2 mm was presented. Recently, it was demonstrated that acoustic detection of shock waves can be used as a feedback mechanism to monitor the incision depth during laser ablation. By using a matrix array of ultrasound detection elements, the feasibility of 3D localization of the incision profile was showcased in *ex vivo* samples [15]. However, the need of an acoustic matching medium (typically water or ultrasound gel) between the ablated tissue and the feedback detector may affect the achievable ablation rate by altering the effective heat capacity of the tissue surface while the contact-based approach may further hamper the general applicability of such monitoring method in a real clinical setting.

It has been previously shown that the noncontact detection of pressure (ultrasound) waves from remote locations is possible by means of air-coupled transducers [16], which are specifically designed to reduce the tremendous acoustic mismatch between air and ultrasound sensing elements. Efficient coupling to the air medium can be performed with micro-membrane capacitance transducers [17] or with piezoelectric sensors coupled with microporous layers, with the latest approach more convenient for frequencies above 1 MHz [18]. Air-coupled transducers have recently been shown to provide sufficient sensitivity for performing noncontact optoacoustic (OA) imaging using laser fluence levels below 20 mJ/cm² [19]. It is therefore expected that air-coupled detection is the ideal candidate for efficient detection of shock waves generated during laser ablation procedures, which often involves fluence levels beyond 10 J/cm² [20]. In this Letter, we investigate the feasibility of monitoring the incision depth in laser cutting by measuring the time of flight of the generated pressure waves with air-coupled transducers.

A layout of the experimental setup is shown in Fig. 1(a). Laser ablation was performed with a frequency-doubled Q-switched Nd:YAG laser (Spectra Physics, Santa Clara, CA) operating at 532 nm with a pulse duration of approximately 7 ns. In order to create ablation, we used per-pulse energies

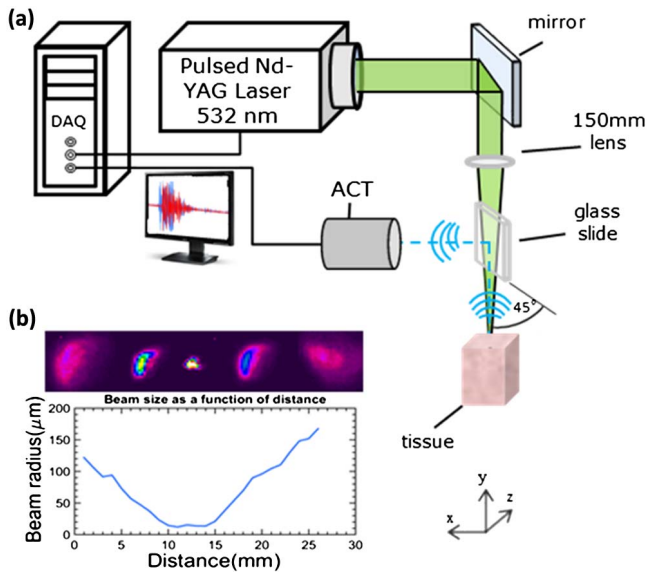


Fig. 1. (a) Layout of the experimental setup. ACT, air-coupled transducer; DAQ, data acquisition. The glass slide (1.1 mm thickness) is positioned at 45° relative to the propagation direction of the shock-waves so that the acoustic waves are reflected at 90° into the ACT. (b) Ablation beam characterization in the vicinity of the focal region. Typical beam shapes are shown in the inset. The effective depth of focus is approximately 5 mm.

above 40 mJ and a pulse repetition frequency of 15 Hz. The laser beam was focused using a lens with 150 mm focal distance (Thorlabs, Newton, NJ). In all experiments, the focal point was located ~ 3 mm under the tissue surface. We characterized the ablation beam size as a function of distance using a camera-based SP620U beam profiler (Spiricon Ophir Photonics, North Logan, UT). The beam diameter shrinks down to 30 μm at the focus, inducing fluence levels up to 5 kJ/cm^2 [Fig. 1(b)]. Under these conditions, the laser beam was able to perform deep incisions in both soft and hard (bone) tissue. Specifically, three different types of tissue were ablated, including liver cheese (German: *leberkäse*), chicken breast, and chicken bone. While *leberkäse* samples are considered to be relatively heterogeneous, fat and connective tissue were removed from the chicken breast and bone tissues, resulting in more homogeneous samples.

Shock waves emitted from the ablation spot were detected with a self-developed unfocused air-coupled piezoelectric transducer with a central frequency of 0.8 MHz and -6 dB bandwidth of 0.4 MHz [21]. The transducer is based on a flat 1–3 piezocomposite with a 20 mm diameter active area. It was positioned at an acoustic travel distance of 50 mm from the tissue surface using a glass slide oriented at 45° so that the focused light beam can propagate without changing its direction while the acoustic waves are reflected at 90° (Fig. 1). The pressure signals collected by the transducer were amplified by 30 dB and digitized at 10 megasamples per second with 12 bit vertical resolution by means of a PCI Express acquisition card (Model ATS9351, AlazarTech, Pointe-Claire, QC, Canada) triggered with the Q -switch output of the laser.

The time of arrival of the measured shock waves was estimated as the instant for which the pressure signal level exceeds a

defined threshold, which was set to 16% of the maximum value for the entire signal sequence. It was further assumed that the ablation spot is always located at the bottom of the cut so that it deepens as the incision progresses, thus increasing the delay in the time of arrival of the waves at the transducer surface. The time of flight difference (TOFD) of the generated shock waves due to propagation inside an open cut is then estimated as the difference in the time of arrival T_i for each detected shock wave with respect to an average time of arrival T_0 for the signals generated by the first 20 laser pulses.

Assuming the speed of sound within the incision c_i is known, one could provide an estimate on the incision depth d according to

$$d = c_i \cdot \text{TOFD}. \quad (1)$$

In the experiments, we used 40 *leberkäse* samples, 30 samples of chicken breast, and 20 samples of chicken bone. The incision depths ranged from 1 to 4 mm for soft tissue samples (*leberkäse* and chicken breast) and from 1 to 8 mm for the osseous tissues. The thickness of the samples was ~ 10 mm. Figures 2(a)–2(c) show examples of the time-resolved signals recorded by the air-coupled transducer for the three different tissue types. The recorded waveforms are increasingly delayed as the incision progresses, indicating deepening of the lesion. Figures 2(d)–2(f) show three examples of the measured TOFD of the shock waves for the entire pulse sequence. It is generally expected that the shock waves generated by the laser pulse propagate at supersonic speeds in the immediate vicinity of the ablated spot but rapidly slow down to the speed of sound for normal (linear) wave propagation [3].

Note, however, that the different tissues exhibit significant variations in the TOFD. For instance, a 2 μs delay of the time of arrival was observed for *leberkäse* [Fig. 2(d)] following 300 laser shots, whereas the corresponding delay for the chicken breast [Fig. 2(e)] and bone [Fig. 2(f)] was 5.5 and 1 μs , respectively. One also may note that the time of arrival slightly decreases in the starting phase of the bone tissue ablations

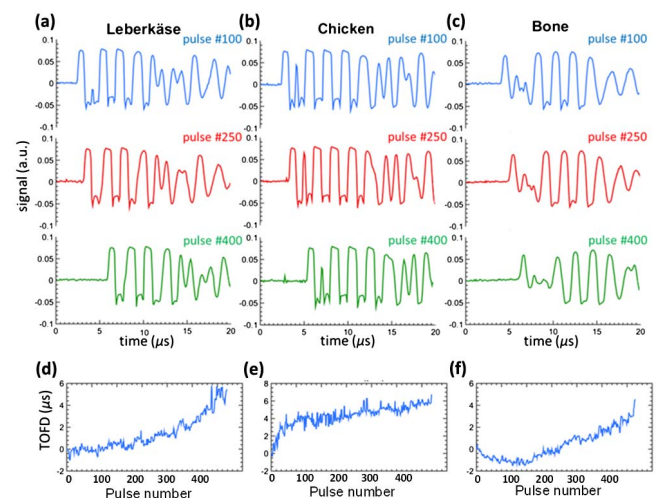


Fig. 2. Illustration of the method used to estimate the speed of sound within the incision profile for different tissue types. Examples of the recorded signals for (a) *leberkäse*, (b) chicken, and (c) bone. Each color corresponds to three different instants, namely, pulse #100, #250, and #400 after the ablation start. Evolution of the corresponding TOFD is shown in (d)–(f).

[see a representative example in Fig. 2(f)], which may be attributed to accumulation of thermoelastic effects at the tissue surface before the actual tissue vaporization takes place. In general, the time of arrival exhibits unsteady behavior in the starting phase of the ablation for all tissue samples. Most time-resolved signals are also characterized by lengthy oscillations, presumably due to residual light absorption in previously generated tissue debris within the crater. Some abrupt variations in the time of arrival also can be attributed to random ablation events occurring in particles suspended in air before the light pulses reach the tissue. The values of the speed of sound inside the incision profile were estimated by considering the actual (final) incision depth d_f measured in post-ablated tissue slices and the average time of flight difference recorded for the last 20 laser pulses TOFD_f via

$$c_i = d_f / \text{TOFD}_f. \quad (2)$$

The calculated values of c_i are shown in Fig. 3 as a function of the measured final incision depth. One may note that, for soft tissue samples, the average estimated c_i increases versus incision depth [Figs. 3(a) and 3(b)]. Specifically, c_i reaches average values of 750 and 570 m/s for 3–4 mm cuts in the leberkäse and chicken breast specimens, respectively. For shallow incisions, the average c_i values remained close to the speed of sound in air (343 m/s for dry air at 20°C). This may indicate that deeper cuts in soft tissue samples (leberkäse and chicken breast) have been filled up with material expelled by the ablation events, so that the shock waves propagate through a mixed air–tissue medium. Conversely, the average value of c_i better matches the speed of sound in air for bone samples, even for considerably deeper cuts [Fig. 3(c)]. This implies that the extracted volume is mainly filled with air during the ablation of bones. Finally, by substituting the c_i values according to the linear fits in Figs. 3(a)–3(c) and the measured TOFD values from Fig. 2 into Eq. (1), one may obtain real-time estimates for the incision depth for the three experiments presented in Fig. 2, as shown in Figs. 3(d)–3(f). The actual

incision profiles corresponding to the measurements presented in Figs. 3(d)–3(f) are further shown in Figs. 3(g)–3(i).

The presented results demonstrate basic feasibility of attaining real-time feedback on the laser-induced incision depth by means of noncontact detection of the generated shock waves with air-coupled transducers. Several clinical applications may greatly benefit from this newly discovered approach. In melanin pigmentation treatments, maxillofacial surgery, and precancerous lesion or benign tumor removal, the performance of laser-based surgery procedures is often hindered by the lack of online depth monitoring. According to the presented results, our method is anticipated to provide accurate estimates on the incision depth in bones, making it ideally suited for accurate monitoring of lesion depth in laser osteotomy. Accordingly, the higher variability of speed of sound inside soft tissue incisions is expected to introduce corresponding uncertainties into the incision depth estimates. However, this variability remains low for incision depths below 1–2 mm where the method is expected to provide accurate estimates.

An efficient handheld design is a key next step for translating this technology into common clinical setting, which also would necessitate devising a different light guiding approach. Yet, a certain window of applicability also may exist for stationary ablation systems design. It is expected that more accurate selection and calibration of the ablation parameters for the different tissue types (laser energy, focal distance, optical fluence at the surface) may further enhance the performance of the method.

In conclusion, we presented a new method for monitoring laser ablation procedures, which accomplishes real-time tracking of the incision depth by detection of shock waves emanating from the ablation spot with air-coupled transducers. The advantages derived from the noncontact nature of the suggested monitoring approach are expected to advance the general applicability of laser-based surgeries.

Funding. Deutsche Forschungsgemeinschaft (DFG) (RA 1848/5-1); Comisión Interministerial de Ciencia y Tecnología (CICYT) (DPI2013–46915-C2-1-R).

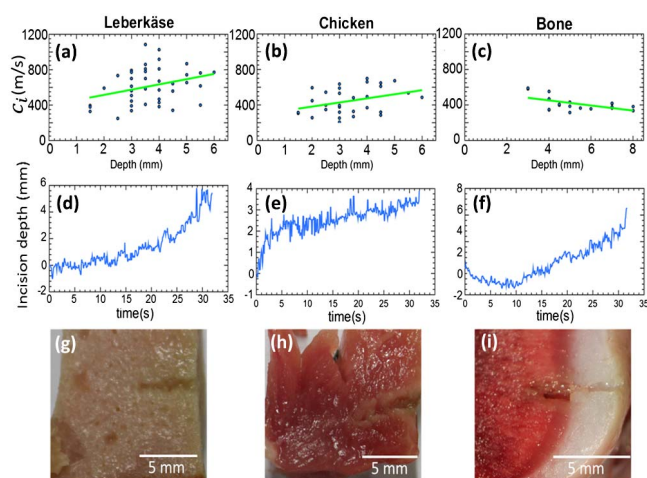


Fig. 3. (a)–(c) Distribution of the estimated speed of sound within the incision based on measurements performed on sliced specimen. Green lines correspond to the linear fit through the scattered data. Examples of real-time incision depth estimations for the tissue samples in Fig. 2 are presented in (d)–(f). Actual photographs of the sliced samples are shown in (g)–(i), respectively.

REFERENCES

- J. T. J. Walsh and T. F. Deutsch, *Appl. Phys. B* **52**, 217 (1991).
- R. O. Esenaliev, A. A. Oraevsky, V. S. Letokhov, A. A. Karabutov, and T. V. Malinsky, *Lasers Surg. Med.* **13**, 470 (1993).
- T. Juhasz, X. H. Hu, L. Turi, and Z. Bor, *Lasers Surg. Med.* **15**, 91 (1994).
- S. Stübinger, B. von Rechenberg, H. Zeilhofer, R. Sader, and C. Landes, *Lasers Surg. Med.* **39**, 583 (2007).
- F. W. Neukam and F. Stelzle, *Phys. Procedia* **5**, 91 (2010).
- G. K. Eyrich, *Med. Laser Appl.* **20**, 25 (2005).
- J. M. White, H. E. Goodis, and C. L. Rose, *Lasers Surg. Med.* **11**, 455 (1991).
- A. Tuchmann, P. Bauer, H. Plenke, and O. Braun, *Res. Exp. Med.* **186**, 375 (1986).
- A. Vogel and V. Venugopalan, *Chem. Rev.* **103**, 577 (2003).
- F. Stelzle, A. Zam, W. Adler, K. Tangemann-Gerk, A. Douplik, E. Nkenke, and M. Schmidt, *J. Transl. Med.* **9**, 20 (2011).
- D. C. Jeong, P. S. Tsai, and D. Kleinfeld, *Curr. Opin. Neurobiol.* **22**, 24 (2012).
- B. M. Kim, M. D. Feit, A. M. Rubenchik, B. M. Mammini, and L. B. Da Silva, *Appl. Surf. Sci.* **127–129**, 857 (1998).
- K. Nahan and A. Vogel, *Lasers Surg. Med.* **25**, 69 (1999).
- L. Fichera, C. Pacchierotti, E. Olivieri, D. Prattichizzo, and L. S. Mattos, in *IEEE Haptics Symposium* (2016), pp. 59–64.

15. E. Bay, X. L. Deán-Ben, G. A. Pang, A. Douplik, and D. Razansky, *J. Biophoton.* **8**, 102 (2015).
16. M. J. Garcia-Hernandez, J. A. Chavez, Y. Yañez, H. B. Kichou, J. L. Prego-Borges, J. Salazar, A. Turo, and F. Montero de Espinosa, *IEEE Int. Ultrason. Symp.* **2**, 1282 (2004).
17. S. T. Hansen, F. L. Degertekin, and B. T. Khuri-Yakub, *Proc. SPIE* **3586**, 310 (1999).
18. T. E. G. Álvarez-Arenas, *Sensors* **13**, 5996 (2013).
19. X. L. Deán-Ben, G. A. Pang, F. Montero de Espinosa, and D. Razansky, *Appl. Phys. Lett.* **107**, 051105 (2015).
20. E. Bay, A. Douplik, and D. Razansky, *Lasers Med. Sci.* **29**, 1029 (2014).
21. T. E. Gomez and F. Montero de Espinosa, *IEEE Ultrason. Symp.* **2**, 1069 (2000).

**INTEGRATED CATHETER FOR SIMULTANEOUS RADIO
FREQUENCY ABLATION AND OPTOACOUSTIC MONITORING OF
LESION PROGRESSION [2]**

Peer-reviewed Journal Paper

Autors: Johannes Rebling^{1,2,†}, Francisco Javier Oyaga Landa^{1,2,†}, Xosé Luís Deán-Ben¹, Alexandre Douplik³, and Daniel Razansky^{1,2,*}

Affiliations:

¹Institute for Biological and Medical Imaging (IBMI), Helmholtz Center Munich, Neuherberg, Germany

²School of Medicine, Technical University of Munich, Germany

³Department of Physics, Ryerson University, 350 Victoria Street, Toronto, Ontario M5B 2K3, Canada

*Corresponding author. ; †These authors contributed equally to this work.

In: Optics Letters Vol. 43, Issue 8, pp. 1886-1889 (2018).

Abstract: Electrosurgery, is a frequently used treatment for many cardiac arrhythmias. Electrophysiological and anatomic mapping, as well as careful radiofrequency power control typically guide the radiofrequency ablation procedure. Accurate monitoring of the lesion formation with sufficient spatio-temporal resolution is currently a challenge. We present a novel integrated catheter; the design combines the delivery of both electric current and optoacoustic excitation beam in a single catheter consisting of copper-coated multimode light-guides and its manufacturing is described in detail. The electrical current causes coagulation and desiccation while the excitation light is locally absorbed, generating OA responses from the entire ex-vivo bovine tissue treated volume with a volumetric frame rate of 10 Hz over 150 seconds.

Contribution of thesis author: Laboratory measurements, processing algorithms, signal analysis and computer-aided results and methods.

Copyright Notice: Copyright © 2018, OSA Publishing, The Optical Society, Optics Letters.

Optics Letters

Integrated catheter for simultaneous radio frequency ablation and optoacoustic monitoring of lesion progression

JOHANNES REBLING,^{1,2,†} FRANCISCO JAVIER OYAGA LANDA,^{1,2,†} XOSÉ LUÍS DEÁN-BEN,¹
ALEXANDRE DOUPLIK,³ AND DANIEL RAZANSKY^{1,2,*}

¹Institute of Biological and Medical Imaging (IBMI), Helmholtz Center Munich, Ingolstaedter Landstraße 1, D-85764 Neuherberg, Germany

²School of Medicine and School of Bioengineering, Technical University of Munich, Germany

³Department of Physics, Ryerson University, 350 Victoria Street, Toronto, Ontario M5B 2K3, Canada

*Corresponding author: dr@tum.de

Received 22 January 2018; revised 27 February 2018; accepted 3 March 2018; posted 5 March 2018 (Doc. ID 319854); published 0 MONTH 0000

Radio frequency (RF) catheter ablation is commonly used to eliminate dysfunctional cardiac tissue by heating via an alternating current. Clinical outcomes are highly dependent on careful anatomical guidance, electrophysiological mapping, and careful RF power titration during the procedure. Yet, current treatments rely mainly on the expertise of the surgeon to assess lesion formation, causing large variabilities in the success rate. We present an integrated catheter design suitable for simultaneous RF ablation and real-time optoacoustic monitoring of the forming lesion. The catheter design utilizes copper-coated multimode light guides capable of delivering both ablation current and near-infrared pulsed-laser illumination to the target tissue. The generated optoacoustic responses were used to visualize the ablation lesion formation in an *ex-vivo* bovine heart specimen in 3D. The presented catheter design enables the monitoring of ablation lesions with high spatiotemporal resolution while the overall therapy-monitoring approach remains compatible with commercially available catheter designs.

Published by The Optical Society under the terms of the [Creative Commons Attribution 4.0 License](#). Further distribution of this work must maintain attribution to the author(s) and the published article's title, journal citation, and DOI.

OCIS codes: (170.1020) Ablation of tissue; (170.5120) Photoacoustic imaging; (170.6935) Tissue characterization.

<https://doi.org/10.1364/OL.99.099999>

Radio frequency catheter ablation (RFCA) is used for coagulation and destruction of dysfunctional tissues in the fields of oncology [1], cardiology [2], dermatology [3], and vascular diseases [4]. One common application in cardiology is the elimination of abnormal electrical pathways responsible for cardiac arrhythmias [2], particularly those shown to be resistant to drug therapy [5]. Much like other thermal ablation procedures,

RFCA results in localized coagulation and desiccation of the target tissue while avoiding uncontrolled damage to neighboring structures. The ablation procedure is generally guided by electrophysiological and anatomic mapping as well as by careful radio frequency (RF) power titration [6]. The size of the induced lesion is mainly determined by the extent and duration of the heat-affected area. Hence, real-time treatment monitoring is essential to optimize the outcome of the intervention. The ablation process is usually monitored via simple temperature or impedance measurements at the ablation tip [7,8]. However, heat diffusion and the use of irrigated ablation tips can substantially affect the size and shape of the heated area, resulting in failed treatments [9]. To this end, several imaging techniques have been proposed for ablation monitoring. For example, intravascular ultrasound (IVUS) and magnetic resonance imaging (MRI) allowed for a more precise placement and navigation of the ablation catheter and visualization of the RFCA-induced morphological tissue alterations [10]. Transformations of the tissue composition in coagulated or desiccated areas result in light scattering and absorption changes detectable via optical methods, such as spectroscopy or optical coherence tomography (OCT) [11]. Infrared thermal imaging furthermore allows the quantification of tissue temperature with high resolution, but is restricted to superficial tissues [12]. Ultrasound (US), x-ray computed tomography (CT), or MRI images were shown sensitive to temperature variations in the tissue; however, real-time mapping of lesion formation is impeded with these techniques due to either limited temporal resolution or low contrast [13].

Optoacoustics (OA) has been suggested for ablation monitoring as early as 1993 [14], chiefly owing to its high sensitivity to changes in optical properties resulting from chemical transformations in ablated tissues [15] and to temperature variations [16]. OA has been used for temperature monitoring in forming lesions [17] and recently adopted for volumetric tomographic ablation monitoring in real time [18]. Volumetric OA tomography has also been shown to clearly discern vascular and organ morphology as well as extrinsically labeled structures

in vivo [19], making it highly suitable for precise anatomical navigation. The high imaging speed of state-of-the-art OA tomography is efficient in capturing the dynamics of RFCA treatments with subsecond temporal resolution in two [15] and three dimensions [18]. However, in previous studies the excitation light was delivered into the ablated area through thick layers of turbid tissues, limiting applicability in realistic clinical scenarios involving monitoring of deep tissue lesions [20].

Herein, we present a conceptually different approach for simultaneous RF ablation and OA monitoring (RAOM) of the lesion formation. It combines the delivery of both electrical current and pulsed light within a single catheter (Fig. 1) while detection of the generated OA responses is performed from outside the body using a spherical matrix array for optimal volumetric OA image formation. The integrated catheter consists of a bundle of 96 copper-coated multimode fibers [Fig. 1(a)]. The excitation light and electrical current are coupled into the proximal end of the bundle [Fig. 1(b)] and are delivered to the tissue at its distal end [Fig. 1(c)]. The individual, custom-made light guides consist of step-index multimode optical fibers with a silica core and a fluorine-doped glass cladding, enabling efficient propagation of visible and near-infrared light with a transmission efficiency of approximately 30%. The fibers have a core diameter of 200 μm (220 μm including cladding) and a numerical aperture (NA) of 0.2. The light guides are further coated with a 25 μm thin copper film [Fig. 1(d)]. The copper coating was removed at the proximal end of the bundle to maximize light coupling efficiency. This was achieved by closely packing the fibers within a conventional optical fiber connector (inner diameter 2.5 mm, SMA905, Thorlabs, Newton, USA) and securing them using a high-temperature epoxy (353NDPK, Thorlabs, Newton, USA). After the epoxy was cured, the proximal end was polished to optical quality. Figure 1(b) shows the facet of the polished proximal. A low-resistance electrical connection between the separate copper-coated light guides was achieved

using solder in the vicinity of the proximal end. Additionally, a copper cable was soldered to the same location, enabling the connection to the RF generator. The copper-coated light guides align to each other in a nearly hexagonal pattern ensuring an even distribution of the ablation current at the distal tip. The bundle was embedded into a steel ferule with an outer diameter of 6 mm and an inner aperture of 4 mm using high-temperature epoxy and polished to optical quality. The minimal short-term bending radius of the copper-coated fibers was experimentally found to be 2 mm, comparable to conventional 200 μm fibers, while the bending radius of the assembled bundle was less than 8 mm. Figure 1(c) shows the polished facet of the distal end with and without light transmitted through the catheter. The assembled RAOM catheter [Fig. 1(d)] was electrically insulated using PVC tubing (Tygon, Carl Roth GmbH, Karlsruhe, Germany), only exposing the ablation tip at the distal end. A schematic of the simultaneous RF ablation and OA signal detection experiment is shown in Fig. 1(e). The ultrasound array consists of 256 detection elements distributed on a spherical cap with 90° apex angle (0.59π solid angle) and 4 cm radius. Its individual elements have a central frequency of 4 MHz and 100% detection bandwidth, resulting in nearly isotropic 3D imaging resolution of ~ 200 μm around the geometrical center of the sphere. OA signal excitation was achieved via an optical-parametric-oscillator-(OPO)-based laser (Innolas Laser GmbH, Krailling, Germany) coupled into the proximal end of the RAOM catheter. The distal end of the catheter delivered short (< 10 ns) laser pulses with ~ 6 mJ energy and pulse repetition rate of 10 Hz, resulting in light fluence of ~ 48 mJ/cm² at the fiber tip. The wavelength of the laser was tuned to 780 nm, corresponding to the highest lesion-specific OA contrast [18]. The 256 detection channels were simultaneously digitized at 40 megasamples per second by a custom-made data acquisition system (Falkestein Mikrosysteme GmbH, Taufkirchen, Germany) triggered by the Q-switch output of the laser. The same trigger signal was used to switch off the RF current during the OA signal acquisition to avoid signal cross-talk. The acquired signals were deconvolved with the impulse response of the matrix array elements and bandpass filtered between 0.1 and 2 MHz to smoothen the images. The reconstructions were performed with a graphics-processing-unit-based 3D back-projection algorithm [21,22].

Performance of the RAOM catheter was first separately characterized in the OA imaging and RF ablation modes. For OA imaging, we used a two-layer agarose phantom [Fig. 2(a)]. The first layer mimicked strong tissue scattering and was used to quantify the OA signal levels generated by the catheter tip due to back-scattered light. It consisted of a 3 mm thick layer of agarose mixed with 1.2% (by volume) of Intralipid. The second 1.5 mm thick layer of the phantom mimicked tissue optical absorption of $\mu_a = 0.66$ cm⁻¹ at 780 nm [23] and comprised agarose mixed with ink. The distal end of the catheter was positioned in direct contact with the scattering layer of the phantom, and OA imaging was performed without RF ablation. Figure 2(b) displays the side view of the recorded volumetric OA image where the absorbing layer is clearly visible at a depth of 3 mm in the phantom (P). Part of the light emitted by the catheter is back-scattered toward the ablation tip where it is absorbed by both the copper surrounding the light guides as well as the steel ferule [see Fig. 1(a)]. The signal generated at the catheter tip (C) is, however, much weaker in comparison

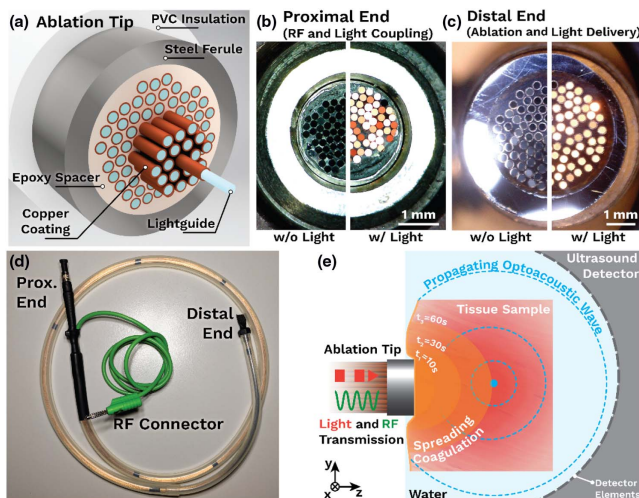


Fig. 1. Design and application of the combined RAOM catheter. (a) The catheter ablation tip, comprising copper-coated light guides embedded in a steel ferule using high-temperature epoxy. (b) Proximal end facet of the catheter, optimized for high light coupling efficiency. (c) Distal end facet of the catheter, delivering both RF current and pulsed-light illumination. (d) Fully assembled bundle. (e) Layout of the combined RAOM monitoring experiment.

F1:1
F1:2
F1:3
F1:4
F1:5
F1:6
F1:7

119
120
121
122
123
124
125
126
127
128
129
130
131
132
133
134
135
136
137
138
139
140
141
142
143
144
145
146
147
148
149
150
151
152
153
154
155
156
157
158
159
160
161
162
163
164
165
166
167
168
169
170
171
172
173
174
175
176
177
178
179

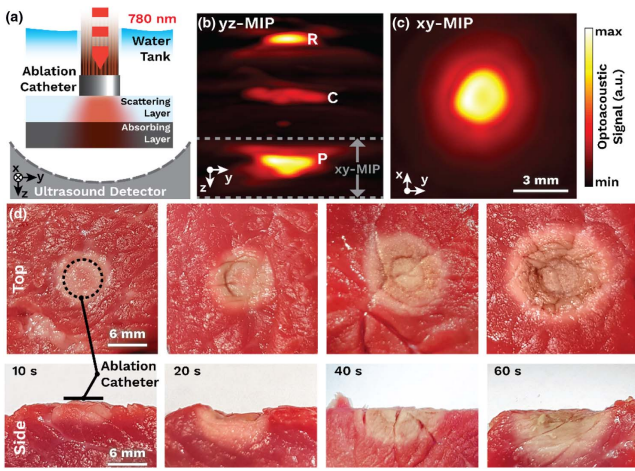


Fig. 2. Characterization of the RFOA catheter in standalone OA imaging and RF ablation modes. (a) Experimental arrangement for OA imaging with the catheter placed in direct contact with a scattering and absorbing phantom. (b) Reconstructed volumetric OA images of the phantom containing signals generated by the absorbing layer (P) and the catheter tip (C) as well as the signal reflected by the catheter tip (R). Maximal intensity projection (MIP) along the x direction is shown. (c) The corresponding MIP image made along the depth (z) direction over the range indicated by the gray-dashed lines in panel (b). (e) Top- and side-view photographs of lesions generated in porcine heart tissue.

F2:1
F2:2
F2:3
F2:4
F2:5
F2:6
F2:7
F2:8
F2:9
F2:10
F2:11

with 20 cm² area was positioned under the tissue. The catheter delivered tone bursts of electric current at 20 kHz carrier frequency with a duty cycle of 3% (600 cycles in a burst, 10 Hz repetition frequency). On average, 9 W of electric power was delivered for 10 s, 20 s, 40 s, and 60 s into the tissue samples. Photographs of the generated lesions are shown in Fig. 2(d). The catheter formed a homogenous white coagulum having a typical pallor and a small depression due to desiccation without any visible charring. Longer ablation durations generated deeper lesions, reaching a maximal depth of ~1 cm after 60 s. The tissue beyond the coagulation region appears unaffected in all four tissue samples. The uniform lesion shape indicates a homogenous current distribution due to the evenly distributed copper-coated light guides.

194
195
196
197
198
199
200
201
202
203
204
205
206
207
208
209
210
211
212
213
214
215
216
217
218
219
220
221
222
223
224
225
226
227
228
229
230
231
232
233
234
235
236

The real-time ablation monitoring performance was then evaluated in a 4 cm thick porcine tissue sample, which was placed between the RAOM catheter and the surface of the spherical detection array. Ablation was carried out for 30 s, and OA signals were acquired for 180 s to cover the cooling period. Light fluence decay was volumetrically corrected by dividing the reconstructed volumetric image with the solution of the light diffusion equation for a point source, i.e., a 3D exponential decay in the form of $(1/d) \exp(-\mu_{\text{eff}}d)$, where $\mu_{\text{eff}} = 3 \text{ cm}^{-1}$ is the effective attenuation coefficient and d is the distance in centimeters between the corrected voxel and the distal end of the fiber bundle. For distances d smaller than the radius of the ablation tip, the fluence was assumed to be constant. This particular correction function was applied as a purely qualitative measure aimed at achieving better contrast uniformity across the OA images.

Figure 3 displays OA images of the porcine tissue sample prior [Fig. 3(a)], during [Fig. 3(b)] and after [Fig. 3(c)] the RF ablation procedure together with an OA signal time trace of a coagulated and a noncoagulated voxel [Fig. 3(d)]. As expected, the lowest OA signal intensity appears prior to the ablation due to the lowest temperature in the sample and lack of coagulation. A strong increase in the OA signal amplitude can be observed as the lesion progresses [Fig. 3(b), first 30 s in Fig. 3(d)]. The signal increase is attributed to the enhanced lesion contrast associated to tissue coagulation [15] as well as to the strong temperature dependence of the Grüneisen parameter in tissues [16]. While previously suggested approaches were afflicted by strong light attenuation in deep tissues thereby

224
225
226
227
228
229
230
231
232
233
234
235
236

to that generated by the tissue-mimicking absorbing layer. The catheter tip also acts as a partial acoustic reflector of the omnidirectional OA signals generated in the phantom. This results in shadow signals detected by the transducer (R). However, these artifacts do not interfere with the signals originating from the region of interest and can easily be cropped. The top view of the volumetric OA image shown in Fig. 2(c) further illustrates the uniform illumination provided by the RAOM catheter. Ablation performance of the RAOM catheter was subsequently evaluated by generating lesions in a porcine heart tissue sample. The catheter was connected to a custom-built generator allowing precise control of the output RF power. The samples were immersed in phosphate-buffered saline (PBS, Sigma Aldrich, St. Louis, USA) and the ground electrode

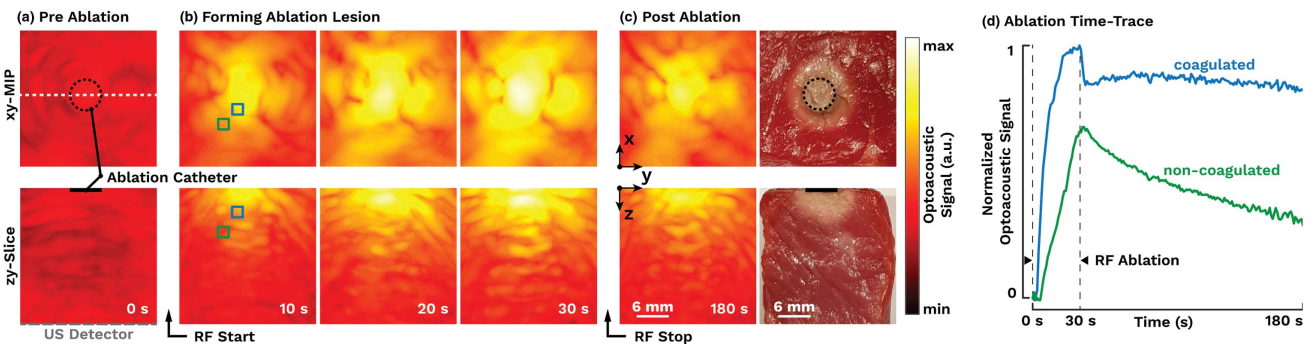


Fig. 3. Real-time OA monitoring of RF ablation in *ex-vivo* porcine heart tissue. (a) OA images acquired from unablated tissue. (b) Noninvasive OA imaging of the lesion formation in 3D. (c) OA image acquired after the cooldown phase along with the photograph of coagulated area from a sliced specimen. Images on the top are top-view MIPs while the bottom row shows a single (z - y) slice through the center of the reconstructed OA volumes, as indicated by the white-dashed line in (a). (d) Time evolution of the OA signal during and after RF ablation in the locations indicated in panel (b).

F3:1
F3:2
F3:3
F3:4
F3:5

necessitating signal averaging [15], direct delivery of the excitation light into the ablated region via the catheter-based approach allows for monitoring of lesion without signal averaging. This represents a significant advantage of the integrated RAOM method for real-time clinical application. In Fig. 3(c) the OA images are further compared to gross pathology of the specimen taken after the RF ablation experiment, confirming a uniform coagulum without charring and a good qualitative correspondence between the yellow colored volume in the OA images and the appearance of coagulated area in the sliced specimen. As expected, cooler tissue [Figs. 3(c) and 3(d), $t = 180$ s] exhibits lower OA signal levels as compared to the end of ablation time point ($t = 30$ s), this is attributed to the temperature dependence of the OA signals [16]. The OA signal levels at $t = 180$ s remain higher than in the pre-ablated specimen, supposedly due to incomplete cooldown and residual thermal diffusion effects in the rest of the sample. Note, however, that the signal in the coagulated zone [blue square in Fig. 3(b)] does not decline significantly during the cooldown period [blue plot in Fig. 3(d)]; this is ascribed to an increase in optical absorption coefficient caused by denatured tissue proteins in the coagulum [17].

The presented results illustrate the basic feasibility of the suggested integrated RAOM approach for simultaneous RF ablation and real-time OA monitoring of the lesion progression. Because of direct light delivery through the catheter, the ablated region is efficiently illuminated, thus enabling monitoring of deep-seated lesions. Evidently, *in vivo* experimentation is essential to demonstrate the applicability of the proposed monitoring configuration in a real clinical setting. For this, several outstanding technical issues need also to be addressed. The ablation tip diameter of 6 mm is to be reduced to the typical 4 mm electrodes used in RFCA; this can be achieved by reducing the size of the encapsulating steel ferrule, packing the copper-coated fibers more densely, and/or reducing the number of fibers, the last also resulting in a more flexible catheter design. This would allow for the integration of the RAOM catheter into conventional steerable catheter shafts, thus adding additional functionality, such as electrocardiographic and temperature monitoring at the tip. Both the ablation catheter and its tip could be further adapted to fit different types of ablation procedures. For instance, RF tumor ablation is regularly performed with large-area ablation catheters, achievable by using a longer steel ferrule at the ablation tip of the RAOM catheter [24]. The presented results indicate the basic feasibility of identifying changes related to tissue heating and coagulation with the suggested RAOM approach, making its potential combination with existing catheter and monitoring modalities simple and cost-effective. We observed dynamic changes in the OA images of forming RF lesions that corresponded well with the gross lesion pathology. However, the observed changes in the OA signal allow for only a qualitative assessment of the forming lesion, as the method does not allow for differentiating between alterations in the optical absorption due to coagulation versus changes of the temperature-dependent Grüneisen parameter. This can be possibly achieved via a multi-spectral imaging approach [25], thus attaining both real-time and quantitative feedback on the temperature distribution and the size of coagulated area during the intervention. Yet, real-time temperature mapping may still be possible in uncoagulated tissue areas where no alterations of the optical tissue properties have occurred [25].

In conclusion, the suggested catheter combining RF ablation and light delivery for OA excitation in a single flexible and adaptable design represents an advantageous solution for optimizing the outcome of RFCA interventions. The high spatiotemporal resolution and deep-tissue imaging capacity of the integrated ablation monitoring approach anticipate its general applicability in a number of RF ablation procedures.

Funding. Deutsche Forschungsgemeinschaft (DFG) (RA 1848/5-1); Seventh Framework Programme (FP7) (317526).

[†]These authors contributed equally to this paper.

REFERENCES

- M. Pai, N. Habib, H. Senturk, S. Lakhtakia, N. Reddy, V. R. Ciccinnati, I. Kaba, S. Beckebaum, P. Drymouisis, M. Kahaleh, and W. Brugge, *World J. Gastrointest. Surg.* **7**, 52 (2015).
- C. T. January, S. L. Wann, J. S. Alpert, H. Calkins, J. E. Cigarroa, J. C. Cleveland, J. B. Conti, P. T. Ellinor, M. D. Ezekowitz, M. E. Field, K. T. Murray, R. L. Sacco, W. G. Stevenson, P. J. Tchou, C. M. Tracy, and C. W. Yancy, *Circulation* **130**, 2071 (2014).
- S. S. Yu, W. D. Tope, and R. C. Grekin, *Dermatol. Surg.* **31**, 932 (2005).
- C. Pappone, S. Rosanio, G. Oreto, M. Tocchi, F. Gugliotta, G. Vicedomini, A. Salvati, C. Dicandia, P. Mazzone, V. Santinelli, S. Gulletta, and S. Chierchia, *Circulation* **102**, 2619 (2000).
- T. Terasawa, E. M. Balk, and M. Chung, *Comp. Effect. Rev.* **15** (2009).
- M. Haïssaguerre, P. Jaïs, D. C. Shah, S. Garrigue, A. Takahashi, T. Lavergne, M. Hocini, J. Peng, R. Roudaut, and J. Clémenty, *Circulation* **101**, 1409 (2000).
- M. Harvey, Y. Kim, J. Souse, R. El-Atassi, F. Morady, H. Calkins, and J. Langberg, *Pacing Clin. Electrophysiol.* **15**, 22 (1992).
- H. Calkins, E. Prystowsky, M. Carlson, L. S. Klein, J. P. Saul, and P. Gillette, *Circulation* **90**, 1279 (1994).
- Z. Liu, M. Ahmed, Y. Weinstein, and M. Yi, *Int. J. Hyperthermia* **22**, 327 (2006).
- C. J. McGann, E. G. Kholmovski, R. S. Oakes, J. Blauer, M. Daccarett, N. Segerson, K. J. Airey, N. Akoum, E. Fish, T. J. Badger, E. DiBella, D. Parker, R. S. MacLeod, and N. F. Marrouche, *J. Am. Coll. Cardiol.* **52**, 1263 (2008).
- D. Herranz, J. Lloret, S. Jiménez-Valero, and E. Margallo-Balbás, *Biomed. Opt. Express* **6**, 3268 (2015).
- M. Wood, S. Goldberg, M. Lau, and A. Goel, *Circ. Arrhythm. Electrophysiol.* **4**, 373 (2011).
- C. Y. Wang, X. Geng, T. S. Yeh, H. L. Liu, and P. H. Tsui, *Med. Phys.* **40**, 72901 (2013).
- R. O. Esenaliev, A. A. Oraevsky, V. S. Letokhov, A. A. Karabutov, and T. V. Malinsky, *Laser Surg. Med.* **13**, 470 (1993).
- N. Dana, L. Di Biase, A. Natale, S. Emelianov, and R. Bouchard, *Heart Rhythm* **11**, 150 (2014).
- I. V. Larina, K. V. Larin, and R. O. Esenaliev, *J. Phys. D* **38**, 2633 (2005).
- K. V. Larin, I. V. Larina, and R. O. Esenaliev, *J. Phys. D* **38**, 2645 (2005).
- G. Pang, Y. Erwin, L. Dean-Ben, and D. Razansky, *J. Cardiovasc. Electrophysiol.* **26**, 339 (2015).
- X. L. Dean-Ben, S. Gottschalk, B. Mc Larney, S. Shoham, and D. Razansky, *Chem. Soc. Rev.* **46**, 2158 (2017).
- T. Mitcham, K. Dextraze, H. Taghavi, M. Melancon, and R. Bouchard, *Photoacoustics* **3**, 45 (2015).
- X. L. Dean-Ben and D. Razansky, *Photoacoustics* **1**, 68 (2013).
- X. L. Dean-Ben, A. Ozbek, and D. Razansky, *IEEE Trans. Med. Imaging* **32**, 2050 (2013).
- S. L. Jacques, *Phys. Med. Biol.* **58**, R37 (2013).
- S. N. Goldberg, *Eur. J. Ultrasound* **13**, 129 (2001).
- D. Razansky, *IEEE J. Sel. Top. Quantum Electron.* **18**, 1234 (2012).

VOLUMETRIC OPTOACOUSTIC TEMPERATURE MAPPING IN PHOTOTHERMAL THERAPY [3]

Peer-reviewed Journal Paper

Autors: Francisco Javier Oyaga Landa^{1,2}, Xosé Luís Deán-Ben¹, Ronald Sroka³, and Daniel Razansky^{1,2,*}

Affiliations:

¹Institute for Biological and Medical Imaging (IBMI), Helmholtz Center Munich, Neuherberg, Germany

²Faculty of Medicine, Technical University of Munich, Germany

³Laser Research Laboratory / LIFE Center, Ludwig-Maximilian-University, Munich, Germany

*Corresponding author.


In: Scientific Reports 7, Article number: 9695 (2017).

Abstract: Photoablative laser therapy is in common use for selective destruction of malignant masses, vascular and brain abnormalities. Tissue ablation and coagulation are irreversible processes occurring shortly after crossing a certain thermal exposure threshold. As a result, accurate mapping of the temperature field is essential for optimizing the outcome of these clinical interventions. Here we demonstrate four-dimensional optoacoustic temperature mapping of the entire photoablated region. Accuracy of the method is investigated in tissue-mimicking phantom experiments. Deviations of the volumetric optoacoustic temperature readings provided at 40ms intervals remained below 10% for temperature elevations above 3°C, as validated by simultaneous thermocouple measurements. The excellent spatio-temporal resolution of the new temperature monitoring approach aims at improving safety and efficacy of laser-based photothermal procedures.

Contribution of thesis author: Study design, laboratory measurements, processing algorithms, signal analysis and computer-aided results and methods.

Copyright Notice: Copyright © 2018, Nature Publishing Group, Springer Nature, Scientific Reports.

SCIENTIFIC REPORTS



OPEN

Volumetric Optoacoustic Temperature Mapping in Photothermal Therapy

Francisco Javier Oyaga Landa^{1,2}, Xosé Luís Deán-Ben¹, Ronald Sroka³ & Daniel Razansky^{1,2}

Photothermal therapy and ablation are commonplace medical procedures employed for treatment of tumors, vascular and brain abnormalities as well as other disorders that require selective destruction of tissues. Yet, accurate mapping of the dynamic temperature field distribution in the treated region represents an unmet clinical need, strongly affecting the clinical outcome of these interventions. We introduce a fast three-dimensional temperature mapping method based on real-time optoacoustic sensing of the treated region coupled with a thermal-diffusion-based model of heat distribution in tissues. Deviations of the optoacoustic temperature readings provided at 40 ms intervals remained below 10% in tissue-mimicking phantom experiments for temperature elevations above 3 °C, as validated by simultaneous thermocouple measurements. Performance of the new method to dynamically estimate the volumetric temperature distribution was further showcased in *post-mortem* mouse imaging experiments. The newly discovered capacity to non-invasively measure the temperature map in an entire treated volume with both high spatial and temporal resolutions holds potential for improving safety and efficacy of light-based therapeutic interventions.

Thermal therapies are widely employed in clinical practice, from selective ablation of cancerous tissues, benign hyperplasias and varicose veins to elimination of subcutaneous fat, cardiac arrhythmias and enhanced drug delivery^{1–6}. Several sources have been considered for the heating purposes, among them laser light, focused ultrasound, radio-frequency current and microwaves². Laser-induced thermotherapy (LITT), also referred to as laser ablation, has gained popularity due to its important advantages, such as minimal invasiveness, low hardware costs and reduced treatment time^{3,4}. LITT employs laser radiation as an energy source, often guided through optical fibers to the target tissue as e.g. in percutaneous laser ablation (PLA) or endovenous laser therapy (ELT). In addition, light-absorbing agents are often used to target photothermal procedures and further serve as theranostic agents^{5–7}. For example, semiconducting polymer nanobioconjugates have been recently suggested as theranostic amplifiers for combined optoacoustic (OA) imaging and photothermal therapy⁸ as well as for targeted photothermal activation of neurons⁹.

Both the temporal and the spatial temperature distribution in the treated tissue play a crucial role in the outcome of photothermal interventions. Heat-driven denaturation is generally facilitated when tissues are heated above 50 °C, while the exposure time further determines the size of the induced lesion. Yet, several therapeutic procedures use lower temperature elevations without inducing irreversible tissue damage, including local and whole-body hyperthermia¹⁰ as well as low- and medium-intensity focused ultrasound^{11,12}. The effectiveness of thermal therapies thus heavily relies on the ability to closely monitor and control the volumetric temperature distribution of the treated tissues in real time². Invasive approaches based on thermocouples or fiber-optic sensors¹³ can be used for temperature monitoring. In this way, the temperature can only be captured in a few locations within the heated region while a direct tissue contact or an invasive approach are further required. On the other hand, the temperature map can in principle be obtained using non-invasive imaging modalities such as optical methods^{14,15}, infrared thermometry¹⁶, ultrasound¹⁷, x-ray computed tomography (CT)¹⁸, or magnetic resonance imaging (MRI)¹⁹. However, these techniques are either limited by low penetration, sensitivity, contrast or otherwise lack an adequate temporal resolution for dynamic mapping of the temperature fields.

¹Institute for Biological and Medical Imaging (IBMI), Helmholtz Center Munich, Neuherberg, Germany. ²Faculty of Medicine, Technical University of Munich, Munich, Germany. ³Laser Research Laboratory/LIFE Center, Ludwig-Maximilians-University, Munich, Germany. Correspondence and requests for materials should be addressed to D.R. (email: dr@tum.de)

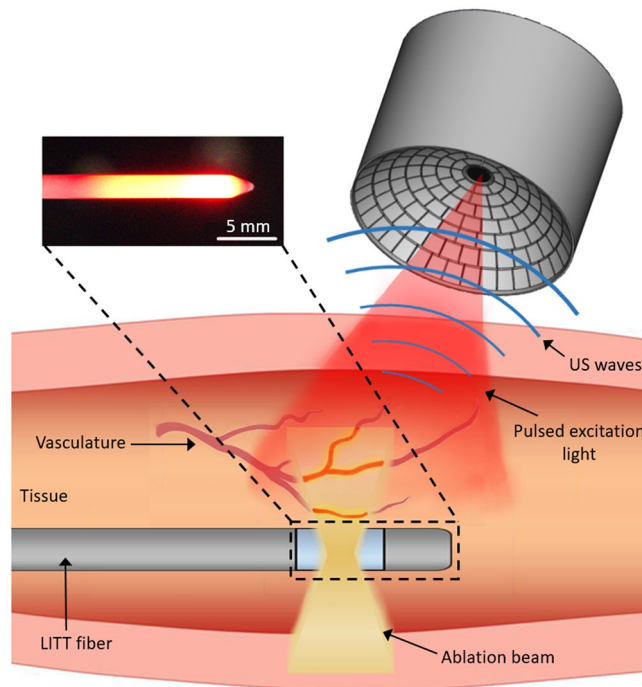


Figure 1. Lay-out of the experimental setup. The drawings of the transducer array and the ablation system were developed by the authors.

OA imaging may potentially represent an advantageous approach for monitoring phototherapy due to its high sensitivity to temperature variations^{20–24}. The temperature dependence of the OA signal during thermal therapies has been previously established^{25–28}. Yet, no three-dimensional (3D) mapping of the temperature field in real time has been so far demonstrated. Herein, we study the application of optoacoustics to map the temperature distribution during laser-induced thermal therapy. In particular, evolution of volumetric OA data is correlated with thermocouple readings in controlled tissue-mimicking phantom experiments in order to establish the lower boundaries on the accuracy of the temperature estimations. A thermal-diffusion-based model of heat distribution in tissues is further employed in order to render the spatio-temporal distribution of the temperature field in experiments performed in highly heterogeneous mouse tissues.

Methods

Optoacoustic data acquisition set-up and image reconstruction. The lay-out of the experimental setup is shown in Fig. 1. Briefly, heating was induced using a diode laser generating 20 W of continuous wave power at a wavelength of 830 nm (Indigo 830, Indigo Medical Inc., Lawrenceville, New Jersey). A specialized fiberoptic delivery system with a cylindrical diffuser at the tip was used to guide the ablation beam to the region of interest. Volumetric temperature monitoring was performed with a 3D OA imaging system consisting of a 512-element spherical transducer array covering an angle 140° with 4 cm radius of curvature (1.3π solid angle). The individual elements of the array have a central frequency of 5 MHz and $\sim 100\%$ detection bandwidth, corresponding to nearly isotropic imaging resolution of $\sim 150 \mu\text{m}$ around the geometrical center of the sphere. Acoustic coupling was ensured by molding agarose gel between the active surface and the surface of the imaged sample (Fig. 1). OA responses were excited with a short-pulsed (~ 8 ns) laser source (Innolas Laser GmbH, Krailling, Germany) guided via a custom-made fiber bundle (CeramOptec GmbH, Bonn, Germany) through a hollow cylindrical cavity in the center of the array. For imaging, the wavelength of the tunable optoacoustic laser source was also set to 830 nm and the optical fluence was approximately 11 mJ/cm^2 at the surface of the imaged sample. The pulse repetition frequency (PRF) of the laser was set to 5 Hz. A second arm of the fiber bundle was guided to a Coherent powermeter EM-USB-J-25MB-LE (Coherent Inc., Santa Clara, California) to monitor the energy per pulse, which was used to normalize the acquired signals. All 512 OA signals were simultaneously digitized at 40 mega-samples per second (MSPS) by a custom-made data acquisition (DAQ) system (Falkenstein Mikrosysteme GmbH, Taufkirchen, Germany) triggered with the Q-switch output of the laser.

OA images were subsequently reconstructed with a graphics processing unit (GPU)-based 3D back-projection algorithm²⁹. Prior to reconstruction, the acquired signals were deconvolved with the impulse response of the array elements and band-pass filtered between 0.1 MHz and 7 MHz.

Temperature Estimation Method. Our OA temperature estimation is based on the temperature dependence of the thermoelastic conversion efficiency. When the OA signals are excited with a short-duration laser pulse, the so-called stress-confinement conditions can be assumed for the initial OA signal (pressure) distribution p_0 in the medium³⁰. In this case, the latter is given via $p_0 = \Gamma \mu_a \Phi$, being Γ the (dimensionless) Grüneisen

parameter, μ_a the optical absorption coefficient and Φ the light fluence. The temperature dependence of the generated OA signals mainly comes from variations in the Grüneisen parameter, whose dependence on temperature in water-like aqueous solutions can be approximated by³⁰

$$\Gamma(T) = 0.0043 + 0.0053T, \quad (1)$$

where T is expressed in °C. Eq. (1) describes temperature dependence of the Grüneisen parameter for water and diluted aqueous solutions, which was verified with empirical measurements across a wide range of temperatures³¹. The relative change of the OA signal as a function of the temperature increase ΔT can be then expressed as

$$\frac{\Delta p_0}{p_{0,0}} = \frac{0.0053 \Delta T}{0.0043 + 0.0053T_0}, \quad (2)$$

being $p_{0,0}$ and T_0 the initial (baseline) optoacoustic signal and the initial temperature before the ablation experiment, respectively. According to Eq. 2, the amplitude of the OA signals is expected to increase by approximately 2.7% per degree for typical temperature values of 36°C in living organisms. We further define F as the ratio between the relative increment of the OA signal and the relative increment of temperature, i.e.,

$$F = \frac{T_0}{p_{0,0} \Delta T} \Delta p_0 \quad (3)$$

Considering Eq. 2, the theoretical value of F (F_{th}) can be expressed as a function of the initial temperature T_0 via

$$F_{th} = \left(\frac{0.8113}{T_0} + 1 \right)^{-1} \quad (4)$$

The temperature increment can then be estimated from the relative OA signal increase as

$$\Delta T = \frac{T_0}{p_{0,0} F_{th}} \Delta p_0 \quad (5)$$

It should be noted that, unlike for inorganic liquids, protein denaturation and coagulation processes are known to take place in soft biological tissues for temperatures exceeding 50°C, introducing significant additional complexity due to non-linear alterations of the Grüneisen parameter²⁶ as well as alterations in the optical absorption and scattering coefficient of the ablated tissues³². Accuracy of the above temperature estimation approach is therefore expected to be limited to the temperatures range lying below the coagulation threshold.

Phantom validation experiments. The quantitative performance of the temperature monitoring method according to Eq. 5 was experimentally tested in a tissue-mimicking phantom. The phantom consisted of three tubings with 1 mm diameter and 10 mm length embedded in a ~8 mm thick layer of chicken breast. The tubings were filled with murine blood and sealed with glue. Three thermocouples (Physitemp Instruments Inc., Clifton, New Jersey) were inserted into the tubings to provide real-time temperature values. The thermocouple readings were digitized with an embedded NI 9213 DAQ (National Instruments Corporation, Austin, Texas, U.S.). For each tubing, the temperature was estimated from the OA signal in an ROI corresponding to the exactly known location of each thermocouple.

The Thermal Diffusion Model. High resolution temperature mapping in real highly heterogeneous tissues represents a much more challenging task than pointwise temperature estimations. This is chiefly because the temperature elevation due to laser-induced heating depends on both the local light fluence distribution and the optical absorption coefficient. As a result, a highly non-uniform temperature distribution is expected to occur in heterogeneous tissues with many locations exhibiting low absorption or otherwise insignificant temperature alterations that cannot be accurately estimated by optoacoustics. We therefore assumed that only voxels that generated OA signals above a certain threshold, set to 20% of the maximum signal in the entire 3D image volume, can be effectively used for reliable temperature estimations, whereas the remaining voxels are assumed to be mainly affected by heat diffusion from the adjacent voxels exhibiting higher absorption values. A model based on the heat diffusion equation has been thus introduced to dynamically estimate the volumetric temperature distribution via³³

$$\frac{\partial T(r, t)}{\partial t} - D \nabla^2 T(r, t) = \frac{Q(r, t)}{\rho C_p}, \quad (6)$$

where $T(r, t)$ is the spatio-temporal map of the temperature increase, $Q(r, t)$ is the heat absorbed in the tissue per unit volume and unit time, ρ is the tissue mass density, C_p is its specific heat capacity per unit mass, and $D = k / \rho C_p$ is the thermal diffusivity, being k the thermal conductivity in [W/m °C]. We assumed $\rho = 1.06 \text{ g/ml}$, $C_p = 3.5 \text{ J/gK}$, $D = 1.14 \cdot 10^{-7} \text{ m}^2/\text{s}$ for soft biological tissues³³. The Green's solution to Eq. (6) is given by

$$T(r, t) = \int_0^t \int_V \frac{Q(r', t')}{\rho C_p} g(r, t, r', t') dr' dt', \quad (7)$$

where $g(r, t, r', t')$ is given by³³

$$g(r, t, r', t') = \frac{1}{(4\pi D(t - t'))^{3/2}} \cdot \exp\left(-\frac{|r - r'|^2}{4D(t - t')}\right). \quad (8)$$

Eq. (7) is subsequently approximated by assuming that energy absorption takes place at a finite number of points and time instants, leading to

$$T(r, t) \approx \sum_{i,j} T_{i,j}(r, t), \quad (9)$$

where

$$T_{i,j}(r, t) = \frac{E_i(t_j)}{\rho C_p} \left(\frac{1}{(4\pi D(t - t_j))^{3/2}} \right) \cdot \exp\left(\frac{-|r - r_j|^2}{4D(t - t_j)}\right). \quad (10)$$

The spatial locations r_i and temporal instants t_j correspond to the position of the reconstructed voxels and the optoacoustic sampling instants, respectively. $E_i(t_j)$ represents the amount of energy absorbed in the i -th voxel for the j -th time interval (between $t_j - \Delta t$ and t_j), i.e.,

$$E_i(t_j) = \rho V C_p \Delta T_i(t_j), \quad (11)$$

where V is the volume corresponding to each reconstructed voxel and $\Delta T_i(t_j)$ is the temperature rise at the i -th voxel during the j -th interval. Eq. (10) is then rewritten as

$$T_{i,j}(r, t) = V \Delta T_i(t_j) \left(\frac{1}{(4\pi D(t - t_j))^{3/2}} \right) \cdot \exp\left(\frac{-|r - r_j|^2}{4D(t - t_j)}\right). \quad (12)$$

On the other hand, for voxels whose values exceeded 20% of the maximum value in the entire 3D image volume the temperature was solely estimated by relying on the instantaneous OA signal values $T(r_i, t_j)$ without considering thermal diffusion, i.e.,

$$\Delta T_i(t_j) = T(r_i, t_j) - T(r_i, t_j - \Delta t). \quad (13)$$

Mouse experiments. The performance of the suggested temperature mapping approach was tested experimentally in a mouse that was ablated *post mortem*. Specifically, the ablation fiber was rectally inserted with the mouse lying in a supine position, so that the OA laser illuminated the back of the mouse. The initial (ambient) temperature of the mouse was $T_0 = 22^\circ\text{C}$. The ablation laser was stopped after 36 s and the optoacoustic images were acquired from the heated area over 120 s, thus also covering the cooling phase. All experiments were performed in full compliance with the institutional guidelines of the Helmholtz Center Munich and with approval from the Government District of Upper Bavaria. Note that a large number of thermocouples would be required for validating the temperature mapping results in 3D in the highly heterogeneous murine tissue while accurate positioning of the thermocouples in the intact mouse is technically challenging. Thus, no thermocouple validation was performed in this case and the experiment was done in order to showcase temperature monitoring in a real heterogeneous biological specimen.

Results

Tissue-mimicking phantom experiments. Figure 2 shows the OA images captured at three different instants during the laser heating procedure. The ablation fiber was aligned parallel to the tubings at a distance of approximately 5 mm from the leftmost one. A progressive increase in the OA signal intensity as the temperature rises is clearly visible in all tubings (Fig. 2a–c). The temperature increase in blood was then estimated from Eq. 5, where the F factor is calculated according to Eq. 4. The estimated temperature increase inside the three tubings is plotted in Fig. 2d (dashed lines). For calculating the relative signal increments, a reference OA image (the baseline image) was taken as the average of 50 frames immediately preceding the ablation procedure. The temperature increase values measured with the thermocouples (located approximately at the same ROIs) are also shown in Fig. 2d (continuous lines).

As expected, lower temperature increments result in larger disagreement between the optoacoustically-estimated temperature values and those measured with the thermocouples. Figure 2e indicates that the relative deviations in F remain below 10% if the temperature increases by at least 3°C . These deviation can be partially attributed to the relative uncertainty in the measured Δp_0 values (see Eq. 3), originating from the noise in OA measurements. Note however that the discrepancy may also result from inaccuracies in the theoretical F values (F_{th}) that were calculated using Eq. 4 assuming a homogenous water medium. Additional uncertainty exists in the location of the thermocouple tip, which may not exactly coincide with the locations where the representative OA traces were analyzed, as labeled by circles in Fig. 2a.

Mouse experiments. Figure 3a shows the reconstructed OA images (MIPs along the transverse and sagittal views) for three different instants during photothermal therapy performed in a mouse *post mortem*. Clearly, the OA images deliver 3D maps of the mouse anatomy at high spatial resolution in the $150\ \mu\text{m}$ range while also

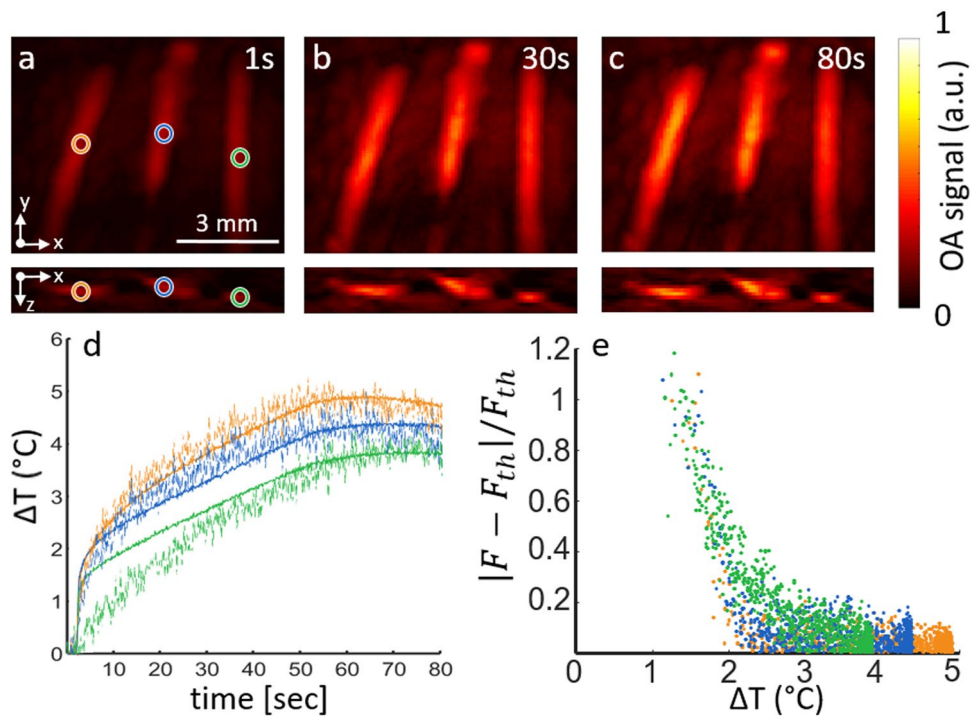


Figure 2. Optoacoustic temperature estimations in a tissue mimicking phantom. (a–c) Transverse and coronal maximum intensity projection (MIP) optoacoustic images reconstructed for three different time points during laser heating of the phantom; (d) The temperature increase estimated from the optoacoustic signal variations (dashed curves) as compared to the temperature increase measured with thermocouples (solid curves). The regions of interest considered for the estimation are marked in panel a; (e) Relative deviation of the F factor from the theoretical value as a function of the temperature increase.

exhibiting rapid OA signal variations closely following the temperature rise. The dynamic temperature maps estimated via the methodology described in the Methods section are shown in Fig. 3b. Plots in Fig. 3c depict the temporal evolution of the temperature profiles at 5 different locations, as indicated in Fig. 3a. The gradual heating and thermal diffusion effects can be best perceived in a video showing real-time monitoring of the temperature distribution in the mouse (Supplementary Video 1). It can be observed that points closer to the ablation fiber experience more pronounced temperature rise in the first few seconds following initiation of the ablation procedure and reach the maximum temperature approximately when the ablation laser is switched off. On the other hand, lower peak temperatures and slower temperature changes are exhibited at locations farther away from the fiber (e.g. points 1, 2 and 3). Yet, the temperature in those regions remains nearly constant after the heating is terminated, indicating that thermal diffusion plays a dominant role in maintaining the energy balance in those regions.

Discussion

The lack of simple and reliable non-invasive temperature feed-back represents a major barrier towards broader adaptation of laser-based thermotherapy procedures in pre-clinical research and clinical routine. The presented results showcase that volumetric OA imaging may emerge as a promising tool for quantitative monitoring of the temperature field during thermal therapies. Optoacoustics is particularly suitable for this purpose due to its high sensitivity to the temperature changes as well as the powerful ability to represent the temperature changes in an entire treated volume with both high spatial and temporal resolutions in the 150 μm and 10 ms ranges, respectively.

Note that in the experiments performed, the temperature dependence of the Grüneisen parameter was adopted from an empirical formula for diluted aqueous solutions, which may not accurately represent the physical reality in soft biological tissues²⁶. Thus, accurate calibration of this parameter in different tissues may result in better accuracy when estimating the temperature-dependence of the OA signals. In addition, accuracy of the temperature estimations has been shown to be directly linked to the contrast and noise levels of the reconstructed optoacoustic images while the average optoacoustic signal strength is expected to drop by approximately an order of magnitude for each centimeter of penetration in living tissues at the near-infrared wavelengths³⁰. In the current study, temperature estimations were achieved at up to 10 mm depth in *ex-vivo* mouse tissues without employing signal averaging. For monitoring at deeper locations, one potential solution may involve guiding the OA excitation beam through the same fiber used for delivering the ablation beam. In this way, since both OA imaging and laser ablation are usually performed in the near-infrared wavelength range, an even higher level of hardware integration could be potentially achieved if the same laser is used for both ablation and generation of OA responses.

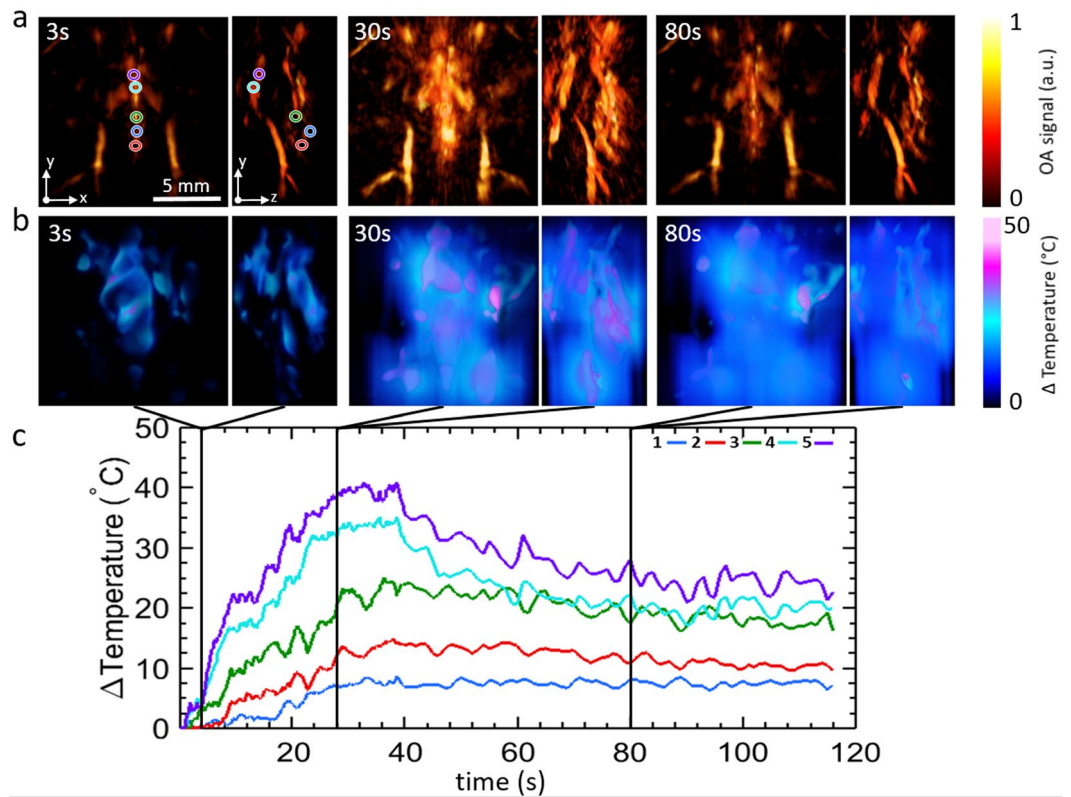


Figure 3. Volumetric optoacoustic monitoring of temperature during photothermal therapy performed in a mouse *post mortem*. **(a)** Transverse and lateral MIPs of the reconstructed optoacoustic volumes at different time points during the treatment. The tip of the ablation fiber is located approximately at the center of the displayed volumes. **(b)** Transverse and lateral MIPs of the estimated temperature maps at the same time points. **(c)** Actual temporal traces of temperature from the points labeled in **(a)**.

The amount of monitored information can be enhanced by acquisition of multispectral optoacoustic tomography (MSOT) data³⁴. Since MSOT enables identifying spectral variations in the imaged tissue, this information may further help improving the accuracy of the suggested temperature monitoring approach by recognizing alterations in the optical or chemical parameters of the imaged tissue resulting from e.g. tissue coagulation.

In the present study, the underlying modeling assumption was that the tissue optical properties remain unchanged during the heating process, which is not the case if tissue coagulation or other irreversible thermal damage occur. It has been previously observed that a stronger and non-linear dependence of the OA signal intensity on temperature was produced in tissues heated above 53 $^{\circ}$ C²⁶. In addition, not only the Grüneisen parameter but several other physical parameters, such as optical absorption and scattering, are altered due to tissue coagulation³⁴. As a result, solutions of the OA inversion and thermal diffusion problems in three and four dimensions become much more complicated in this case and require a different mathematical treatment, which will be addressed in future work. During *in-vivo* thermal therapy treatments, it is further expected that the results are affected by alterations in blood perfusion induced by tissue heating. Indeed, a higher blood volume may lead to an additional OA signal increase not related to the temperature changes. On the other hand, increased blood perfusion also has a cooling effect^{2,35}, which may result in further inaccuracies introduced into the suggested thermal diffusion model.

Conclusion

In conclusion, we introduced a new high resolution volumetric temperature monitoring method based on real-time acquisition of three-dimensional optoacoustic data coupled with thermal-diffusion-based model of heat distribution in tissues. The results suggest that the proposed approach is capable of mapping the development of the temperature field during laser-induced thermal therapies, which can potentially contribute to improving safety and efficacy of these treatments.

References

1. Moros, E.G. Physics of thermal therapy: fundamentals and clinical applications. *CRC Press*, (2012).
2. Chu, K. F. & Dupuy, D. E. Thermal ablation of tumours: biological mechanisms and advances in therapy. *Nature Reviews Cancer*. **14**, 199–208 (2014).
3. Mensel, B., Weigel, C. & Hosten, N. Laser-induced thermotherapy. Minimally invasive tumor therapies. *Springer Berlin Heidelberg*. 69–75 (2006).

4. Torres-Reveron, J., Tomaszewicz, H. C., Shetty, A., Amankulor, N. M. & Chiang, V. L. Stereotactic laser induced thermotherapy (LITT): a novel treatment for brain lesions regrowing after radiosurgery. *Journal of neuro-oncology*. **113**, 495–503 (2013).
5. Ke, H. *et al.* Gold nanoshelled liquid perfluorocarbon magnetic nanocapsules: a nanotheranostic platform for bimodal ultrasound/magnetic resonance imaging guided photothermal tumor ablation. *Theranostics*. **14**, 12–23 (2014).
6. Zhang, F. *et al.* Noninvasive dynamic imaging of tumor early response to nanoparticle-mediated photothermal therapy. *Theranostics*. **5**, 1444–1455 (2015).
7. Zou, L. *et al.* Current approaches of photothermal therapy in treating cancer metastasis with nanotherapeutics. *Theranostics*. **6**, 762–772 (2016).
8. Lyu, Y. *et al.* Intraparticle molecular orbital engineering of semiconducting polymer nanoparticles as amplified theranostics for *in vivo* photoacoustic imaging and photothermal therapy. *ACS Nano*. **10**, 4472–4481 (2016).
9. Lyu, Y., Xie, C., Chechetka, S. A., Miyako, E. & Pu, K. Semiconducting polymer nanobioconjugates for targeted photothermal activation of neurons. *Journal of the American Chemical Society*. **138**, 9049–9052 (2016).
10. Datta, N. R. *et al.* Local hyperthermia combined with radiotherapy and/or chemotherapy: Recent advances and promises for the future. *Cancer Treatments Reviews*. **41**, 742–753 (2015).
11. Bandyopadhyay, S. *et al.* Low-Intensity focused ultrasound induces reversal of tumor-induced T Cell tolerance and prevents immune escape. *The Journal of Immunology*. **196**, 1964–1976 (2016).
12. Shaw, A., Haar, G. T., Haller, J. & Wilkens, V. Towards a dosimetric framework for therapeutic ultrasound. *International Journal of Hyperthermia*. **31**(2), 182–192 (2015).
13. Saccomandi, P., Schena, E. & Silvestri, S. Techniques for temperature monitoring during laser-induced thermotherapy: An overview. *International Journal of Hyperthermia*. **29**, 609–619 (2013).
14. Liu, L. W. *et al.* Fluorescence spectra shape based dynamic thermometry. *Applied Physics Letters*. **104**(3) (2014).
15. Liu, L. *et al.* Wideband fluorescence-based thermometry by neural network recognition: Photothermal application with 10 ns time resolution. *Journal of Applied Physics*. **118**(18) (2015).
16. Lahiri, B. B., Subramainam, B., Jayakumar, T. & Philip, J. Medical applications of infrared thermography: A review. *Infrared Physics & Technology*. **55**(4), 221–235 (2012).
17. Lewis, M. A., Staruch, R. M. & Chopra, R. Thermometry and ablation monitoring with ultrasound. *International Journal of Hyperthermia*. **31**, 163–181 (2015).
18. Fani, F., Saccomandi, P. & Silvestri, S. CT-based thermometry: An overview. *International Journal of Hyperthermia*. **30**, 219–227 (2014).
19. Rieke, V. & Pauly, K. B. MR thermometry. *Journal of Magnetic Resonance Imaging*. **27**(2), 376–390 (2008).
20. Petrova, E. V. *et al.* Using photoacoustic imaging for measuring the temperature dependence of Gruneisen parameter in optically absorbing solutions. *Optics Express*. **21**(21), 25077–25090 (2013).
21. Gao, L. *et al.* Single-cell photoacoustic thermometry. *Journal of biomedical optics*. **18**(2), 026003–026003 (2013).
22. Shah, J. *et al.* Photoacoustic imaging and temperature measurement for photothermal cancer therapy. *Journal of biomedical optics*. **13**(3), 034024–034024 (2008).
23. Yao, L., Huang, H. & Jiang, H. Finite-element-based photoacoustic imaging of absolute temperature in tissue. *Optics letters*. **39**, 5355–5358 (2014).
24. Pang, G. A., Bay, E., Deán-Ben, X. L. & Razansky, D. Three-dimensional photoacoustic monitoring of lesion formation in real time during radiofrequency catheter ablation. *Journal of cardiovascular electrophysiology*. **26**(3), 339–345 (2015).
25. Gray, J. P. *et al.* Multi-wavelength photoacoustic visualization of high intensity focused ultrasound lesions. *Ultrasonic imaging*. **38**(1), 96–112 (2016).
26. Larina, I. V., Larin, K. V. & Esenaliev, R. O. Real-time photoacoustic monitoring of temperature in tissues. *Journal of Physics D: Applied Physics*. **38**(15), 2633–2639 (2005).
27. Larin, K. V., Larina, I. V., Motamedi, M. & Esenaliev, R. O. Monitoring of temperature distribution with photoacoustic technique in real time. *SPIE Proc.* **3916**, 311–321 (2000).
28. Yao, D., Zhang, C., Maslov, K. & Wang, L. V. Photoacoustic measurement of the Gruneisen parameter of tissue. *Journal of biomedical optics*. **19**(1), 017007–017007 (2014).
29. Deán-Ben, X. L., Ozbek, A. & Razansky, D. Volumetric real-time tracking of peripheral human vasculature with GPU-accelerated three-dimensional photoacoustic tomography. *IEEE transactions on medical imaging*. **32**(11), 2050–2055 (2013).
30. Wang, L. V. & Wu, H. Biomedical optics: principles and imaging. *John Wiley & Sons*. (2012).
31. Wang, W. & Mandelis, A. Thermally enhanced signal strength and SNR improvement of photoacoustic radar module. *Biomedical Optics Express*. **5**, 2785–2790 (2014).
32. A. A. Oraevsky, A. A., Esenaliev, R. O., Motamedi, M., Karabutov, A. A. Real time photoacoustic monitoring of changes in tissue properties. US Patent 6,309,352.
33. Niemz, M. H. Laser-tissue interactions: fundamentals and applications. *Springer Science & Business Media*. (2013).
34. Deán-Ben, X. L., Gottschalk, S., McLarney, B., Shoham, S. & Razansky, D. Advanced photoacoustic methods and labelling approaches for imaging of multi-scale *in vivo* dynamics. *Chem Soc Rev* **46**, 2158–2198 (2017).
35. Shih, T. *et al.* Numerical analysis of coupled effects of pulsatile blood flow and thermal relaxation time during thermal therapy. *International Journal of Heat and Mass Transfer*. **55**, 3763–3773 (2012).

Acknowledgements

This work was supported by the German Research Foundation (DFG) and the Technical University of Munich within the funding programme Open Access Publishing.

Author Contributions

D.R., X.L.D.-B. and F.J.O.L. proposed and designed the project. D.R. and X.L.D.-B. designed the photoacoustic imaging system. R.S. provided the laser ablation fiber system. X.L.D.-B. and F.J.O.L. implemented image reconstruction and processing algorithms and analyzed the data. D.R. and R.S. supervised the study. All authors discussed the results and contributed to writing the manuscript.

Additional Information

Supplementary information accompanies this paper at doi:10.1038/s41598-017-09069-5

Competing Interests: The authors declare that they have no competing interests.

Publisher's note: Springer Nature remains neutral with regard to jurisdictional claims in published maps and institutional affiliations.



Open Access This article is licensed under a Creative Commons Attribution 4.0 International License, which permits use, sharing, adaptation, distribution and reproduction in any medium or format, as long as you give appropriate credit to the original author(s) and the source, provide a link to the Creative Commons license, and indicate if changes were made. The images or other third party material in this article are included in the article's Creative Commons license, unless indicated otherwise in a credit line to the material. If material is not included in the article's Creative Commons license and your intended use is not permitted by statutory regulation or exceeds the permitted use, you will need to obtain permission directly from the copyright holder. To view a copy of this license, visit <http://creativecommons.org/licenses/by/4.0/>.

© The Author(s) 2017

FOUR-DIMENSIONAL OPTOACOUSTIC MONITORING OF TISSUE HEATING WITH MEDIUM INTENSITY FOCUSED ULTRASOUND [4]

Peer-reviewed Journal Paper

Autors: Francisco Javier Oyaga Landa^{a,b,1}, Silvia Ronda Penacoba^{c,1}, Francisco Montero de Espinosa^c, Daniel Razansky^{a,b}, and Xosé Luís Deán-Ben^{a,*}

Affiliations:

^aInstitute for Biological and Medical Imaging (IBMI), Helmholtz Center Munich, Neuherberg, Germany

^bSchool of Medicine, Technical University of Munich, Germany

^cITEFI-CSIC, Institute of Physics and Communication Technologies, Madrid, Spain

*Corresponding author.

¹These authors contributed equally to this work.

In: Ultrasonics Ref: ULTRAS_2018_315_R1.

Abstract: Medium-intensity focused ultrasound (MIFU) concerns therapeutic ultrasound interventions aimed at stimulating physiological mechanisms to reinforce healing responses without reaching temperatures that can cause permanent tissue damage. The therapeutic outcome is strongly affected by the temperature distribution in the treated region and its accurate monitoring represents an unmet clinical need. In this work, we investigate on the capacities of four-dimensional optoacoustic tomography to monitor tissue heating with MIFU. Calibration experiments in a tissue-mimicking phantom have confirmed that the optoacoustically-estimated temperature variations accurately match the simultaneously acquired thermocouple readings. The performance of the suggested approach in real tissues was further shown with bovine muscle samples. Volumetric temperature maps were rendered in real time, allowing for dynamic monitoring of the ultrasound focal region, estimation of the peak temperature and the size of the heat-affected volume.

Contribution of thesis author: Study design, laboratory measurements, processing algorithms, signal analysis and computer-aided results and methods.

Copyright Notice: Copyright © 2018, Elsevier Publishing Group, Ultrasonics.



Short communication

Four-dimensional optoacoustic monitoring of tissue heating with medium intensity focused ultrasound

Francisco Javier Oyaga Landa^{a,b,1}, Silvia Ronda Penacoba^{c,1}, Francisco Montero de Espinosa^c, Daniel Razansky^{a,b}, Xosé Luís Deán-Ben^{a,*}

^a Institute for Biological and Medical Imaging (IBMI), Helmholtz Center Munich, Neuherberg, Germany

^b School of Medicine, Technical University of Munich, Germany

^c ITEFI-CSIC, Institute of Physics and Communication Technologies, Madrid, Spain



ARTICLE INFO

Keywords:

Thermal treatment monitoring
Optoacoustic tomography
Photoacoustic imaging
Temperature monitoring
Therapeutic ultrasound

ABSTRACT

Medium-intensity focused ultrasound (MIFU) concerns therapeutic ultrasound interventions aimed at stimulating physiological mechanisms to reinforce healing responses without reaching temperatures that can cause permanent tissue damage. The therapeutic outcome is strongly affected by the temperature distribution in the treated region and its accurate monitoring represents an unmet clinical need. In this work, we investigate on the capacities of four-dimensional optoacoustic tomography to monitor tissue heating with MIFU. Calibration experiments in a tissue-mimicking phantom have confirmed that the optoacoustically-estimated temperature variations accurately match the simultaneously acquired thermocouple readings. The performance of the suggested approach in real tissues was further shown with bovine muscle samples. Volumetric temperature maps were rendered in real time, allowing for dynamic monitoring of the ultrasound focal region, estimation of the peak temperature and the size of the heat-affected volume.

1. Introduction

Therapeutic ultrasound (US) comprises a myriad of techniques routinely used in the clinics to treat pathological tissues, such as tumors, kidney stones, neurological disorders, blood clots, hemorrhages or injured muscles and tendons [1,2]. The majority of US-based treatments involve thermal effects produced via tissue heating with average intensity levels exceeding those permitted for diagnostic US imaging purposes ($> 0.1 \text{ W/cm}^2$). High-intensity focused ultrasound (HIFU) ($100\text{--}10,000 \text{ W/cm}^2$), is used to selectively destroy abnormal tissues, such as malignant neoplastic lesions, via local temperature elevations exceeding the coagulation thresholds [3,4]. HIFU has been also used at power levels below the thresholds required for ablation, such as in intense therapy ultrasound (ITU), e.g. by creating thermal injury zones in the tissue, initiating tissue repair cascade, promoting collagen generation and thus a healing response [5,6]. Low intensity pulsed ultrasound stimulation (LIPUS) has also shown beneficial effects in tissue healing with typical US intensities lower than 0.1 W/cm^2 and a temperature rise less than 1°C [7]. In addition, non-thermal physical effects, such as cavitation and acoustic streaming, have shown to influence cell membrane permeability and increase cellular activity [8]. Medium-intensity

focused ultrasound (MIFU), with acoustic intensity levels between those used in echography and HIFU (typically $5\text{--}300 \text{ W/cm}^2$), represents a largely unexplored scientific niche that can lead to combined and cooperative thermal and non-thermal physical effects in soft tissues for performing physio or cancer therapy, either directly or via local drug delivery. Dedicated and flexible electronics with programmable parameters – voltage, signal shape, frequency and number of active elements – as well as specialized US array transducers need to be studied and developed to investigate the outcome of US physiotherapy treatments. In our case, using special array transducers and electronics capable to focalize in 3D, temperature increases in phantoms up to 10°C in less than 30 s have been achieved with intensities of tens of W/cm^2 . Tissue heating results from absorption of US waves, while other effects, such as cavitation or acoustic streaming, may additionally take place. Effective application of US requires accurate monitoring of the spatio-temporal temperature distribution during the procedure, control over the delivered US intensity levels and duration of the treatment as well as precise spatial targeting in the body [9].

Considerable inconsistencies in the clinical outcomes for different therapeutic US protocols have been reported [10]. Thereby, the development of efficient monitoring methods is paramount for improving

* Corresponding author.

E-mail address: xl.deanben@helmholtz-muenchen.de (X.L. Deán-Ben).

¹ These authors contributed equally to this work.

the therapeutic efficacy while avoiding unnecessary tissue damage. Of particular importance is the feasibility to render real-time feedback on the spatio-temporal temperature distribution in the treated tissue. Heat-driven cell deterioration typically starts at temperatures above 50 °C, while cell death strongly depends on the exposure duration to a certain temperature [4]. For instance, coagulative necrosis and immediate cell death is typically produced in HIFU when reaching temperatures above 55 °C for 1 s or longer [11]. Temperature monitoring is also essential in MIFU for preventing overheating. Also, the outcome of a MIFU procedure highly depends on the temperature values and the exposure time. Then, controlling the spatio-temporal distribution of temperature is generally essential in MIFU. Intrusive temperature monitoring methods based on thermocouples, thermistors or fiber-optic detectors can be used for temperature control [12]. However, those are invasive approaches that can only retrieve temperature readings from a limited number of discrete locations. Mapping of the temperature distribution was further attempted using non-invasive imaging approaches, including infrared thermometry [13], analysis of US backscattered signals [14,15], X-ray computed tomography (CT) [16] or magnetic resonance imaging (MRI) [17]. However, all these methods have limitations for real-time volumetric temperature mapping associated to the achievable penetration depth, contrast or spatio-temporal resolution.

Optoacoustic (OA) imaging constitutes an advantageous approach for monitoring thermal treatments as it provides high sensitivity to changes in temperature and can further detect tissue composition changes associated with coagulation [18–21]. OA can reach depths of ~1–2 cm as reported by several groups [22–25], which can be sufficient for many MIFU applications e.g. in physical rehabilitation or pain management [26,27]. To this end, OA monitoring and guidance has been used to control thermal therapies involving radio-frequency ablation [28], laser-induced thermotherapy [29,30], cryoablation [31], therapeutic US procedures including HIFU [32] or nanoparticle-based targeted therapies [33]. One of the advantages of the OA method is the possibility to integrate it with MIFU or HIFU using the same transducer array [34]. Yet, real-time volumetric mapping of the temperature distribution during US thermotherapy, particularly for intensity levels below the thermal damage thresholds, has never been attempted. Herein, using a novel MIFU multi pulse electronic system and a two dimensional piezoelectric spherical matrix array, we demonstrate the feasibility of four dimensional (real-time three-dimensional) optoacoustic mapping of the induced spatio-temporal temperature distribution in a tissue-mimicking phantom and in an ex-vivo bovine tissue sample.

2. Materials and methods

2.1. Experimental set-up and signal processing

A lay-out of the experimental set-up is depicted in Fig. 1a. MIFU heating was induced with a self-developed annular array probe consisting of 8 equal-area coaxial rings, which allowed focusing the US beam along the axial direction. This allows concentrating the energy in a region that resembles an elongated rice grain with approximate dimensions of 1.5–2 mm in width and 1–1.5 cm in length, i.e., the sound beam maximum intensity is confined within a ~0.04 cm³ volume. The excitation signals in each element were delayed in order to focus the US beam by constructive interference at a distance of 5 cm from the active surface. Each element of the array has an area of 0.88 cm² and a central frequency of 2 MHz. The array has a total diameter of 3 cm. The elements were excited with a custom-made multichannel electronic driving system (SITAU, Dasel Sistemas, Madrid, Spain) controlled with a MATLAB® code. When driven with a negative square pulse of 150 V, a peak pressure of 3 MPa is generated at the focus, which corresponds to $I_{SPTP} = 300 \text{ W/cm}^2$ of acoustic intensity [5]. The pressure was measured with a needle hydrophone (DAPCO 54389) with 0.6 mm active diameter.

OA volumetric temperature monitoring was performed with a custom-made spherical matrix array consisting of a 256 piezoelectric elements with 90° (0.59π solid angle) angular coverage [35]. Each element of the array has an area of 3 × 3 mm², central frequency of 4 MHz and > 80% detection bandwidth, providing a nearly isotropic imaging resolution of ~200 μm around the geometrical center of the sphere. The OA field of view is in the order of 1 cm³, which can be covered by the depth of field of the MIFU array. The OA detection array was positioned orthogonally with respect to the MIFU array and acoustic coupling was guaranteed by immersing the entire set-up in water (Fig. 1a). Optoacoustic responses were excited with a short-pulsed (< 10 ns) tunable laser source (Innolas Laser GmbH, Krailling, Germany) guided via a custom-made fiber bundle (CeramOptec GmbH, Bonn, Germany) through a cylindrical cavity in the center of the array. Optical fluence of ~11 mJ cm⁻² was measured at the surface of the sample at 720 nm illumination wavelength, corresponding to the maximum energy of the laser. The pulse repetition frequency of the laser source was set to 10 Hz. The 256 optoacoustic signals corresponding to all elements of the array were simultaneously acquired at 40 mega-samples per second (MSPS) by a custom-made data acquisition (DAQ) system (Falkenstein Mikrosysteme GmbH, Taufkirchen, Germany) triggered with the Q-switch output of the laser. Synchronization between OA imaging and MIFU excitation was achieved by delaying the US excitation tone-bursts by 100 μs with respect to the laser trigger used for the OA signal acquisition, as depicted in the timing diagram in Fig. 1b. Specifically, the employed MIFU excitation protocol consisted of emitting 50 tone-bursts of 125 ($I_{SPTA} = 9.4 \text{ W/cm}^2$) or 255 ($I_{SPTA} = 19.1 \text{ W/cm}^2$) cycles with 150 V negative square amplitude and carrier frequency of 2 MHz, at a pulse repetition frequency (PRF) of 1 kHz following each laser pulse. OA images were reconstructed with a graphics processing unit (GPU)-based three-dimensional back-projection algorithm [36]. Prior to reconstruction, the acquired raw signals were deconvolved with the known impulse response of the array elements and band-pass filtered with cut-off frequencies between 0.1 MHz and 6 MHz.

2.2. Temperature estimation method

The OA temperature estimation method is based on the temperature dependence of the Grüneisen parameter, corresponding to the thermoelastic conversion efficiency. For short-pulsed laser excitation under thermal and stress-confinement conditions [37], the optoacoustically-induced pressure amplitude is approximately given by $p_0 = \Gamma \mu_a \Phi$, being Γ the (dimensionless) Grüneisen parameter, μ_a the optical absorption coefficient and Φ the light fluence. For water and diluted aqueous solutions, the temperature dependence of the Grüneisen parameter can be approximated via [37]

$$\Gamma(T) = 0.0043 + 0.0053T, \quad (1)$$

where T is expressed in °C. Note that Eq. (1) has been previously verified with empirical measurements across a wide range of temperatures [38]. According to Eq. (1), the relative change of the OA signal as a function of temperature increase ΔT can be then expressed as [30]

$$\frac{\Delta p_0}{p_{0,0}} = \frac{0.0053\Delta T}{0.0043 + 0.0053 \cdot T_0} \quad (2)$$

being $p_{0,0}$ and T_0 the initial (baseline) OA signal and the initial temperature, respectively, before the application of MIFU heating. Δp_0 is the increase in OA signal with respect to $p_{0,0}$. According to Eq. (2), the amplitude of the OA signals is expected to increase by approximately 2.7% per degree for temperature levels around 36 °C in living biological tissues. The temperature increment can then be estimated from the relative OA signal increase as

$$\Delta T = \Delta p_0 (0.8113 + T_0) / p_{0,0} \quad (3)$$

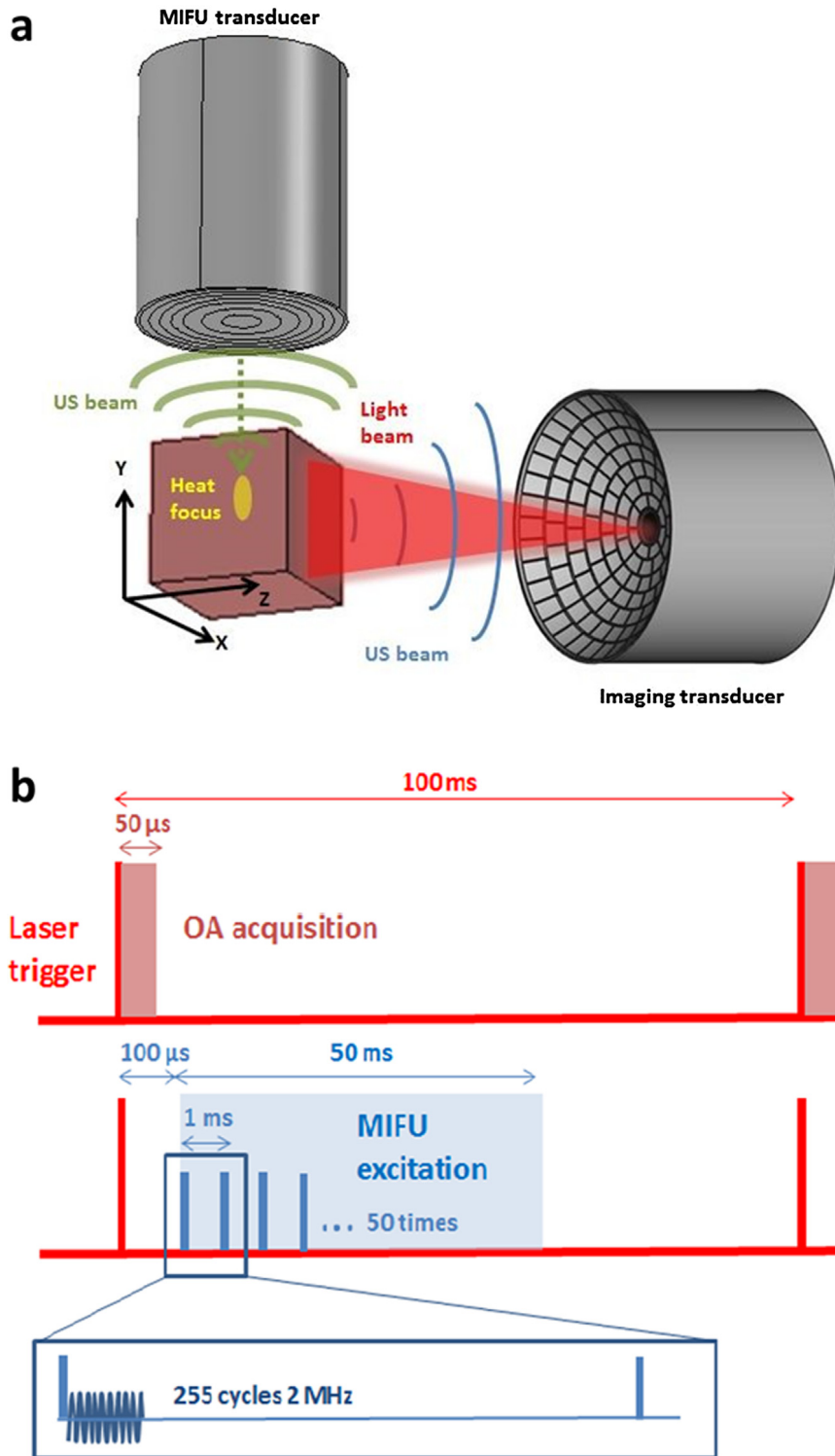


Fig. 1. Lay-out of the experimental setup. (a) Schematic representation of the OA transducer array and the MIFU transducer. (b) Schematic timing diagram of MIFU excitation and OA acquisition.

2.3. Phantom validation experiment

A 8.5 mm wide square-shaped tissue-mimicking phantom was first measured to experimentally test the validity of Eq. (3). The phantom consisted of an agar matrix (1.3% w/w agar powder solved in water) mixed with 7.8% w/w of Aluminum Oxide (Al_2O_3) and India ink to create an US attenuation coefficient of 3.6 dBcm^{-1} at 2 MHz frequency and an optical absorption coefficient of $\mu_a \sim 3.5 \text{ cm}^{-1}$ at 720 nm

illumination wavelength. The attenuation coefficient was measured using a typical through-transmission approach with two Panametrics A305 2.25 MHz transducers in a water tank. Different samples with various thicknesses were used for comparing the transmitted amplitude. The optical absorption of a water solution with the same concentration of ink and the acoustic attenuation of the phantom material were estimated with an optical spectrometer (OceanOptics, FL, USA) and from the amplitude of multiple echoes of a sample with 1 cm thickness,

respectively. The speed of sound in the phantom material was taken as 1490 m/s, corresponding to the speed of sound in water for the initial temperature. A thermocouple (Physitemp Instruments Inc., Clifton, New Jersey) was inserted at the front (illuminated) edge of the phantom. The temperature readings were digitized with an integrated NI 9213 DAQ (National Instruments Corporation, Austin, Texas, U.S.). The OA-based temperature estimation method, as described in Eqs. (1)–(3), was used to estimate the temperature at a region of interest (ROI) matching the known location of the thermocouple. This corresponds to the region for which a maximum relative increase in the OA signal was measured. Likewise, the US focus was positioned on the thermocouple tip by raster-scanning the MIFU array until the maximum temperature elevation was measured.

2.4. Ex-vivo bovine tissue experiments

The effectiveness of the proposed approach for temperature mapping in real tissues was subsequently examined in an ex-vivo bovine sample. In a first step, the capability to localize the US focus in a three-dimensional region was tested. For this, the MIFU array was scanned along the axial direction of the OA imaging probe. For each position, the MIFU array was driven as previously described. Considering that no significant thermal diffusion occurs for the protocol duration (15 s), the temperature raise within this time period is assumed to be mainly due to US absorption and so the focus position can be localized. In addition, the spatio-temporal distribution of temperature was estimated during MIFU heating for a fixed position of the US focus. The baseline tissue temperature was $T_0 = 22^\circ\text{C}$. MIFU heating was stopped after 15 s while the OA monitoring continued for 40 s to cover the cooling period. The expected optical absorption coefficient in this type of tissue is approximately 0.2 cm^{-1} [39]. The ultrasound attenuation at 2 MHz was estimated as that of muscle tissue (1.09 dB cm^{-1}) [40]. This is in agreement with lower temperature increase observed as compared to that of the phantom.

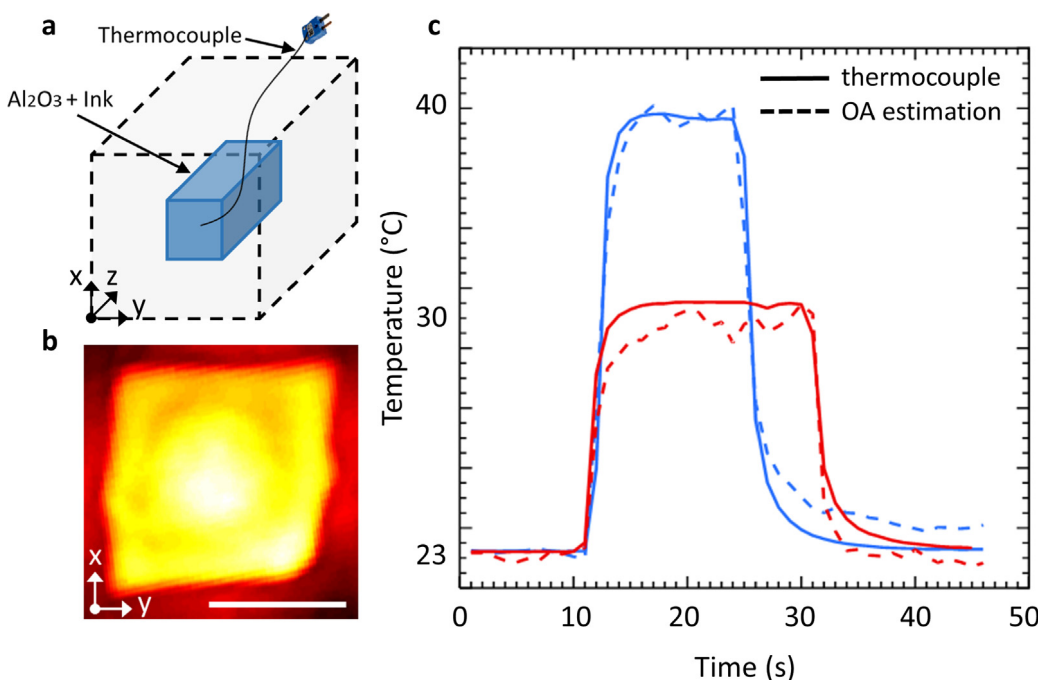


Fig. 2. Validation of the OA temperature monitoring method. (a) Thermocouple location in the tissue mimicking phantom. (b) MIP of the 3D OA image along the z direction, showing the front side of the phantom. Scalebar – 5 mm. (c) OA temperature estimations (dashed lines) along with the corresponding thermocouple readings (continuous lines). The data corresponds to two different MIFU heating procedures using 255 (blue) and 125 (red) cycles. (For interpretation of the references to color in this figure legend, the reader is referred to the web version of this article.)

3. Results

3.1. Phantom validation experiment

Fig. 2a shows a schematic representation of the measurement arrangement. The maximum intensity projection (MIP) along the depth direction of the volumetric OA images taken before the MIFU heating is displayed in Fig. 2b. The temperature increase in the phantom at the thermocouple location was then estimated with Eq. (3). Specifically, two measurements were performed. First, a series of 150 V tone-bursts consisting of 255 cycles ($I_{SPTA} = 19.1\text{ W/cm}^2$) were used to excite the MIFU array for 15 s. In Fig. 2c, the time dependence of temperature measured with the thermocouple versus the temperature estimated from the OA image sequence are represented by the solid and dashed blue lines, respectively. In a second measurement, a series of tone-bursts of 150 V and 125 cycles ($I_{SPTA} = 9.4\text{ W/cm}^2$) were used to drive the MIFU array for 20 s. The corresponding temperature values are shown by solid and dashed red lines in Fig. 2c. The relative OA signal increases were estimated with a reference OA image (the baseline signal) taken as the average of 30 frames immediately preceding the MIFU procedure. It is shown that the optoacoustically-estimated temperature acceptably matches the thermocouple readings. Specifically, the standard deviations of the differences between the corresponding time profiles in Fig. 2c are 0.65°C and 0.88°C for tone-bursts of 125 and 255 cycles, respectively. The good agreement is probably a consequence of the fact that the phantom consists of an aqueous solution, for which Eq. (3) is expected to be valid [30]. Inaccuracies may originate from the discrepancy between the actual location of the thermocouple tip and the analyzed OA traces.

3.2. Ultrasonic focus monitoring

The difference of the OA images of the bovine tissue taken after and before MIFU heating (150 V tone-bursts, 255 cycles, $I_{SPTA} = 19.1\text{ W/cm}^2$) are displayed in Fig. 3. The tissue surface is indicated with a dashed line. No significant heat diffusion was produced during the heating period, so that the differential images reliably represent the heated region, namely, the US focus. The difference in the signal amplitude for the different US focus depths is due to light attenuation, which also

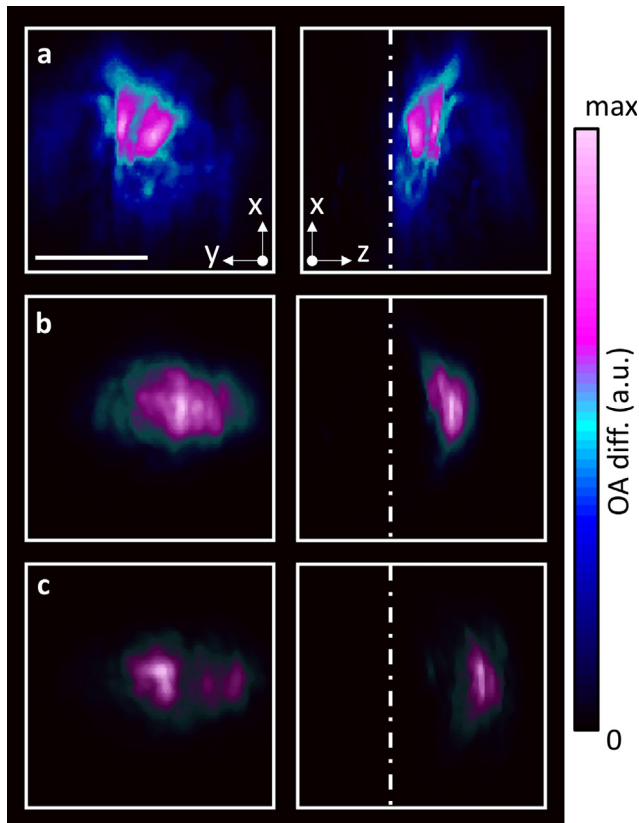


Fig. 3. MIPs of the differential 3D OA images along the z and y directions from ex-vivo bovine tissue for the US focus located at a reference position right underneath the tissue surface (a) and at 1.5 mm (b) and 3 mm (c) points deeper than the reference position, respectively. Scalebar – 5 mm.

results in a lower signal to noise ratio (SNR) at deeper locations. This in turn limits the maximum applicable depth for OA monitoring of the MIFU treatments.

3.3. Temperature mapping in ex-vivo bovine tissue

The results of the temperature mapping experiment in an ex-vivo bovine tissue sample are shown in Fig. 4. Specifically, the spatio-temporal maps of the temperature elevation estimated according to Eq. (3) are displayed in Fig. 4a. Note that no thermocouple was included in this case. Indeed, it was found that it generates a significantly larger optoacoustic signal than the tissue. This leads to streak-type artefacts in the reconstructed images that also affect the estimated temperature maps. It can be seen that the temperature map estimated for the time point of peak temperature elevation (Fig. 4a, 20 s) is tightly centered around the ultrasonic focus location. On the other hand, the heated region spreads over a larger region at later time points during the cooling period (Fig. 4a, 24 s), which indicates that thermal diffusion plays a dominant role in carrying the heat further away from the ultrasonic focus. This is further corroborated in the time traces in Fig. 4b, corresponding to the estimated temperatures at three locations indicated in Fig. 4a at 2.5 s. The incremental heating and thermal diffusion processes can be best identified in a video displaying real-time volumetric monitoring of the temperature map distribution in bovine tissue (Visualization 1). It can be appreciated that voxels closer to the ultrasonic focus experience greater temperature increases and reach the maximum value when the MIFU transducer is turned off. Yet, the generated heat continues diffusing outside the focal region also at later time points. Since the estimated temperature rise was below 15 °C during the entire procedure, no tissue damage should be produced. This was confirmed by visual inspection of the sample after the experiment.

4. Discussion and conclusion

Medium-intensity focused ultrasound (MIFU) therapy aims to provide significant improvements in the efficacy, safety, reliability and metrological traceability of US treatments in both physiotherapy and drug delivery. Here, four-dimensional OA tomography was used to non-invasively measure the temperature increase induced in tissues by a newly designed MIFU prototype system. Of particular importance is the feasibility to provide real-time volumetric temperature feed-back, which can greatly impact the outcome of MIFU-based medical treatments by (1) enabling effective control of the exposure time of the target tissue at a given temperature and (2) preventing tissue overheating above the damage threshold. OA is particularly suitable for temperature mapping applications due to the high sensitivity of the Grüneisen parameter, representing the OA conversion efficiency, to temperature variations [37,41]. Note that in our current experiments the temperature distribution was estimated by assuming the Grüneisen parameter to be equivalent to that of water. Considering that muscle tissues contain approximately 75% water, 20% protein, 1–10% fat and 1% glycogen, this seems a reasonable approximation [42]. However, accurate calibration of the temperature dependence of the Grüneisen parameter is required to assess the error in such approximation and to improve the accuracy of the estimated temperature values. Such calibration may be achieved with optoacoustic methods, for which the light fluence and the absorption coefficient of the tissue of interest need to be determined [43]. This turns particularly challenging *in vivo*, while the optical properties *ex vivo* can significantly change. The high spatio-temporal resolution of the state-of-the-art OA tomography system employed further represents an important advantage. In this work, we have attained spatial resolution of 200 μm at 10 Hz volumetric frame rates, which covers well the spatio-temporal range of the induced temperature variations. Higher spatial and temporal resolutions are also possible by using a similar configuration, which however would come to the detriment of the field of view [44].

It has further been shown that four-dimensional OA tomography enables dynamic localization of the position of the US focus. In this way, more accurate identification of the target tissues can be facilitated prior to applying the therapy. Naturally, the SNR of the differential OA images declines with depth due to light attenuation, the latter dominating over acoustic attenuation for the applicable US frequency range [45]. In order to improve on the achievable monitoring depth, other light delivery methods, e.g. based on endoscopic or intravascular probes, may be additionally considered [46,47]. The regions accessible with OA imaging are confined within $\sim 1\text{--}2$ cm from the surface where light is delivered. This is sufficient for many relevant potential applications of MIFU, such as treatment of active myofascial pain trigger points, stimulation of abdominal or paraspinal muscles or even for neurostimulation of cortical areas in the brain. Registration of OA and US images can further provide enhanced anatomical information and some efficient techniques for hybrid optoacoustic-ultrasound (OPUS) imaging have been recently reported [48].

The monitoring approach introduced in this work can also be potentially applied in treatments based on selective tissue destruction with HIFU [49,50]. These procedures can particularly benefit from augmented information acquired by means of multispectral optoacoustic tomography (MSOT) analysis [51]. The most recently developed OA systems effectively provide five-dimensional (real-time three-dimensional multispectral) imaging capabilities [52], thus enabling tracking of spectroscopic variations in the target tissue, e.g. due to coagulation. It should be noted that the temperature dependence of the OA signals in biological tissues is significantly altered at temperatures exceeding 50 °C [19], so that more accurate calibrations are needed for temperature monitoring in coagulated tissue volumes. The temperature maps *in vivo* are also expected to be affected by induced changes in blood flow, which have a cooling effect. The development of proper models accounting for different effects occurring in living organisms

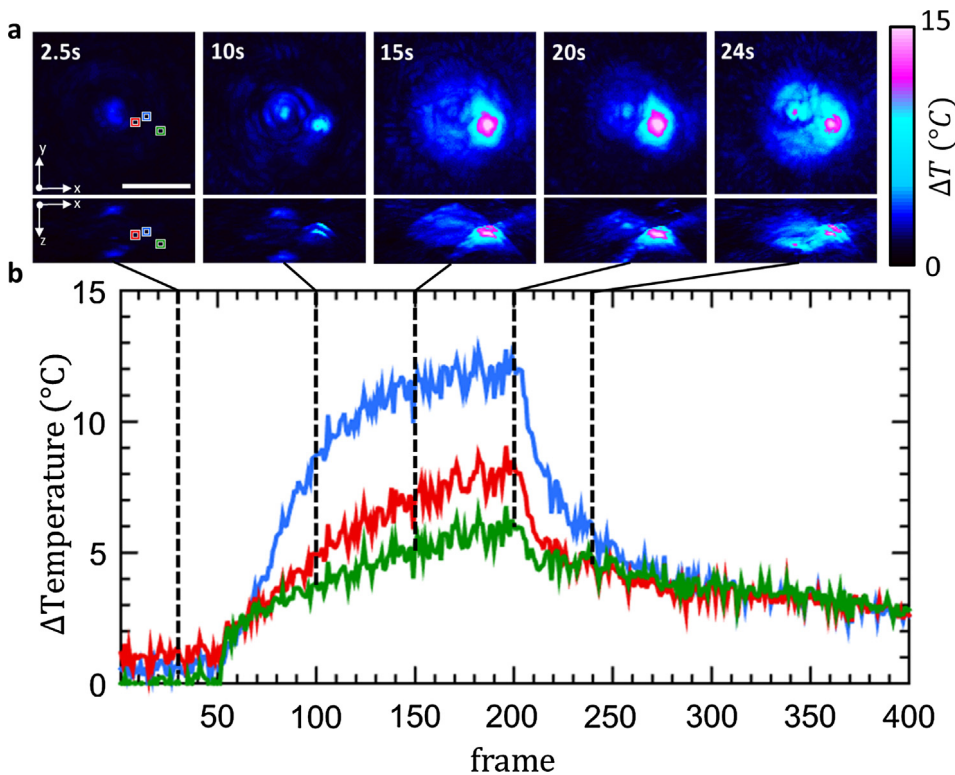


Fig. 4. Volumetric OA monitoring of temperature during MIFU therapy performed in an ex-vivo bovine tissue. (a) MIPs of the estimated 3D temperature increase maps at different time points along the procedure. Scalebar – 5 mm. (b) Temporal profiles of the estimated temperature increase for the 3 points labeled in (a) with the same color. (For interpretation of the references to color in this figure legend, the reader is referred to the web version of this article.)

thus represent an important next step. Also, a temperature rise induces changes in the speed of sound of the heat affected zone, which may affect the reconstructed images obtained by assuming a uniform speed of sound [53], particularly if high-resolution is required.

In conclusion, it has been shown that tissue heating with US can be monitored in three dimensions and in real time with OA tomography. The achieved high sensitivity to temperature variations, high spatial resolution and fast imaging rates anticipate applicability of the suggested approach in various procedures involving low and medium intensity therapeutic US, such as physical rehabilitation [26,54,55], pain management [27] or neurostimulation [56].

Acknowledgements

The authors acknowledge support from the German Research Foundation (DFG) under Research Grant RA 1848/5-1 (D.R.) and the Spanish Ministry of Economy and Competitiveness under project DPI2016-80254-R (F.M.).

Appendix A. Supplementary material

Supplementary data to this article can be found online at <https://doi.org/10.1016/j.ultras.2018.11.011>.

References

- [1] G. ter Haar, Heat and sound: focused ultrasound in the clinic, *Int. J. Hyperth.* 31 (2015) 223–224.
- [2] E.S. Ebbini, G. Ter Haar, Ultrasound-guided therapeutic focused ultrasound: current status and future directions, *Int. J. Hyperth.* 31 (2015) 77–89.
- [3] Y.-S. Kim, H. Rhim, M.J. Choi, H.K. Lim, D. Choi, High-intensity focused ultrasound therapy: an overview for radiologists, *Korean J. Radiol.* 9 (2008) 291–302.
- [4] K.F. Chu, D.E. Dupuy, Thermal ablation of tumours: biological mechanisms and advances in therapy, *Nat. Rev. Cancer* 14 (2014) 199–208.
- [5] T.D. Mast, et al., Bulk ablation of soft tissue with intense ultrasound: modeling and experiments, *J. Acoust. Soc. Am.* 118 (2005) 2715–2724.
- [6] M.H. Slayton, J.K. Barton, Ultrasonics Symposium (IUS), 2014 IEEE International, IEEE, 2014, pp. 1654–1657.
- [7] A. Khanna, R.T. Nelmes, N. Gougoulas, N. Maffulli, J. Gray, The effects of LIPUS on soft-tissue healing: a review of literature, *Brit. Med. Bull.* 89 (2008) 169–182.
- [8] D.M. Hallow, A.D. Mahajan, T.E. McCutchen, M.R. Prausnitz, Measurement and correlation of acoustic cavitation with cellular bioeffects, *Ultrasound Med. Biol.* 32 (2006) 1111–1122.
- [9] G. Clement, Perspectives in clinical uses of high-intensity focused ultrasound, *Ultrasonics* 42 (2004) 1087–1093.
- [10] D.L. Miller, et al., Overview of therapeutic ultrasound applications and safety considerations, *J. Ultrasound Med.* 31 (2012) 623–634.
- [11] G. ter Haar, C. Coussios, High intensity focused ultrasound: physical principles and devices, *Int. J. Hyperth.* 23 (2007) 89–104.
- [12] E. Schena, D. Tosi, P. Saccomandi, E. Lewis, T. Kim, Fiber optic sensors for temperature monitoring during thermal treatments: an overview, *Sensors-Basel* 16 (2016) 1144.
- [13] B. Lahiri, S. Bagavathiappan, T. Jayakumar, J. Philip, Medical applications of infrared thermography: a review, *Infrared Phys. Techn.* 55 (2012) 221–235.
- [14] T.A. Fuhrmann, O. Georg, J. Haller, K.-V. Jenderka, V. Wilkens, Uncertainty estimation for temperature measurement with diagnostic ultrasound, *J. Ther. Ultrasound* 4 (2016) 28.
- [15] M.A. Lewis, R.M. Staruch, R. Chopra, Thermometry and ablation monitoring with ultrasound, *Int. J. Hyperth.* 31 (2015) 163–181.
- [16] F. Fani, E. Schena, P. Saccomandi, S. Silvestri, CT-based thermometry: an overview, *Int. J. Hyperth.* 30 (2014) 219–227.
- [17] V. Rieke, K. Butts Pauly, MR thermometry, *J. Magn. Reson. Imaging* 27 (2008) 376–390.
- [18] K.V. Larin, I.V. Larina, M. Motamedi, R.O. Esenaliev, Biomedical Optoacoustics, International Society for Optics and Photonics, 2000, pp. 311–322.
- [19] K.V. Larin, I.V. Larina, R.O. Esenaliev, Monitoring of tissue coagulation during thermotherapy using optoacoustic technique, *J. Phys. D Appl. Phys.* 38 (2005) 2645.
- [20] J. Kandulla, H. Elsner, R. Birngruber, R. Brinkmann, Noninvasive optoacoustic online retinal temperature determination during continuous-wave laser irradiation, *J. Biomed. Opt.* 11 (2006) 041111–041111-041113.
- [21] E. Petrova, et al., Using optoacoustic imaging for measuring the temperature dependence of Grüneisen parameter in optically absorbing solutions, *Opt. Express* 21 (2013) 25077–25090.
- [22] L.V. Wang, Multiscale photoacoustic microscopy and computed tomography, *Nat. Photon.* 3 (2009) 503.
- [23] I. Stoffels, et al., Metastatic status of sentinel lymph nodes in melanoma determined noninvasively with multispectral optoacoustic imaging, *Sci. Transl. Med.* 7 (2015) 317ra199–317ra199.
- [24] X.L. Deán-Ben, T.F. Fehm, M. Gostic, D. Razansky, Volumetric hand-held optoacoustic angiography as a tool for real-time screening of dense breast, *J. Biophoton.* 9 (2016) 253–259.
- [25] M. Heijblom, et al., Photoacoustic image patterns of breast carcinoma and comparisons with Magnetic Resonance Imaging and vascular stained histopathology, *Sci. Rep.-UK* 5 (2015) 11778.
- [26] L. Claes, B. Willie, The enhancement of bone regeneration by ultrasound, *Prog. Biophys. Mol. Biol.* 93 (2007) 384–398.
- [27] J. Majles, H. Ünalan, High-power pain threshold ultrasound technique in the

- treatment of active myofascial trigger points: a randomized, double-blind, case-control study, *Arch. Phys. Med. Rehabil.* 85 (2004) 833–836.
- [28] G.A. Pang, E. Bay, X. Deán-ben, D. Razansky, Three-dimensional optoacoustic monitoring of lesion formation in real time during radiofrequency catheter ablation, *J. Cardiovasc. Electr.* 26 (2015) 339–345.
- [29] T.F. Fehm, X.L. Deán-Ben, P. Schaur, R. Sroka, D. Razansky, Volumetric optoacoustic imaging feedback during endovenous laser therapy—an ex vivo investigation, *J. Biophoton.* 9 (2016) 934–941.
- [30] F.J.O. Landa, X.L. Deán-Ben, R. Sroka, D. Razansky, Volumetric optoacoustic temperature mapping in photothermal therapy, *Sci. Rep.-UK* 7 (2017) 9695.
- [31] E.V. Petrova, M. Motamedi, A.A. Oraevsky, S.A. Ermilov, in: *Proc. SPIE*. 97080G.
- [32] P.V. Chitnis, H.-P. Brecht, R. Su, A.A. Oraevsky, Feasibility of optoacoustic visualization of high-intensity focused ultrasound-induced thermal lesions in live tissue, *J. Biomed. Opt.* 15 (2010) 021313-021313-021315.
- [33] Y. Lyu, et al., Intraparticle molecular orbital engineering of semiconducting polymer nanoparticles as amplified theranostics for in vivo photoacoustic imaging and photothermal therapy, *ACS Nano* 10 (2016) 4472–4481.
- [34] A. Prost, A. Funke, M. Tanter, J.-F. Aubry, E. Bossy, Photoacoustic-guided ultrasound therapy with a dual-mode ultrasound array, *J. Biomed. Opt.* 17 (2012) 0612051–0612056.
- [35] X.L. Dean-Ben, D. Razansky, Portable spherical array probe for volumetric real-time optoacoustic imaging at centimeter-scale depths, *Opt. Express* 21 (2013) 28062–28071, <https://doi.org/10.1364/Oe.21.028062>.
- [36] X.L. Dean-Ben, A. Ozbek, D. Razansky, Volumetric real-time tracking of peripheral human vasculature with GPU-accelerated three-dimensional optoacoustic tomography, *IEEE Trans. Med. Imaging* 32 (2013) 2050–2055.
- [37] L.V. Wang, H.-I. Wu, *Biomedical Optics: Principles and Imaging*, John Wiley & Sons, 2012.
- [38] W. Wang, A. Mandelis, Thermally enhanced signal strength and SNR improvement of photoacoustic radar module, *Biomed. Opt. Express* 5 (2014) 2785–2790.
- [39] S.L. Jacques, Optical properties of biological tissues: a review, *Phys. Med. Biol.* 58 (2013) R37.
- [40] M.O. Culjat, D. Goldenberg, P. Tewari, R.S. Singh, A review of tissue substitutes for ultrasound imaging, *Ultrasound Med. Biol.* 36 (2010) 861–873, <https://doi.org/10.1016/j.ultrasmedbio.2010.02.012>.
- [41] M. Pramanik, L.V. Wang, Thermoacoustic and photoacoustic sensing of temperature, *J. Biomed. Opt.* 14 (2009) 054024.
- [42] A. Listrat, et al., How muscle structure and composition influence meat and flesh quality, *Sci. World J.* 2016 (2016).
- [43] D.-K. Yao, C. Zhang, K.I. Maslov, L.V. Wang, Photoacoustic measurement of the Grüneisen parameter of tissue, *J. Biomed. Opt.* 19 (2014) 017007.
- [44] X.L. Deán-Ben, et al., Functional optoacoustic neuro-tomography for scalable whole-brain monitoring of calcium indicators, *Light Sci. Appl.* 5 (2016) e16201.
- [45] X.L. Dean-Ben, D. Razansky, V. Ntziachristos, The effects of acoustic attenuation in optoacoustic signals, *Phys. Med. Biol.* 56 (2011) 6129–6148, <https://doi.org/10.1088/0031-9155/56/18/021>.
- [46] H. He, A. Buehler, V. Ntziachristos, Optoacoustic endoscopy with curved scanning, *Opt. Lett.* 40 (2015) 4667–4670.
- [47] A. Rosenthal, et al., Sensitive interferometric detection of ultrasound for minimally invasive clinical imaging applications, *Laser Photon. Rev.* 8 (2014) 450–457.
- [48] X. Deán-Ben, E. Mercep, D. Razansky, Hybrid-array-based optoacoustic and ultrasound (OPUS) imaging of biological tissues, *Appl. Phys. Lett.* 110 (2017) 203703.
- [49] H. Cui, X. Yang, Real-time monitoring of high-intensity focused ultrasound ablations with photoacoustic technique: an in vitro study, *Med. Phys.* 38 (2011) 5345–5350.
- [50] J. Gray, et al., Multi-wavelength photoacoustic visualization of high intensity focused ultrasound lesions, *Ultrason. Imaging* 38 (2016) 96–112.
- [51] S. Tzoumas, N. Deliolanis, S. Morscher, V. Ntziachristos, Unmixing molecular agents from absorbing tissue in multispectral optoacoustic tomography, *IEEE Trans. Med. Imaging* 33 (2014) 48–60.
- [52] X.L. Deán-Ben, D. Razansky, Adding fifth dimension to optoacoustic imaging: volumetric time-resolved spectrally enriched tomography, *Light Sci. Appl.* 3 (2014) e137.
- [53] J. Yao, H. Ke, S. Tai, Y. Zhou, L.V. Wang, Absolute photoacoustic thermometry in deep tissue, *Opt. Lett.* 38 (2013) 5228–5231.
- [54] G. Ter Haar, Therapeutic ultrasound, *Eur. J. Ultrasound* 9 (1999) 3–9.
- [55] V.J. Robertson, K.G. Baker, A review of therapeutic ultrasound: effectiveness studies, *Phys. Ther.* 81 (2001) 1339–1350.
- [56] R.L. King, J.R. Brown, W.T. Newsome, K.B. Pauly, Effective parameters for ultrasound-induced in vivo neurostimulation, *Ultrasound Med. Biol.* 39 (2013) 312–331.

OPTOACOUSTIC MONITORING OF RF ABLATION LESION**PROGRESSION [5]****Peer-reviewed Journal Paper**

Autors: Francisco Javier Oyaga Landa^{1,2}, Cagla Özsoy^{1,2}, Xosé Luís Deán-Ben¹, and Daniel Razansky^{1,2,*}

Affiliations:

¹Institute for Biological and Medical Imaging (IBMI), Helmholtz Center Munich, Neuherberg, Germany

²School of Medicine, Technical University of Munich, Germany

*Corresponding author.

In: Photons Plus Ultrasound: Imaging and Sensing 2019 10878, 108782R.

Abstract: Efficient monitoring of radiofrequency ablation procedures is essential to optimize the lesions induced to treat cancer, cardiac arrhythmias and other conditions. Recently, optoacoustic imaging and sensing methods have been suggested as a promising approach to address this challenge, offering unique advantages such as high sensitivity to temperature changes and chemical transformations in coagulated tissues, real-time operation and use of non- ionizing radiation. However, assessing how the ablation lesion boundary progresses is still challenged by changes in optical properties induced during the interventions. Herein, we suggest a new approach for dimensional characterization of the induced lesion based on detecting sharp positive variations in the time derivative of optoacoustic signals. Experiments in porcine tissue samples indicate that such variations are uniquely associated to the onset of ablation and that the method can robustly visualize the evolution of the lesion in three dimensions.

Contribution of thesis author: Laboratory measurements, processing algorithms, signal analysis and computer-aided results and methods.

Copyright Notice: Copyright © 2019, SPIE Reprint Permission, SPIE policies on article-sharing.

PROCEEDINGS OF SPIE

[SPIDigitalLibrary.org/conference-proceedings-of-spie](https://spiedigitallibrary.org/conference-proceedings-of-spie)

Optoacoustic monitoring of RF ablation lesion progression

Francisco Javier Oyaga Landa, Cagla Özsoy, Xosé Luis Deán-Ben, Daniel Razansky

Francisco Javier Oyaga Landa, Cagla Özsoy, Xosé Luis Deán-Ben, Daniel Razansky, "Optoacoustic monitoring of RF ablation lesion progression," Proc. SPIE 10878, Photons Plus Ultrasound: Imaging and Sensing 2019, 108782R (27 February 2019); doi: 10.1117/12.2510775

SPIE.

Event: SPIE BiOS, 2019, San Francisco, California, United States

Optoacoustic monitoring of RF ablation lesion progression

Francisco Javier Oyaga Landa,^{1,2} Cagla Ozsoy,^{1,3} Xosé Luís Deán-Ben,¹ and Daniel Razansky^{1,3,*}

¹Institute for Biological and Medical Imaging (IBMI), Helmholtz Zentrum München, Neuherberg, Germany

²Faculty of Informatics, Technical University of Munich, Munich, Germany

³School of Medicine, Technische Universität München (TUM), Munich, Germany

*Corresponding author: dr@tum.de

ABSTRACT

Efficient monitoring of radiofrequency ablation procedures is essential to optimize the lesions induced to treat cancer, cardiac arrhythmias and other conditions. Recently, optoacoustic imaging and sensing methods have been suggested as a promising approach to address this challenge, offering unique advantages such as high sensitivity to temperature changes and chemical transformations in coagulated tissues, real-time operation and use of non-ionizing radiation. However, assessing how the ablation lesion boundary progresses is still challenged by changes in optical properties induced during the interventions. Herein, we suggest a new approach for dimensional characterization of the induced lesion based on detecting sharp positive variations in the time derivative of optoacoustic signals. Experiments in porcine tissue samples indicate that such variations are uniquely associated to the onset of ablation and that the method can robustly visualize the evolution of the lesion in three dimensions.

Keywords: Radiofrequency Ablation of Tissue; Optoacoustic Tomography; Temperature; Thermal Treatments.

1. INTRODUCTION

Thermal treatments are routinely used in the clinics for a myriad of applications ranging from pain relief to the generation of localized apoptosis and coagulative necrosis in tumors.¹ The induced thermal effects in biological tissues mainly depend on the temperature rise. No permanent tissue damage is generally produced for temperatures below 50°C, and treatments are typically based on bio-stimulation of chemical reactions in muscle, nervous and other tissues.² At higher temperatures, irreversible effects such as coagulation, carbonization or vaporization of tissues are produced.³⁻⁵ These effects are exploited for tissue ablation, a term used in medicine to refer to the destruction or removal of diseased (pathological) tissues.⁶ Thermal ablation, performed by either heating or cooling to reach temperatures lethal to cells, is used world-wide with the aim to treat cancer, cardiac arrhythmias and other conditions.⁷ Multiple energy sources such as laser, microwaves, ultrasound and radiofrequency (RF) current can be used for heating,⁸ while cryoablation is performed by circulating fluids through hollow needles (cryoprobes) to reach temperatures typically below -50°C.⁹

Efficient monitoring of ablation procedures is essential for improving the treatment outcome as well as to avoid unnecessary tissue damage.¹⁰ Generally, this is achieved by mapping the spatio-temporal distribution of temperature within the treated region either by inserting sensors at specific locations or with non-invasive imaging modalities such as infrared thermometry, x-ray computed tomography, magnetic resonance imaging or ultrasound.¹¹ Recently, several groups have suggested optoacoustic (OA, photoacoustic) imaging and sensing systems as a new approach for real-time monitoring of tissue ablation with high contrast and by using only non-ionizing excitation.^{12,13} OA presents unique advantages for this purpose as 1) the thermo-elastic conversion efficiency is highly sensitive to temperature variations (2.7% per °C)¹⁴⁻¹⁸ and 2) tissue coagulation leads to chemical changes further affecting the OA signal intensity.¹⁹ These two effects are clearly evinced in experiments performed for calibrating the temperature dependence of OA signals. It was shown that the increase in OA signal intensity per °C remains approximately constant for temperatures below 50°C, where it abruptly changes.²⁰ This additional increase in OA signal intensity, associated to coagulation of tissues at higher temperatures, was also shown to be maintained when the tissue was cooled down to room temperature. To this end, OA measurements

performed during thermal ablation procedures have corroborated this initial calibration experiments. Real-time temperature mapping was achieved for temperatures below coagulation thresholds¹⁴ and the ablated region could be identified after cooling down via multi-spectral analysis or comparison with the corresponding image before ablation.²¹ Real-time monitoring further enabled visualizing tissue destruction e.g. in endovenous laser ablation.²² However, assessing how the ablation lesion boundary progresses during an intervention remains challenging. It is known that the resulting lesion size depends both on temperature and exposure time,²³ and OA temperature readings are inaccurate when ablation is produced.²⁴ Tissue coagulation further leads to a change in optical attenuation,²⁵ which in turn produces distortion (spectral coloring) of the absorption spectrum at deep locations. Herein, we suggest a new approach for characterizing the evolution of the induced lesion based on identifying sharp changes in OA time profiles extracted from the sequence of images acquired with a four dimensional (real-time three dimensional) OA tomographic imaging system. The method is based on single-wavelength excitation and hence is not affected by spectral coloring or other OA signals changes in the optical wavelength dimension.

2. METHODS/RESULTS

A lay-out of the experimental set-up is depicted in Fig. 1a. Radiofrequency (RF) ablation was induced on a 30x30x10mm³ porcine heart tissue sample using a RF wave generator and an electrode with a 3 mm diameter semi-spherical shaped tip. A second (ground) electrode consisting of an aluminum foil was placed at the bottom surface of the tissue. The RF generator delivered bursts of 600 cycles at 20 kHz (Fig. 1b) with an average power of 9 W. Volumetric (three-dimensional - 3D) OA imaging was performed with a self-developed tomographic imaging system consisting of a 512-element spherically-arranged transducer array covering an angle of 140° (1.3 π solid angle) with 4 cm of curvature radius. Each array element has a central frequency of 5 MHz and 100% detection bandwidth, which enables a nearly isotropic resolution of 150 μ m around the geometrical center of the spherical array.¹¹ Efficient acoustic coupling and electrical insulation were facilitated by an agarose layer positioned between the active surface of the imaging array and the electrical ground pad. OA excitation was provided with a 10 Hz short-pulsed (≤ 10 ns) laser (Innolas Laser GmbH, Krailling, Germany) guided via a custom-made fiber bundle (CeramOptec GmbH, Bonn, Germany) through a central cavity in the array. The laser wavelength was set to 780 nm to provide maximum contrast between ablated and non-ablated tissues.²¹ The energy density per pulse and mean power density of the light beam at the tissue surface were maintained below safety standards.²⁶ A custom-made data acquisition system (DAQ, Falkenstein Mikrosysteme GmbH, Taufkirchen, Germany) was used for simultaneous acquisition of all 512 pressure signals at 40 megasamples per second. The acquired pressure signals were deconvolved with the frequency response of the array elements and band-pass filtered between 0.1 and 4 MHz. 3D OA images were subsequently reconstructed with a graphics processing unit (GPU)-based 3D back-projection algorithm.⁹

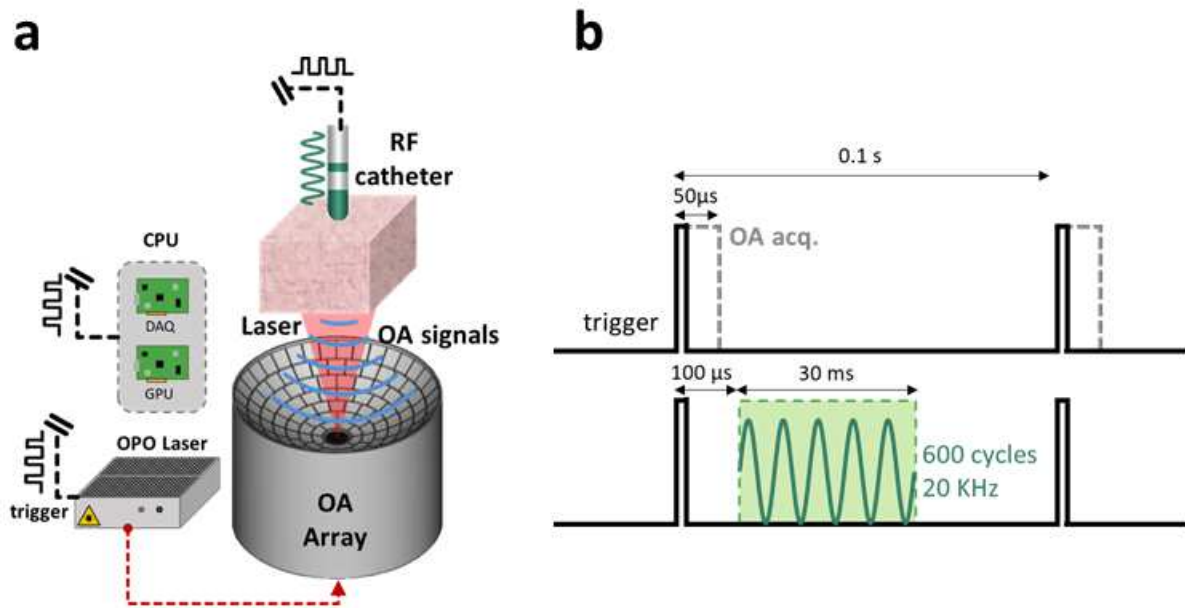


Figure 1. Schematic view of the experimental setup of the ablation experiment. (a) Drawings of the OA transducer array and RF system network. (b) Schematic synchronization diagram of the OA and RF excitations and acquisition routines.

For short-pulsed laser excitation under thermal and stress-confinement conditions,²⁷ the OA signal (initial pressure) is approximately given by $p_0 = \Gamma \mu_a \phi$, being Γ the (dimensionless) Grüneisen parameter, μ_a the optical absorption coefficient and ϕ the light fluence. The Grüneisen parameter is known to be temperature dependent and hence changes in OA signal amplitude can be used to estimate corresponding changes in temperature. Thus, for water and diluted aqueous solutions, the temperature rise at a given point can be estimated from the relative increase in OA signal intensity as²⁸

$$\Delta T = \frac{\Delta P_0(0.8113 + T_0)}{p_{0,0}} \quad (1)$$

being $p_{0,0}$ and T_0 the initial (baseline) OA signal and the initial temperature in 0,0, respectively. ΔT in Eq. 1 is expressed in °C.

RF ablation was performed in a porcine tissue sample with approximately 1 cm thickness.

The RF catheter containing the electrical excitation is in orthogonal position relative to the surface of the tissue sample. Thermal coagulation is initiated when the tissue resistance to the electrical input leads to a joule-effect temperature increase above the tissue-specific temperature and time of exposure time for tissue denaturation. The procedure is monitored in real-time by illuminating the region of interest treated beneath the electrode. The guiding fiber bundle delivers approximately 20 mJ of electromagnetic radiation and it gets diffused and scattered at the surface of the sample, subsequently leading to an exponential fluence decay in the direction of the beam path. Fig. 2a displays the time profiles of the relative increase in OA signal intensity during ablation for two points located at 6 mm (blue curve) and 10 mm (red curve) depth. Considering that soft biological tissues mainly consist of water, Eq. 1 can be taken as a reasonable approximation. Eq. 1 establishes that the increase in temperature is proportional to the relative increase in OA signal. Thereby, the estimated time profiles of temperature are equivalent to those shown in Fig. 2a for temperatures below the ablation temperature threshold (typically 50°C). However, this approximation is no longer valid when ablation takes place as additional changes in the Grüneisen parameter are produced. The time points when the ablation temperature threshold is reached (marked in Fig. 2b) can be identified in the differential profiles of temperature. Such time points can be used to

build a map corresponding to the onset time of ablation that serves to estimate how the lesion propagates with time.

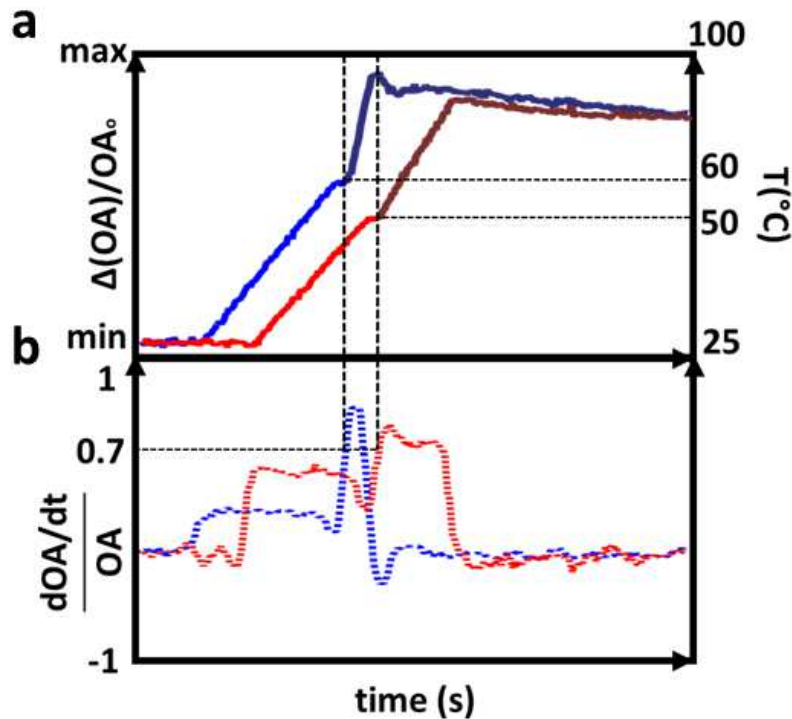


Figure 2. (a) Lay-out of the experimental setup. The RF catheter containing the electrical excitation is positioned orthogonally to the surface of the tissue sample. (b) Computational methods for estimation of the lesion size during RF ablation. OA signal derivative approach and coagulation temperature methods.

The time profile of OA signal intensity in Fig. 2b further features a significant slope change at approximately the time point when the ablation temperature threshold is reached. The below panel in Fig 2b displays the numerically estimated time derivative of the OA signal intensity ($\delta p_0/\delta t$). Four different intervals can be clearly distinguished. In the first (baseline) interval, $\delta p_0/\delta t = 0$. $\delta p_0/\delta t$ subsequently reaches defined positive values in a second and third intervals, while it eventually becomes slightly negative in the final interval. The significant change in $\delta p_0/\delta t$ between the second and third interval is consistent with the previously reported change in slope of the OA signal intensity versus pressure when ablation is produced,¹⁷ i.e., ablation begins between the second and third intervals in the $\delta p_0/\delta t$ curves. A map of the onset time of ablation can then be estimated from the time points between the second and third intervals by setting a threshold in $\delta p_0/\delta t$ for the voxels in the image. It is also important to note that the relative increase in OA signal for the first point features a relatively sharp decrease at the beginning of the fourth interval. This is arguably due to the fact that the light fluence is reduced when ablation at deeper regions (e.g. at point 2) starts to be produced. Indeed, the onset of ablation leads to an increased optical attenuation and a consequent decrease in light fluence and optoacoustic signal in the entire volume. Thereby, a sharp increase in optoacoustic signal is only produced for the time points when ablation starts, and the identification of these points represents a robust approach for assessing the progression of the lesion being formed.

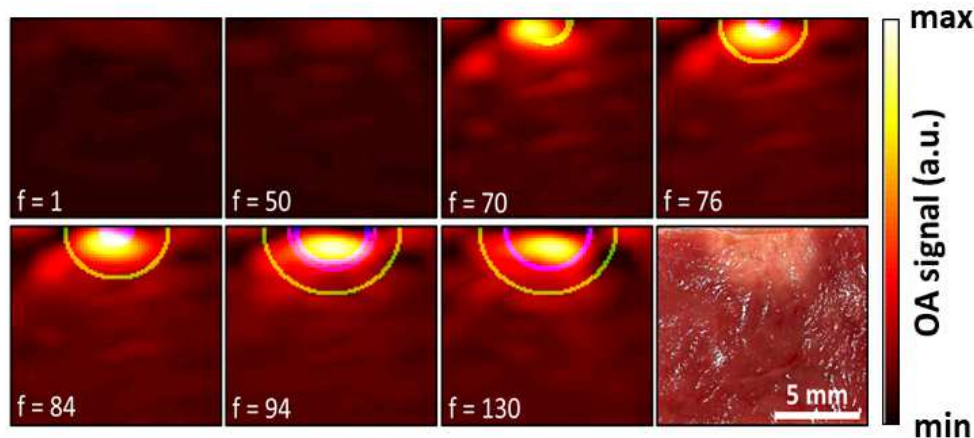


Figure 3. Lesion boundary progression results applying different detection methods. Coagulated region dimensions for width (w) and depth (d) of the ablated tissue displayed with continuous and dashed lines respectively. The coagulation boundary regions overlaid on top of the actual fluence-corrected OA images at different time-points during the treatment and the post-ablation cross-sectional view of the porcine tissue sample.

The lesion width and depth were examined for characterization of the lesion growth as a function of time. The ablated points were identified as those that 1) exceeded a give temperature threshold as estimated optoacoustically or 2) underwent a change in slope in the optoacoustic time profile. Fig. 3 shows the results of this characterization. Fig. 3a displays the measured width (w) and depth (d) of the lesion for two different values of the temperature threshold and for which the derivative of the optoacoustic normalized signal derivative increased by 70%, based on previous studies.¹⁷ It is shown that the lesion size estimated from the derivative of the optoacoustic signal approximately matches that estimated with a temperature threshold of 60°C. This is expected considering that for this temperature coagulation is almost instantaneous and the heating process is rather fast, i.e., a temperature of 60°C is reached before the time required for tissue ablation at lower temperatures, i.e.: 50°C. The dynamics of lesion formation is also visualized in a sequence of maximum intensity projections (MIPs) of the OA images along the lateral plane shown in Fig. 3b. For better visualization, the images were normalized with the light fluence distribution estimated from the diffusion equation for a semi-infinite medium, namely an exponential decay with depth from the illuminated surface with effective attenuation coefficient $\mu_{\text{eff}} = 3.5 \text{ cm}^{-1}$. A movie of the lesion formation process is provided as supplementary material in the online version of the journal. The dimensions of the lesion estimated with the time derivative of the OA signals ($w=6.1 \text{ mm}$ and $d=2.6 \text{ mm}$) approximately matched the observed lesions size in a photograph of a tissue section taken after the ablation procedure (Fig. 3b), which corroborates the validity of this approach.

3. DISCUSSION

The final size of the ablation lesion estimated both by considering the threshold temperature and the time derivative of the OA signals reasonable agreed with that observed visually in a section of the sample taken after the procedure. This, along with the fact that the results obtained with these two independent methods matched for different time points, appears to ratify the feasibility of OA monitoring of lesion progression in RF ablation procedures. Both methods are based on simple operations that can easily be computed in real-time, which ensures their applicability in the clinical setting.

In principle, the suggested methodology can as well be applied for monitoring the lesion progression in other ablation interventions based on alternative sources of energy. However, this needs to be verified for each specific case. Of particular importance is the induced spatio-temporal distribution of the temperature field. It is well-known that both the temperature and the exposure time have an influence on the resulting ablation lesion in the target tissue. Indeed, it has been noted that for each temperature exposure degree increase above 43°C, there is a two-fold drop in the time required to achieve the same biological denaturation effect.²³ Thereby, some methods to estimate tissue degradation account for both exposure time and temperature. For example, the cumulative

equivalent minutes (CEM) methodology establishes the time required to produce ablation in a tissue exposed to a given temperature.²⁹ These methods can potentially be implemented in the OA framework described in this work. However, accurate estimation e.g. of the CEM at a given point requires the development of more sophisticated models that properly account for the temperature dependence of the OA signals when ablation is produced. Cumulative exposure has a limited effect for the ablation method considered in this work since tissue ablation is produced in relatively short time, but it can be very important in slower procedures. It is also important to take into account that significant changes in the optical properties of tissues are produced when coagulation takes place. This in turn affects the light attenuation in tissues and leads to additional inaccuracies in the estimated temperature maps.

The newly suggested approach based on analyzing the changes in the temporal derivative of the OA signals does not rely on temperature estimations and hence it is expected to be more robust than alternative approaches. Indeed, the temperature ablation threshold can vary for different tissue types and hence the lesion size can be erroneously estimated even when considering an imaging approach that accurately maps the temperature distribution. Abrupt changes in the OA signal intensity can also enable identifying the onset of coagulation in ablation procedures based on a relatively large exposure time. Furthermore, the reported increase in optical attenuation in ablated tissues results in a reduced light fluence at deep locations.³⁰ Thereby, positive changes in the time derivative of OA signals are exclusively due to coagulation and can be detected at any point of the target tissue regardless of the light delivery method for OA excitation. The newly suggested method has been enabled by the unique OA capabilities for high-frame-rate imaging in three dimensions and for sensing chemical transformations taking place during coagulation. The fact that single wavelength excitation is sufficient for detecting such changes can also significantly reduce the cost of clinical embodiments. These features, along with the fact that non-ionizing radiation is employed, represent unparalleled advantages of OA with respect to other imaging modalities that can potentially be used for ablation monitoring. Multi-spectral OA imaging, based on tissue excitation at multiple optical wavelengths, can further provide additional information encoded both in the time and spectral dimensions.²¹ However, even though OA spectral changes have been detected in ablated tissues,⁷ these may not be properly identified in regions affected by the wavelength dependence of optical attenuation and single-wavelength excitation may still represent the optimum approach for ablation monitoring. Overall, we expect that the methodology introduced in this work helps improving the outcome of tissue ablation methods routinely used in the clinics.

ACKNOWLEDGMENTS

The authors acknowledge the support by the German Research Foundation (DFG) and the Technical University of Munich within the funding program Open Access Publishing.

REFERENCES

1. Verma, A. & Natale, A. *Circulation* **121**, p. 46–215, (2010).
2. Weininger, S., Pfefer, S. & Chang, I. A. *IEEE Symposium on Product Safety Engineering* **3-4(2)**, p. 83–91, (2005).
3. Larin, K. V., Larina, I. V., Motamedi, M. & Esenaliev, R. O. *SPIE Proc.* **3916**, p. 311–321, (2000).
4. Oyaga Landa, F. J. et. al. Noncontact monitoring of incision depth in laser surgery with air-coupled ultrasound transducers. *Optics letters.* **41**, p. 2704–2707, (2016).
5. Oyaga Landa, F. J. et. al. Noncontact monitoring of incision depth in laser surgery with air-coupled ultrasound transducers. *SPIE Digital Library.* **10064**, 100640H, (2017).
6. Teresawa, T., Balk, E. M. & Chung, M. *Comparative Effectiveness Review* **15**, (2009).
7. Pai, M. et. al. *World J Gastrointest Surg* **7**, p. 52–59, (2015).
8. Ahmed, M. et. al. *Radiology* **258(2)**, p. 351–369, (2011).
9. Kaltman, J. R. et. al. *J Cardiovascular Electrophysiology* **19(2)**, p. 343–347, (2008).
10. January, C. T. et. al. *Circulation* **130**, p. 2071–2104, (2014).
11. Xu, M. & Wang, L. et. al. *Physical Review E* **71**, p. 016706, (2005).

12. Rebling, J., Landa, F. J. O., Deán-Ben, X.L., Douplik, A. & Razansky, D. *Opt. Lett.* **130**, p. 2071–2104, (2014).
13. Rebling, J., Landa, F. J. O., Deán-Ben, X.L., Douplik, A. & Razansky, D. *SPIE Digital Library*. **10488**, p. 1048855, (2018).
14. Landa, F. J. O., Deán-Ben, X.L., Sroka, R. & Razansky, D. *Scientific Reports* **7**, p. 9695, (2017).
15. Oyaga Landa, F. J., Deán-Ben, X.L., Sroka, R. & Razansky, D. *SPIE Digital Library* **10494**, p. 104940D, (2018).
16. Oyaga Landa, F. J., Deán-Ben, X.L., Sroka, R. & Razansky, D. *SPIE Digital Library* **10415**, p. 104150A, (2017).
17. Oyaga Landa, F. J., Ronda Penacoba, S., Deán-Ben, X.L., Montero de Espinosa, F. & Razansky, D. *Ultrasonics* **5860**, (2018).
18. Oyaga Landa, F. J., Ronda Penacoba, S., Deán-Ben, X.L., Montero de Espinosa, F. & Razansky, D. *SPIE Digital Library* **10494**, 104945J, (2018).
19. Larina, I. V., Larin, K. V. & Esenaliev, R. O. *Journal of Physics D: Applied Physics* **38**(15), p. 2633–2639, (2005).
20. Datta, N. R. et. al. *Cancer Treatments Reviews* **41**, p. 742–753, (2015).
21. Pang, G.A., Bay, E., Deán-Ben, X.L. & Razansky, D. *Journal of cardiovascular electrophysiology*. **26**(3), p. 339–345, (2015).
22. Fehm, T.F. et. al. *J. Biophotonics*. **9**, p. 934–941, (2015).
23. Sapareto, S. A. & Dewey, W. C. *Int. J. Radiat. Oncol. Biol. Phys.* **10**, p. 787–800, (1984).
24. Larin, K. V., Larina, I. V., Motamedi, M. & Esenaliev, R. O. *SPIE Proc.* **3916**, p. 311–321, (2000).
25. Soroushian, B., Whelan, W. M. & Kolios, M. C. *SPIE Proc.* **75641N**, (2010).
26. ANSI: American National Standard for Safe Use of Lasers. *American National Standard Institute*, (2007).
27. Wang, L. V. & Wu, H. *Biomedical optics: principles and imaging*, (2010).
28. Cui, H. & Yang, X. *Medical Physics* **38**(10), p. 5345, (2011).
29. Chin, L.C.L., Whelan, W. M., Sherar, M.D. & Vitkin, I.A. *Physics in Medicine & Biology* **46**(9), p. 2407–2420, (2001).
30. Meng, L. et. al. *Photoacoustics* **13**, p. 33–45, (2019).

Chapter IV

Summary and Conclusion

Chapter 4

Summary and Conclusion

OA imaging is distinguished among other imaging modalities by its operational simplicity, its relatively low hardware costs and its competence to provide volumetric real-time imaging at high spatio-temporal resolutions. It is a hybrid imaging technique combining optics and US, thus capitalizing on the advantages of US detection and optical excitation. OA has been applied in many fields of fundamental research and it is now translated into clinical routine with increasing medical applications emerging. Future research development will be focused on the miniaturization of lasers and DAQ systems for an increased portability of OA imaging devices. Further technological implementations in OA imaging such as US transceivers that combine both functions as transmitter and receiver modes will lead to hardware reduction and powerful new appliances. The research studies carried out in this thesis hold a great potential for the advancement of OA sensing.

We have demonstrated the feasibility of tracking the incision profile during laser surgery by detection of shock waves emanating from the ablation spot with an air-coupled transducer, thus avoiding the need of a coupling medium. This new capability is expected to enable upcoming new applications in different types of clinically relevant interventions.

Also, we have introduced a new high-resolution volumetric temperature monitoring capability based on real-time acquisition of three-dimensional OA data. The demonstrated volumetric temperature mapping speed during photothermal ablation procedures, the hand-held characteristic and the OA intrinsic synergy combining optics and US will contribute to improving safety and efficacy of these treatments. Furthermore, the validated use of OA temperature mapping showcased that the proposed approach is capable of mapping the development of the temperature field during MIFU treatments. The proposed method further allows localizing the US focus, estimating the peak temperature and measuring the size of the heat-affected volume in real-time.

It was further shown how that the integration of the OA illumination source in copper-coated optical silica fibers that could deliver synchronously ablative RF energy, can be used to observe contrast-based dynamic changes in the OA images of forming RF lesions. The high spatiotemporal resolution and deep-tissue imaging capacity of the integrated ablation monitoring approach are an advantageous solution for optimizing the outcome of RF ablation interventions.

Finally, it was demonstrated how OA has unique capabilities for high-frame-rate volumetric imaging for sensing chemical transformations taking place during coagulation, based on changes in the temporal derivative of OA signals. Abrupt changes in the OA signal intensity can also enable identification of the onset of coagulation in ablation procedures.

In conclusion, OA signals are useful for providing incision depth feedback during laser surgeries where the presence of a tissue-transducer coupling medium is no longer needed. OA signal properties can be further utilized for real-time temperature monitoring during lesion progression and estimation of lesion size during thermal ablation treatments. The current research provides a substantial improvement to the advancement of OA imaging applications and it is anticipated that the methodology developed in this work will accelerate the transition of OA imaging into day to day routine, as well as improve the outcome of tissue ablation methods routinely used in the clinics.

Bibliography

- [1] Moros, E.G. “Physics of thermal therapy: fundamentals and clinical applications,” *CRC Press*, (2012).
- [2] Chu, K. F. & Dupuy, D. E. “Thermal ablation of tumours: biological mechanisms and advances in therapy,” *Nature Reviews Cancer*. **14**, 199–208 (2014).
- [3] Mensel, B., Weigel, C. & Hosten, N. “Laser-induced thermotherapy. Minimally invasive tumor therapies,” *Springer Berlin Heidelberg*. 69–75 (2006).
- [4] Torres-Reveron, J., Tomaszewicz, H. C., Shetty, A., Amankulor, N. M. & Chiang, V. L. “Stereotactic laser induced thermotherapy (LITT): a novel treatment for brain lesions regrowing after radiosurgery,” *Journal of neuro-oncology*. **113**, 495–503 (2013).
- [5] Ke, H. et al. “Gold nanoshelled liquid perfluorocarbon magnetic nanocapsules: a nanotheranostic platform for bimodal ultrasound/magnetic resonance imaging guided photothermal tumor ablation,” *Theranostics*. **14**, 12–23 (2014).
- [6] Zhang, F. et al. “Noninvasive dynamic imaging of tumor early response to nanoparticle-mediated photothermal therapy,” *Theranostics*. **5**, 1444–1455 (2015).
- [7] Schwarzmaier, H. & Eickmeyer, F. “Basic principles of laser induced interstitial thermotherapy in brain tumors,” *Medical Laser Application*. **17**(2), 147–158 (2002).
- [8] Vogel, A. & Venugopalan, V. “Mechanisms of pulsed laser ablation of biological tissues,” *Chemical reviews*. **103**(2), 577–644 (2003).
- [9] Ter Haar, G. & Coussios, C. “High intensity focused ultrasound: physical principles and devices,” *International Journal of Hyperthermia*. **23**(2), 89–104 (2007).

- [10] Ni, Y., Mulier, S., Miao, Y., Michel, L. & Marchal, G. "A review of the general aspects of radiofrequency ablation," *Abdominal imaging*. **30**(4), 381–400 (2005).
- [11] Simon, C., Dupuy, D. & Mayo-Smith, W. "Microwave ablation: principles and applications," *Radiographics*. **25**(1), 69–84 (2005).
- [12] Arsenault, M. G., Kolios, M. C. & Whelan, W. M. "Optoacoustic detection of thermal lesions," *SPIE Proc.* **7177**, 71771V (2009).
- [13] Cox, B. "Introduction to laser-tissue interactions." *PHAS*. **4886**, 1-61 (2007).
- [14] Cui, H. & Yang, X. "Real-time monitoring of high-intensity focused ultrasound ablations with photoacoustic technique: An in vitro study," *Medical Physics*. **38**(10), 5345 (2011).
- [15] Sapareto, S. A. & Dewey, W. C. "Thermal dose determination in cancer therapy," *Int. J. Radiat. Oncol. Biol. Phys.* **10**, 787-800 (1984).
- [16] Vogel, A. & Venugopalan, V. "Mechanisms of pulsed laser ablation of biological tissues," *Chemical reviews*. **103**(2), 577–644 (2003).
- [17] Dana, N., Di Biase, L., Natale, A., Emelianov, S. & Bouchard, R. "In vitro photoacoustic visualization of myocardial ablation lesions," *Heart Rhythm*. **11**, 150–157 (2014).
- [18] Fichera, L., Pacchierotti, C., Olivieri, E., Prattichizzo, D. & Mattos, L.S. "Kinesthetic and vibrotactile haptic feedback improves the performance of laser microsurgery," *IEEE Haptics Symposium*. **16**, 59–64 (2016).
- [19] Stübinger, S., Rechenberg, B., Zeilhofer, H., Sader, R. & Landes, C. "Er:YAG laser osteotomy for removal of impacted teeth: Clinical comparison of two techniques," *Lasers Surg. Med.* **39**, 583 (2007).
- [20] Neukam, F. W. & Stelzle, F. "Laser tumor treatment in oral and maxillofacial surgery," *Phys. Procedia*. **5**, 91 (2010).
- [21] Eyrich, G. K. H. "Laser-osteotomy induced changes in bone," *Med. Laser Appl.* **20**, 25 (2005).

- [22] White, J. M., Goodis, H. E. & Rose, C. L. "Use of the pulsed Nd:YAG laser for intraoral soft tissue surgery," *Lasers Surg. Med.* **11**, 455 (1991).
- [23] Tuchmann, A., Bauer, P., Plenk, H. & Braun, K. D. "Comparative study of conventional scalpel and CO₂-laser in experimental tumor surgery," *Res. Exp. Med.* **186**, 375 (1986).
- [24] Vogel, A. & Venugopalan, V. "Mechanisms of pulsed laser ablation of biological tissues," *Chem. Rev.* **103**, 577 (2003).
- [25] Stelzle, F. Zam, A., Adler, W., Tangermann-Gerk, K., Douplik, A., Nkenke, E. & Schmidt, M. "Optical nerve detection by diffuse reflectance spectroscopy for feedback controlled oral and maxillofacial laser surgery," *J. Transl. Med.* **9**, 20 (2011).
- [26] Jeong, D.C. Tsai, P.S & Kleinfeld, D. "Prospect for feedback guided surgery with ultra-short pulsed laser light," *Curr. Opin. Neurobiol.* **22**, 24 (2012).
- [27] Kim, B. M. Feit, M. D., Rubenchik, A. M., Mammini, B. M. & Da Silva, L. B. "Optical feedback signal for ultrashort laser pulse ablation of tissue," *Appl. Surf. Sci.* **857**, 127–129 (1998).
- [28] Nahen, K. & Vogel, A. "Investigations on acoustic on-line monitoring of IR laser ablation of burned skin," *Lasers Surg. Med.* **25**, 69 (1999).
- [29] Fichera, L., Pacchierotti, C., Olivieri, E., Prattichizzo, D. & Mattos, L. S. "Kinesthetic and vibrotactile haptic feedback improves the performance of laser microsurgery," *IEEE Haptics Symposium*. 59–64, (2016).
- [30] Bay, E., Deán-Ben, X. L., Pang, G. A., Douplik, A. & Razansky, D. "Real-time monitoring of incision profile during laser surgery using shock wave detection," *J. Biophoton.* **8**, 102 (2015).
- [31] Müller, G., Roggan, A., "Laser-Induced Interstitial Thermotherapy," *SPIE Optical Engineering Press.* **1**, 114–156 (1995).
- [32] Saccomandi, P. et al. "Laser interstitial thermotherapy for pancreatic tumor ablation: Theoretical model and experimental validation," *Proc IEEE Eng. Med. Biol. Soc.* 5585–8 (2011).

- [33] Landa, F. J. O., Deán-Ben, X. L., Sroka, R. & Razansky, D. "Volumetric Optoacoustic Temperature Mapping in Photothermal Therapy," *Sci. Rep.* **7**, 9695 (2017).
- [34] Hersh, D.S. et al. "Emerging Applications of Therapeutic Ultrasound in Neuro-oncology: Moving Beyond Tumor Ablation," *Neurosurgery*. **79**, 5 (2016).
- [35] Kim, Y.S., Rhim, H., Choi, M. J., Lim, H. K. & Choi, D. "High-intensity focused ultrasound therapy: an overview for radiologists," *Korean journal of radiology*. **9**, 291-302 (2008).
- [36] Chu, K. F. & Dupuy, D. E. "Thermal ablation of tumours: biological mechanisms and advances in therapy," *Nature Reviews Cancer*. **14**, 199-208 (2014).
- [37] Mast, T. D. et al. "Bulk ablation of soft tissue with intense ultrasound: Modeling and experiments," *The Journal of the Acoustical Society of America*. **118**, 2715-2724 (2005).
- [38] Slayton, M. H. & Barton, J. K. "Healing tissue response with ITU in musculoskeletal tissue, feasibility study," *IEEE Computer Society*. **4**, 1654-1657 (2014).
- [39] Claes, L. & Willie, B. "The enhancement of bone regeneration by ultrasound," *Progress in biophysics and molecular biology*. **93**, 384-398 (2007).
- [40] Dyson, M. "Enhancement of hyperthermia-induced apoptosis by non-thermal effects of ultrasound," *Cancer Letters*. **178**, 1 (2002).
- [41] Fuhrmann, T. A., Georg, O., Haller, J., Jenderka, K.-V. & Wilkens, V. "Uncertainty estimation for temperature measurement with diagnostic ultrasound," *Journal of therapeutic ultrasound* **4**, 28 (2016).
- [42] Saccomandi, P., Schena, E. & Silvestri, S. "Techniques for temperature monitoring during laser-induced thermotherapy: an overview," *International Journal of Hyperthermia*. **29**, 609-619 (2013).
- [43] Lahiri, B., Bagavathiappan, S., Jayakumar, T. & Philip, J. "Medical applications of infrared thermography: a review," *Infrared Phys Techn.* **55**, 221-235 (2012).

- [44] Lewis, M. A., Staruch, R. M. & Chopra, R. "Thermometry and ablation monitoring with ultrasound," *International Journal of Hyperthermia*. **31**, 163-181 (2015).
- [45] Fani, F., Schena, E., Saccomandi, P. & Silvestri, S. "CT-based thermometry: an overview," *International Journal of Hyperthermia*. **30**, 219-227 (2014).
- [46] Rieke, V. & Butts Pauly, K. "MR thermometry," *Journal of magnetic resonance imaging*. **27**, 376-390 (2008).
- [47] January, C. T. et. al. "2014 AHA/ACC/HRS guideline for the management of patients with atrial fibrillation: executive summary: a report of the American College of Cardiology/American Heart Association Task Force on practice guidelines and the Heart Rhythm Society," *Circulation*. **130**, 2071-104 (2008).
- [48] Haïssaguerre, M., Jaïs, P., Shah, D. C. et. al. "Spontaneous initiation of atrial fibrillation by ectopic beats originating in the pulmonary veins," *N Engl J Med*. **339**, 659-66 (2000).
- [49] Harvey, M., Kim, Y., Souse, J., El-Atassi, R., Morady, F., Calkins, H. & Langberg, J. "Impedance monitoring during radiofrequency catheter ablation in humans," *Pacing Clin. Electrophysiol*. **15**, 22 (1992).
- [50] Calkins, H., Prystowsky, E., Carlson, M., Klein, L. S., Saul, J. P. & Gillette, P. "Temperature monitoring during radiofrequency catheter ablation procedures using closed loop control. Atakr multicenter investigators group," *Circulation*. **90**, 1279 (1994).
- [51] Liu, Z., Ahmed, M., Weinstein, Y., Yi, M., Mahajan, R. L. & Goldberg, S. N. "Characterization of the RF ablation-induced oven effect: the importance of background tissue thermal conductivity on tissue heating," *Int. J. Hyperthermia*. **22**, 327-329 (2006).
- [52] Vergara, G. R. et. al. "Real-time magnetic resonance imaging-guided radiofrequency atrial ablation and visualization of lesion formation at 3 Tesla," *Heart Rhythm*. **8**, 295-303 (2011).

- [53] Wright, M. et. al. "Real-time lesion assessment using a novel combined ultrasound and radiofrequency ablation catheter," *Heart Rhythm*. **8**,304-312 (2011).
- [54] Li, C. H. & Wang, L. H. V. "Photoacoustic tomography and sensing in biomedicine," *Physics in Medicine and Biology*. **54**(19), R59-R97 (2009).
- [55] Soubret, A. & Ntziachristos, V. "Textbook of in vivo Imaging in Vertebrates," *John Wiley & Sons*. (2007).
- [56] Wang, L. V. & Wu, H. I. "Biomedical Optics: Principles and Imaging," *Wiley-Interscience*. (2007).
- [57] Taruttis, A. "Multispectral optoacoustic tomography for imaging of disease biomarkers," PhD thesis, *Technical University of Munich TUM* (2012).
- [58] Angelsen, B. A. J. & Waag, R. C. "Ultrasound Imaging: waves, signals and signal processing," *The Journal of the Acoustical Society of America*. **121**(4), 697 (2007).
- [59] Esenaliev, R. O., Karabutov, A. A. & Oraevsky, A. A. "Sensitivity of laser optoacoustic imaging in detection of small deeply embedded tumors" *IEEE Journal of selected topics in Quantum electronics*. **5**(4), 981-988 (1999).
- [60] Esenaliev, R. O. et. al. "Laser optoacoustic imaging for breast cancer diagnostics: Limit of detection and comparison with X-ray and ultrasound imaging," *SPIE Proc.* **2979**, 0277-786 (2009).
- [61] Razansky, D. "Multi-spectral Optoacoustic Tomography – Volumetric Color Hearing in Real Time," *IEEE Journal of Selected Topics in Quantum Electronics*. **18**(3), 1235-1243 (2012).
- [62] Gusev, V. E., *Laser Optoacoustics*, *Amer Inst of Physics* (1993).
- [63] Kozhushko, V. et. al. "Focused array transducer for two-dimensional optoacoustic tomography," *Journa of the Acoustical Society of America*. **116**(3), 1498-1506 (2004).
- [64] Shung, K. K. & Zipparo, M. "Ultrasonic transducers and arrays," *IEEE Engineering in Medicine and Biology Magazine*. **15**(6), 20-30 (1996).

- [65] Xu, M. H. & Wang, L. H. V. "Photoacoustic imaging in biomedicine," *Review of Scientific Instruments*. **77**(4), 041101 (2006).
- [66] Xu, M. H. & Wang, L. H. V. "Universal back-projection algorithm for photoacoustic computed tomography," *Physical Review E*. **71**(1), 016706 (2005).
- [67] Rosenthal, A., Ntziachristos, V. & Razansky, D. "Acoustic inversion in optoacoustic tomography: A review," *Current Medical Imaging Reviews*. **9**(4), 318-336 (2013).
- [68] Burgholzer, P., Matt, G. J., Haltmeier, M. & Paltauf, G. "Exact and approximate imaging methods for photoacoustic tomography using an arbitrary detection surface," *Physical Review E*. **75**, 046706 (2007).
- [69] Ntziachristos, V. & Razansky, D. "Molecular imaging by means of multispectral optoacoustic tomography (MSOT)," *Chemical Reviews*. **110**(5), 2783-2794 (2010).
- [70] Razansky, D., Distel, M., Vinegoni, C. & Ma, R. "Multispectral opto-acoustic tomography of Deep-seated fluorescent proteins in vivo," *Nature Photonics*. **3**, 412-417 (2009).
- [71] Razansky, D., Vinegoni, C. & Ntziachristos, V. "Multispectral photoacoustic imaging of fluorochromes in small animals," *Optics Letters*. **32**(19), 2891-2893 (2007).
- [72] Tzoumas, S., Deliolanis, N., Morscher, S. & Ntziachristos, V. "Unmixing molecular agents from absorbing tissue in multispectral optoacoustic tomography," *Medical Imaging IEEE Transactions*. **33**(1), 48-60 (2013).
- [73] Pallav, K., Saxena, I. & Ehmman, K. F. "Laser-induced plasma micromachining process: principles and performance," *Journal of Micro and Nano-manufacturing*. **3**(3), 031004 (2015).
- [74] Steen, W. & Majumdar, J. *Laser Material Processing*. Springer. **2**, (2005).
- [75] Noack, J. & Vogel, A. "Laser-induced plasma formation in water at nanosecond to femtosecond time scales: Calculation of thresholds, absorption coefficients, and energy density," *IEEE J. Quantum Electron*. **35**(8), 1156-1167 (1999).

- [76] Vogel, A. et. al. "Intraocular Nd:YAG laser surgery: Laser-tissue interaction, damage range, and reduction of collateral effects," *IEEE J. Quantum Electron.* **26**(12), 2240-2260 (1990).
- [77] Walsh, J. T. J. & Deutsch, T. F. "Measurement of Er:YAG laser ablation plume dynamics," *Appl. Phys. B* **52**, 217 (1991).
- [78] Kaufmann, R. & Hibst, R. "Pulsed erbium:YAG laser ablation in cutaneous surgery" *Lasers in Surgery and Medicine.* **19**(3), 324-330 (1996).
- [79] Landa, F. J. O., Deán-Ben, X. L., Montero de Espinosa, F. & Razansky, D. "Non-contact monitoring of incision depth in laser surgery with air-coupled ultrasound transducers," *Optics Letters.* **41**(12), 2704 (2016).
- [80] Vergara, G. R. et. al. "Real-time magnetic resonance imaging-guided radiofrequency atrial ablation and visualization of lesion formation at 3 Tesla," *Heart rhythm: The official journal of the Heart Rhythm Society.* **8**, 295–303 (2011).
- [81] Wright, M., Harks, E., Deladi, S. & Suijver, F. "Real-time lesion assessment using a novel combined ultrasound and radiofrequency ablation catheter," *Heart Rhythm.* **8**(2), 304-312 (2011).
- [82] Fahey, B. J. et. al. "Acoustic radiation force impulse imaging of myocardial radiofrequency ablation: initial in vivo results," *IEEE Trans Ultrason Ferroelectr Freq Control.* **52**(4), 631-641 (2005).
- [83] Eyerly, S. A. et. al. "Intracardiac acoustic radiation force impulse imaging: A novel imaging method for intraprocedural evaluation of radiofrequency ablation lesions," *Heart Rhythm.* **9**(11), 1855-1862 (2012).
- [84] Seo, C. H. et. al. "The feasibility of using thermal strain imaging to regulate energy delivery during intracardiac radio-frequency ablation," *IEEE Transactions on Ultrasonics, Ferroelectrics, and Frequency Control.* **58**(7), 1406-1417 (2011).
- [85] Stephens, D. "First in vivo use of a capacitive micromachined ultrasound transducer array-based imaging and ablation catheter," *Journal of Ultrasound in Medicine.* **31**(2), 247-256 (2012).

- [86] Fleming, C. P., Quan, K. J., Wang, H., Amit, G. & Rollins, A. M. "In vitro characterization of cardiac radiofrequency ablation lesions using optical coherence tomography," *Optics Express*. **18**, 3079-92 (2010).
- [87] Fleming, C. P., Rosenthal, N. & Rollins, A. M. "First in vivo real-time imaging of endocardial radiofrequency ablation by optical coherence tomography: Implications on safety and the birth of electro-structural substrate-guided ablation," *The Journal of Innovations in Cardiac Rhythm Management*. **2**, 199-201 (2011).
- [88] Pang, G. A., Bay, E., Deán-Ben, X. L. & Razansky, D. "Three-dimensional optoacoustic monitoring of lesion formation in real time during radiofrequency catheter ablation," *Journal of Cardiovascular Electrophysiology*. **26**(3), 339-345 (2014).
- [89] Dana, N., Di Biase, L., Natale, A., Emelianov, S. & Bouchard, R. "In vitro photoacoustic visualization of myocardial ablation lesions," *Heart Rhythm*. **11**, 150-157 (2014).
- [90] Prahl, S. "Molar extinction coefficients of haemoglobin and oxy-hemoglobin," OR: *Oregon Health and Science University School of Medicine*. (1999).
- [91] Fehm, T. F., Deán-Ben, X. L., Schaur, P., Sroka, R. & Razansky, D. "Volumetric optoacoustic imaging feedback during endovenous laser therapy – an ex vivo investigation," *Journal of Biophotonics*. **9**(9), 934-941 (2015).
- [92] Cain, C.P. & Welch, A.J. "Thin-film temperature sensors for biological measurements," *IEEE Trans Biomed Eng.* **21**, 421-423 (1974).
- [93] Welch, A. J. "Measurement and prediction of thermal injury in the retina of the rhesus monkey," *IEEE Trans Biomed Eng.* **31**, 633-644 (1984).
- [94] Muschter, R. & Whitfield, H. "Interstitial laser therapy of benign prostatic hyperplasia" *Eur. Urol.* **35**, 147-154 (1999).
- [95] Rao, Y.J. "In-fiber Bragg grating sensors," *Meas. Sci. Technol.* **8**, 355-375 (1997).
- [96] Silvestri, S. & Schena, E. "Optical-fiber measurement systems for medical applications," *Optoelectronics: Devices and Applications. Predeep P*, 205-224 (2011).

- [97] Wickersheim, K.A. & Sun, M.H. "Fiberoptic thermometry and its applications," *J. Microwave Power*. **22**, 85-94 (1987).
- [98] Grattan, K.T.V. & Zhang, Z.Y. "Fiber Optic Fluorescence Thermometry: Introduction," *New York, NY: Springer*. 1-34 (1995).
- [99] Allison, S.W., Gillies, G.T., Rondinone, A.J. & Cates, M.R. "Nanoscale thermometry via the fluorescence of YAG:Ce phosphor particles: measurements from 7 to 77°C," *Nanotechnology*. **14**, 859-863 (2003).
- [100] Simons, A.J., McClean, I. P. & Stevens, R. "Phosphors for remote thermograph sensing in lower temperature ranges," *Electronics Letters*. **32**(3), 253-4 (1996).
- [101] Cetas, T.C. "Will thermometric tomography become practical for hyperthermia treatment monitoring," *Cancer Res*. **44**, S4805-8 (1984).
- [102] Homolka, P., Gahleitner, A. & Nowotny, R. "Temperature dependence of HU values for various water equivalent phantom materials," *Phys Med Biol*. **47**, 2917-23 (2002).
- [103] Pandeya, G.D. et. al. "Assessment of thermal sensitivity of CT during heating of liver: An ex vivo study," *Brit. J. Radiol*. **85**, e661-5 (2012).
- [104] Pandeya, G.D. et. al. "Feasibility of noninvasive temperature assessment during radiofrequency liver ablation on computed tomography," *J. Comput. Assist. Tomogr*. **35**, 356-360 (2011).
- [105] Schena, E. et. al. "Experimental assessment of CT-based thermometry during laser ablation of porcine pancreas," *Phys. Med. Biol*. **58**, 5705-16 (2013).
- [106] Hoskins, P., Martin, K. & Thrush, A. "Diagnostic Ultrasound: Physics and Equipment, 2nd ed.," *Cambridge University Press*. (2010).
- [107] Pearce, J. Valvano, J.W. & Emelianov, S. "Optical Thermal Response of Laser Irradiated Tissue: Temperature measurement," *New York, NY: Springer*. 434-444 (2011).

- [108] Parker, D.L. "Applications of NMR imaging in hyperthermia: An evaluation of the potential for localized tissue heating and noninvasive temperature monitoring," *IEEE Trans Biomed Eng.* **31**, 161-167 (1984).
- [109] Graham, S.J., Bronskill, M.J. & Henkelman, R.M. "Time and temperature dependence of MR parameters during thermal coagulation of ex vivo rabbit muscle," *Magn. Reson. Med.* **39**, 198-203 (1998).
- [110] Parker, D.L. et al. "Temperature distribution measurements in two-dimensional NMR imaging," *Med. Phys.* **10**, 321-325 (1983).
- [111] Rieke, V. & Pauly, K.B. "MR thermometry" *J. Magn. Reson. Imaging.* **27**, 376-90 (2008).
- [112] Wlodarczyk, W. et al. "Comparison of four magnetic resonance methods for mapping small temperature changes," *Phys. Med. Biol.* **44**, 607-24 (1999).
- [113] Kickhefel, A. et al. "A pilot study for clinical feasibility of the near-harmonic 2D referenceless PRFS thermometry in liver under free breathing using MR-guided LITT ablation data," *Int. J. Hyperthermia.* **28**, 250-66 (2012).
- [114] Feng, Y. & Fuentes, D. "Model-based planning and real-time predictive control for laser induced thermal therapy," *Int. J. Hyperthermia.* **27**, 751-61 (2011).
- [115] Christensen, D.A. "A new nonperturbing temperature probe using semiconductor band edge shift," *J. Bioeng.* **1**, 541-5 (1977).
- [116] Cetas, T.C., Connor, W.G. & Manning, M.R. "Monitoring of tissue temperature during hyperthermia therapy," *Ann. NY Acad. Sci.* **335**, 281-297 (1980).
- [117] Liu, L. et al. "Wideband fluorescence-based thermometry by neural network recognition: Photothermal application with 10ns time resolution," *Journal of Applied Physics.* **118**(18), (2015).
- [118] Rieke, V. & Pauly, K. B. "MR thermometry," *Journal of Magnetic Resonance Imaging.* **27**(2), 376-390 (2008).

- [119] Larina, I. V., Larin, K. V. & Esenaliev, R. O. "Real-time optoacoustic monitoring of temperature in tissues," *Journal of Physics D: Applied Physics*. **38**(15), 2633–2639 (2005).
- [120] Wang, W. & Mandelis, A. "Thermally enhanced signal strength and SNR improvement of photoacoustic radar module," *Biomedical Optics Express*. **5**, 2785–2790 (2014).
- [121] Oraevsky, A. A., Esenaliev, R. O., Motamedi, M., Karabutov, A. A. "Real time optoacoustic monitoring of changes in tissue properties," *US Patent 6,309,352*.
- [122] Niemz, M. H. "Laser-tissue interactions: fundamentals and applications," *Springer Science & Business Media*. (2013).
- [123] Jang, H.J., Lee, J-Y., Lee, D-H., Kim, W-H. & Hwang, J.H. "Current and future clinical applications of HIFU for pancreatic cancer," *Gut Liver*. **4**, S57–61 (2010).
- [124] Larin, K.V., Larina, I.V., Motamedi, M. & Esenaliev, R.O. "Monitoring of temperature distribution with optoacoustic technique in real time," *SPIE Proc.* **3916**, 311–321 (2000).
- [125] January, C. T. et. al. "2014 AHA/ACC/HRS guideline for the management of patients with atrial fibrillation" *Circulation*. **130**, 2071–2104, (2014).
- [126] Rebling, J., Landa, F. J. O., Deán-Ben, X. L., Douplik, A. & Razansky, D. "Integrated catheter for simultaneous radio frequency ablation and optoacoustic monitoring of lesion progression," *Optics Letters*. **43**(7), 1–4 (2018).
- [127] Oyaga Landa, F. J., Ronda Penacoba, S., Deán-Ben, X.L., Montero de Espinosa, F. & Razansky, D. "Four-dimensional optoacoustic monitoring of tissue heating with médium intensity focused ultrasound," *Ultrasonics*. **5860**, (2018).
- [128] Kaltman, J. R. et. al. "Time and temperature profile of catheter cryoablation of right septal and free wall accessory pathways in children," *J. Cardiovascular Electrophysiology*. **19**(2), 343–347, (2008).

- [129] Datta, N. R. et. al. "Local hyperthermia combined with radiotherapy and-/or chemotherapy: recent advances and promises for the future," *Cancer Treatments Reviews*. **41**, 742–753, (2015).
- [130] Soroushian, B., Whelan, W. M. & Kolios, M. C. "Dynamics of thermoelastic expansion for native and coagulated ex-vivo bovine liver tissues," *SPIE Proc.* **75641N**, (2010).
- [131] Garcia-Hernandez, M.J. et. al. "Ultrasonic lamb wave NDE system using an air coupled concave array transducer," *IEEE Int. Ultrason. Symp.* **2**, 1282–1285, (2004).
- [132] Orsi, F. et. al. "High-intensity focused ultrasound ablation: effective and safe therapy for solid tumors in difficult locations," *AJR Am. J. Roentgenol.* **195**(3), 245–52, (2010).
- [133] Deán-Ben, X.L., Gottschalk, S., Mc Larney, B., Shoham, S. & Razansky, D. "Advanced optoacoustic methods for multiscale imaging of in vivo dynamics," *Chem. Soc. Rev.* **46**(8), 2158–2198, (2017).
- [134] Chin, C.L., Whelan, W.M., Sherar, M.D. & Vitkin, I.A. "Changes in relative light fluence measured during laser heating: implications for optical monitoring and modelling of interstitial laser photocoagulation," *Physics in Medicine & Biology* **46**(9), 2407–2420, (2001).